UCLA
UCLA Electronic Theses and Dissertations

Title
Theory of Particle Focusing in Inertial Microfluidic Devices

Permalink
https://escholarship.org/uc/item/09w02703

Author
Hood, Kaitlyn Tuley

Publication Date
2016

Peer reviewed|Thesis/dissertation

Theory of Particle Focusing in Inertial Microfluidic Devices

A dissertation submitted in partial satisfaction
of the requirements for the degree
Doctor of Philosophy in Mathematics

by

Kaitlyn Tuley Hood

2016

ABSTRACT OF THE DISSERTATION

Theory of Particle Focusing
in Inertial Microfluidic Devices

by

Kaitlyn Tuley Hood

Doctor of Philosophy in Mathematics

University of California, Los Angeles, 2016

Professor Marcus Leigh Roper, Chair

Microfluidic devices are tiny circuits that flow fluids instead of electrons. Because they are inexpensive and portable, microfluidic devices are ideal for use in areas where medical resources are scarce. Inertial microfluidic devices represent a new direction in microfluidic device design in which high flow speeds are used to exert nonlinear inertial effects on the fluid and on fluid-suspended particles. While inertial microfluidic devices are finding applications in fields such as fluid mixing, particle filtration, flow cytometry (the counting, sorting, and analyzing of cells), the devices are built with essentially no theoretical input due to a lack of models for the nonlinear inertial effects.

Why is there so little theory for inertial microfluidic devices? While there are many numerical methods for simulating inertial migration, because most devices have multiple moving boundaries and rely on three-dimensional effects, simulations are computationally intensive. In many cases, the computational time far exceeds the time needed to build and test a device experimentally. In contrast, asymptotic studies of inertial migration are only valid in limited cases, such as vanishingly small particle sizes.

This thesis is concerned with developing a theory for inertial effects in microfluidic devices for a wide range of complicated geometries. This theory is achieved through the combination of both asymptotic and numerical methods. First, a theory is developed for the inertial lift

force on a particle in a square channel. Second, this theory for the inertial lift force is validated against experiment. Third, a theory is developed for the formation of particle chains in a rectangular channel. Finally, a theory is developed for the number of focusing positions in a given channel.

The dissertation of Kaitlyn Tuley Hood is approved.

Dino Di Carlo

Russell E. Caflisch

Christopher R. Anderson

Marcus Leigh Roper, Committee Chair

University of California, Los Angeles

2016

To my grandparents.

TABLE OF CONTENTS

xiii

LIST OF TABLES

Vita

2010	B.S. (Mathematics and Physics), University of Maryland, College Park.
2010	National Science Foundation Graduate Research Fellowship.
2012	M.A. (Mathematics), UCLA, Los Angeles, California.

Publications

K. Hood, S. Kahkeshani, D. Di Carlo, and M. Roper. Direct measurement of particle inertial migration in rectangular channels. *Lab on a Chip*, 16(15):2840-2850, 2016.

K. Hood, S. Lee, and M. Roper. Inertial migration of a rigid sphere in three-dimensional poiseuille flow. *Journal of Fluid Mechanics*, 765:452479, 2015.

L. dePillis, E. J. Graham, K. Hood, Y. Ma, A. Radunskaya, and J. Simons. Injury- initiated clot formation under flow: A mathematical model with warfarin treatment. In *Applications of Dynamical Systems in Biology and Medicine*, volume 158 of *The IMA Volumes in Mathematics and its Applications*, pages 7598. Springer New York, 2015.

K. A. Okoudjou, R. S. Strichartz, and E. K. Tuley. Orthogonal polynomials on the sierpinski gasket. *Constructive Approximation*, 37(3):311340, 2013.

G. Kutyniok, K. A. Okoudjou, F. Philipp, and E. K. Tuley. Scalable frames. *Linear Algebra and its Applications*, 438(5):22252238, 2013.

CHAPTER 1

Introduction

Microfluidics – the manipulation of fluids in channels with dimensions in the tens of micrometers – is an emergent field of study. Microfluidics has the potential to influence subject areas from chemical synthesis and biological analysis to optics and information technology [77]. Microfluidic devices are inexpensive and portable and therefore ideal for use in in areas where medical resources are scarce. Because microfluidic devices are so small, typical Reynolds numbers describing the flow are $Re \ll 1$ and fall in the Stokes regime - where the dynamics are governed by the Stokes equations.

In contrast, there is a subset of microfluidic devices with fast enough flow that the Reynolds number is large ($1 \leq Re \leq 500$) – called inertial microfluidic devices. In such devices the fluid inertia is nonzero and can exert a force on bodies (i.e. particles or cells) submerged in the flow. This force is called the inertial lift force. The inertial lift force pushes particles to migrate across streamlines to settle to a deterministic set of streamlines [22]. This movement across streamlines is called inertial focusing, and can be exploited to manipulate and filter particles. Examples include fluid mixing, particle filtration, flow cytometry (the counting, sorting, and analyzing of cells) [22]. While inertial particle focusing is increasingly exploited in applications, there is still a darth of predictive theory.

Why is there so little theory for inertial microfluidic devices? While many numerical simulations exist [23, 12, 57, 54, 29], the computational time far exceeds the time needed to build and test a device experimentally. Furthermore, many costly simulations are needed to determine which physical effects are universal dynamical features or transient features that depend strongly on initial conditions. Conversely, while there have been many asymptotic

studies of particle dynamics [62, 32, 63, 2], these models were unable to predict the behavior observed in experiments.

While inertial focusing is interesting and useful in its own right, it exemplifies a class of problems that are mathematically significant: partial differential equations with moderate nonlinearity and complicated domains. These problems are difficult to model by existing methods because they have moderately large nonlinear effects, and therefore the solution must use some numerical component. However, these problems also have multiple moving boundaries and complicated three-dimensional domains, making purely numerical methods difficult and costly. As a result, we solve this class of problems through the combination of singular asymptotics and cutting-edge numerical techniques.

Restricting this class of problems to applications in hydrodynamics, we arrive at a juxtaposition between two partial differential equations (PDEs): the Navier-Stokes equations (NSE) and the Stokes equations (SE):

$$
\text{(NSE)} \begin{cases} \nabla^2 \mathbf{u} - \nabla p \ = Re\left(\partial_t \mathbf{u} + \mathbf{u} \cdot \nabla \mathbf{u}\right) \\ \nabla \cdot \mathbf{u} \ = 0, \end{cases} \qquad \text{(SE)} \begin{cases} \nabla^2 \mathbf{u} - \nabla p = 0 \\ \nabla \cdot \mathbf{u} = 0. \end{cases}
$$

Here, the Reynolds number $Re = \rho U \ell / \mu$, a dimensionless number representing the strength of the nonlinear inertial term in the NSE. In the limit that Re approaches zero, the nonlinear NSE reduce to the linear SE. We are interested in modeling the NSE with moderate Reynolds number, $1 < Re < 500$, via asymptotic methods that exploit the solutions of the SE.

The linearity and time-instaneity of the SE makes them tractable for many numerical methods as well as for asymptotic techniques. In particular, solutions can be constructed from super-positions of Green's functions (known in fluid mechanics as Stokeslets), or by regularized Green's functions [15, 16], representing boundaries of moving bodies by low-dimensional elements.

In contrast, because of their nonlinearity and differential-algebraic structure, the NSE have no fundamental solutions, and are solved only by numerical methods. Although these

methods are extensive they produce computationally massive solutions, making them too slow for experimental design and optimization. Existing perturbation theory, although dating back to Oseen, revealed fundamental features of singular asymptotics [58]. However, these theories have been developed only for high symmetry bodies (spheres, ellipsoids, etc.) in unbounded flow, and there is no clear path for adapting these theories to practical engineering geometries and flows.

In this dissertation, we attempt to carve a path for solving the class of nonlinear PDEs with complicated domains by considering the example of inertial microfluidic devices. (Here, low Reynolds number microfluidic devices satisfy the SE, while inertial microfluidic devices satisfy the NSE.) Microfluidics is an ideal application to study because experiments are cheap and quick to build, facilitating the validation of mathematical models. (mention singularities here)

This dissertation is ogranized into four parts.

Chapter 2: We derive a model for the inertial lift force on a single particle in a square channel. While this has been extensively studied both asymptotically and numerically since the 60s, never the less recent experiments [23] uncovered a contradiction with existing theory. We reconcile the experimental findings with theory by extending the asymptotic model in two ways: (i) solving the model in 3 dimensions (instead of two dimensions) and (ii) calculating the next term in the perturbation series. The result predicts the inertial focusing of particles for a wider range of Reynolds numbers and particle sizes than was previously accessed by theoretical studies.

Chapter 3: We develop an experimental method to validate the prediction of the inertial focusing developed in Chapter 2. While inertial focusing was first observed in the 60s by [64], and more recently has been exploited in biomedical devices (cite Di Carlo), inertial focusing has only been observed in streak images – averaging over time and many particles. Here we use high speed imaging and an image processing reconstruction algorithm to observe

the migration velocities of individual particles. This direct observation of inertial migration velocities agrees well with the prediction by the model developed in Chapter 2.

Chapter 4: Once particles have been focues to their inertial streamline, they can interact streamwise with each other to form a regularly spaced lattice – a phenomenon called particle chaining. Particle chains can be exploited in inertial microfluidic devices for flow cytometry, high speed imaging, and entrapment. While the location and number of chains can be manipulated by changing the channel geometry, the particle interactions are not understood well enough to manipulate the spacing between particles. We develop a mathematical model of particle interactions and the formation of particle chains.

Chapter 5: Can we engineer a channel to have any given number of inertial focusing positions? Thus far we have only considered rectangular channels, which because of the symmetry, particles must focus to either two or four inertial focusing positions. But with soft-lithography methods, inertial microfluidic devices can have channels with a wide range of cross-sections. In this final chapter we publish some works in progress. First we derive a theory for the number of focusing positions in a rectangular channel. Then we develop a heuristic explanation of the inertial lift force in order to develop a theory for engineering devices.

CHAPTER 2

Inertial migration of a rigid sphere in three-dimensional Poiseuille flow

2.1 Background

Inertial microfluidic devices employ inertial focusing to segregate and sort chains of particles, and to move particles between streams of different fluids. For example, centrifuges-on-a-chip [50, 69] trap circulating cancer cells from blood in microchannel vortices, and sheathless high-throughput flow cytometry [38, 13] fractionates particles from a buffer in order to image and count rare blood cells. However there are no predictive theories that describe the trajectories of particles during inertial focusing. Instead the features of these devices, including flow-rate and geometry, are optimized by experimental trial-and-error. Although asymptotic theories exist for inertial lift forces, they are quantitatively correct only for asymptotically small particles, much smaller than the particles that are typically used in microfluidic devices. Previous asymptotic theories also do not predict how differently sized particles will be differently focused [23].

Inertial migration of particles was first observed in 1961 by Segré and Silberberg. Experiments showed that a dilute suspension of neutrally buoyant particles flowing in a cylindrical pipe at moderate speeds will migrate across streamlines [64, 65, 66]. Particles initially uniformly dispersed through the cross-section of the pipe became focused into a ring with radius 0.6 times the channel radius. Since the reversibility of Stokes equations (the limit of the Navier-Stokes equations when Reynolds number, $Re = 0$) prohibits movement across

streamlines this migration must arise from inertia in the flow [7].

Many theoretical studies of this effect using asymptotic theory are described below. Each study focuses on a particular limit of two dimensionless groups, Re and α. The first parameter, Re, is the channel Reynolds number, and only depends on the dimensions of the pipe and the properties of unladen flow into the channel. The second parameter, α, is a ratio of the particle size to a characteristic channel length scale. Some studies take this length scale to be the width of the channel, others the distance between the particle and the wall. Values for these parameters in various studies are compiled in table 2.1.

Although early theoretical studies [61, 62] illuminated how inertial lift forces are generated by applied torques or body forces, [18] were the first to directly address lift forces on neutrally buoyant particles. They consider a body of arbitrary shape suspended in a fluid bounded by a system of walls in three dimensions, and observe that viscous stresses dominate over inertial stresses, provided that $Re \ll \alpha$. Assuming rapid flow field decay, i.e. viscous stresses remain dominant over inertial stresses throughout the fluid, they derive an implicit analytic expression for the force by a regular perturbation expansion of the Navier-Stokes equations in the small parameter Re. They show that this assumption is valid for the lateral migration of a sphere in flow through a cylinder with arbitrary cross section. Subsequently, they arrive at an integral formula for the lift force for a neutrally buoyant sphere, but they do not evaluate the integrals to determine how lift forces vary across the channel, or how they depend on particle size. Additionally, [53] extended the theory of [62] to non-neutrally buoyant particles by considering a finite slip velocity.

[32] were the first to explicitly calculate the lift force on a particle in the presence of channel walls, by developing an asymptotic theory for a particle in 2D Couette and Poiseuille flows. Since there are multiple scales for the dynamics in the particle-channel system, Ho & Leal introduce the particle Reynolds number $Re_p = \alpha^2 Re$. They observe that provided $Re_p \ll \alpha^2$, viscous stresses dominate over inertial stresses throughout the fluid filled domain. They develop a scaling law for the lift force as a function of the particle position by a regular perturbation series expansion in powers of Re_p. Each term in this expansion can be expanded

6

study	α	Re	Re_p	p	Comments
Rubinow & Keller [61]	N/A	N/A	$\ll 1$	5	Uniform flow and absence of walls
Saffman [62]	N/A	N/A	$\ll 1$	2	Wall effect: particle lags behind fluid
Cox & Brenner [18]	$\ll 1$	$\ll 1$	$\ll \alpha^2$	-	Implicit analytic force expression
Ho & Leal[32]	$\ll 1$	$\ll 1$	$\ll \alpha^2$	4	2D geometry
Vasseur & Cox [75]	$\ll 1$	$\ll 1$	$\ll \alpha^2$	-	Agrees with [32] away from wall
Cox & Hsu [17]	$\ll 1$	$\ll 1$	$\ll \alpha^2$	-	Agrees with [32] near wall
Schonberg & Hinch [63]	$\ll 1$	$O(1)$	$\ll 1$	4	Matched asymptotics
McLaughlin [53]	N/A	N/A	$\ll 1$	2	Extends [62] for finite slip velocity
Hogg [33]	$\ll 1$	$O(1)$	$\ll \alpha$	4	Non-neutrally buoyant particles
Asmolov [2]	$\ll 1$	$O(10^3)$	$\ll 1$	4	Extends [63] for large Re
Di Carlo *et al.* [23]	$O(1)$	$O(10^2)$	$O(10)$	3	3D numerics and experiments
Hood *et al.* [36]	$O(1)$	$O(10^2)$	$O(10)$	-	Reconciles with $\alpha \ll 1$ theory

Table 2.1: A comparison of the parameters α, Re, and Re_p, and the value of the exponent p for the scaling law $f \sim \rho U^2 a^p$, for various studies, where ρ is the fluid density, U is the characteristic flow velocity, and a is the particle radius.

in powers of α. Retaining only leading order terms, they find that lift force $F_L \sim \rho U_m^2 \alpha^2 a^2$, where ρ is the fluid density, U_m is the maximum velocity of the background flow and a is the particle radius, i.e. that lift force scales with the fourth power of particle diameter.

Later computations by [75] apply the result of [18] to a spherical particle flowing between two parallel plates. Provided $Re_p \ll \alpha^2$, only the inner expansion is needed to calculate the first term in the expansion for the migration velocity. The migration velocity is computed as a Fourier integral and no definite scaling law for the lift force is derived. However, they compare their numerical results to those of [32] and have good agreement, except near the wall. Similarly, by considering a particle near a single wall and using the results of [18], [17] calculate the migration velocity of a particle near a the wall. They do not derive a scaling law for the force, but their numerical results compare well to those of [32] near the wall.

Although early theory assumed $Re \ll 1$, in inertial microfluidic devices, and in the experiments of [64], the channel Reynolds number ranges from 1-700. The first theory capable of describing migration of particles in these moderate Reynolds number flows was developed by [63] who assumed small particle size ($\alpha \ll 1$) and particle Reynolds number ($Re_p = \alpha^2 Re \ll 1$), but allowed for Reynolds number $Re = O(1)$. For particles in a 2D Poiseuille flow, they separate the flow field into inner and outer regions. In the inner region, at distances $O(a)$ from the particle, the viscous stresses are dominant. In the outer region, at distances $a/Re_p^{-1/2}$ from the particle, inertial stresses become co-dominant with viscous stresses. In this outer region, the particle's disturbance of the flow field is weak enough to be linearized around the base flow, reducing the Navier-Stokes equation to Oseen's linearized equations [3]. Although the authors solve for the inertial migration velocity for a force free particle, their calculation can readily be adapted to calculate the lift force, and again predicts $F_L \sim \rho U^2 \alpha^2 a^2$; i.e. that lift force scales with the fourth power of particle size. [33] extended the analysis of [63] to non-neutrally buoyant particles, while [2] extended the theory of [63] to large Re.

In inertial microfluidic experiments particle diameters may not be small compared to the channel width and particle Reynolds numbers Re_p can reach values of 10-20. To determine lift forces in this experimentally relevant regime, and to consider focusing in three-dimensional flows, [23] performed finite element simulations for particles in square channels. They varied Reynolds Re number between 20 and 80 and the ratio of particle size to channel size α between 0.05 and 0.2. They find that unlike circular pipes, which focus particles to an annulus, square channels focus particles to four symmetrically arranged positions. For particles near the channel center, numerical fitting of the numerical data generates the power law $F_L \sim \rho U^2 \alpha a^2$, asserting that the lift force F_L increases with a^3 rather than a^4. For particles closer to the channel walls they find different exponents for the scaling of lift force with particle size, depending on particle position. The different exponent in the scaling casts doubt on the use of any of the previous asymptotic theories. Additionally, [23] explore experimentally and numerically how the focusing position of the particle varies with particle

size; an observation that is integral to inertial separation devices, but which is not considered in asymptotic theory.

In this paper we explicitly compute the dominant balances in the equations of motion of the particle to show that the asymptotics of [32] were essentially correct, and hold for a much larger parameter space of Re and α than the authors realized. Specifically, viscous and pressure stresses dominate over inertial stresses over the entire width of the channel; and the drag force on the particle can be computed by regular perturbation of the equations of slow creeping flow. We perform this regular perturbation analysis to derive asymptotic expressions for the lift force that are quantitatively accurate up to $Re = 80$, and with maximum particle size limited only by the proximity of the walls. Our theory also predicts how focusing position depends on particle radius. We show that the scaling observed by [23] is actually a serendipitous fitting to a perturbation series in α by a single apparent scaling law.

2.2   Equations of motion

We model flow through an infinitely long square channel of side length ℓ. A three dimensional Poiseuille flow $\bar{\mathbf{u}}'$ flowing in the $z'-$direction, is disturbed by a rigid sphere of radius a (figure 3.1a). Here we use primes to denote dimensional variables. We denote the fluid viscosity by μ, fluid density by ρ, and the center-line velocity of the background flow by U_m. The particle is located at $(x'_0, y'_0, 0)$ and is allowed to translate in the $z'-$ direction with velocity $\mathbf{U}'_p = U'_p \mathbf{e_{z'}}$, and rotate with angular velocity $\mathbf{\Omega}'_p$, until it is drag free and torque free. The objective of this paper is to calculate the lift forces acting on the particle in the $x'-$ and $y'-$ directions.

There are three important dimensionless parameters: (i) the dimensionless ratio of particle radius to channel diameter $\alpha = a/\ell$, (ii) the channel Reynolds number $Re = U_m \ell / \nu$, and (iii) the particle Reynolds number $Re_p = U_m a^2 / \ell \nu$. Here we write $\nu = \mu / \rho$ for the kinematic viscosity. In common with previous theory [18, 32, 63] we will perform dual perturbation
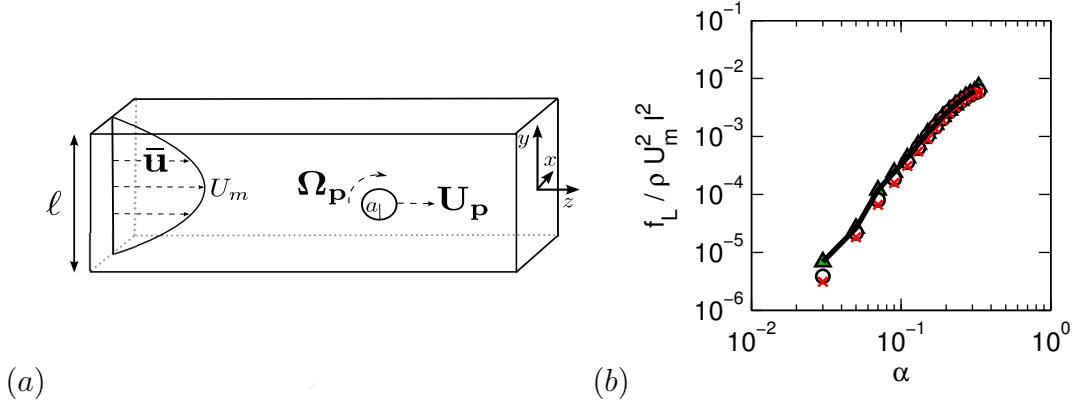
Figure 2.1: (a) The physical system for the flow around a particle suspended in a square channel. (b) We numerically compute the lift force F_L as a function of particle size α for various Reynolds numbers, $Re = 10$ (green triangles), $Re = 50$ (circles), and $Re = 80$ (red x's). The curves collapse when lift force is scaled by $\rho U_m^2 \ell^2$, but the curves are neither a power law with exponent 3 nor exponent 4. A regular perturbation expansion that we computed numerically fits the data extremely well (solid black line).

expansions in Re_p and α, assuming that both quantities are asymptotically small. In inertial microfluidic experiments [23], particle diameters may be comparable with the channel dimensions. We will show that our expansions converge even at the moderate values of α accessed in these experiments.

The background flow, $\bar{\mathbf{u}}'$, is square channel Poiseuille flow [55], and takes the form $\bar{\mathbf{u}}' = \bar{u}'(x', y')\mathbf{e}_{z'}$, where $\bar{u}'$ defined by:

$$\bar{u}'(x', y') = U_m \left[-\frac{1}{2}\left(y'^2 - \left(\frac{\ell}{2a}\right)^2\right) \right. \tag{2.1}$$
$$\left. + \sum_{n=0}^{\infty} \frac{-4\ell^2(-1)^n \cosh\left(\frac{(2n+1)\pi a x'}{\ell}\right)}{(2n+1)^3\pi^3 a^2 \cosh\left(\frac{(2n+1)\pi}{2}\right)} \cos\left(\frac{(2n+1)\pi a y'}{\ell}\right) \right].$$

The velocity $\bar{\mathbf{u}}'$ and pressure $\bar{p}'$ solve the Stokes equations with boundary condition $\bar{\mathbf{u}}' = \mathbf{0}$ on the channel walls. We will also need the Taylor series expansion for $\bar{u}'$ around the center

of the particle:

$$\bar{u}'(x', y') = \beta' + \gamma'_x(x' - x'_0) + \gamma'_y(y' - y'_0) \tag{2.2}$$
$$+ \delta'_{xx}(x' - x'_0)^2 + \delta'_{xy}(x' - x'_0)(y' - y'_0) + \delta'_{yy}(y' - y'_0)^2 + O(r'^3)$$

To illustrate the reference frame of the equations we will use later, we first list the dimensionless equations of motion and boundary conditions for the velocity and pressure fields $\mathbf{u}''$ and p'' expressed in particle-fixed coordinates. We non-dimensionalise these equations by scaling velocities by $U_m a/\ell$, lengths by a, and pressures by $\mu U_m/\ell$:

$$
\begin{aligned}
\nabla^2 \mathbf{u}'' - \nabla p'' &= Re_p\left[(\mathbf{u}'' + \mathbf{U}_p) \cdot \nabla \mathbf{u}''\right], \\
\nabla \cdot \mathbf{u}'' &= 0, \\
\mathbf{u}'' &= \boldsymbol{\Omega}_p \times \mathbf{r}'' \quad \text{on} \quad r'' = 1, \\
\mathbf{u}'' &= -\mathbf{U}_p \quad \text{on the walls}, \\
\mathbf{u}'' &= \bar{\mathbf{u}} - \mathbf{U}_p \quad \text{as} \quad z'' \to \pm\infty.
\end{aligned}
\tag{2.3}
$$

Now we introduce the disturbance velocity and pressure fields $\mathbf{u} = \mathbf{u}'' - \bar{\mathbf{u}} + \mathbf{U}_p$ and $p = p'' - \bar{p}$, in which the background flow $\bar{\mathbf{u}} - \mathbf{U}_p$ (as measured in this reference frame) is subtracted from $\mathbf{u}''$. For reference, the fluid velocity in the lab frame is given by: $\mathbf{v} = \mathbf{u} + \bar{\mathbf{u}}$. We then obtain the equations of motion and boundary conditions that will be used throughout this paper:

$$
\begin{aligned}
\nabla^2 \mathbf{u} - \nabla p &= Re_p\left(\bar{\mathbf{u}} \cdot \nabla \mathbf{u} + \mathbf{u} \cdot \nabla \bar{\mathbf{u}} + \mathbf{u} \cdot \nabla \mathbf{u}\right), \\
\nabla \cdot \mathbf{u} &= 0, \\
\mathbf{u} &= \boldsymbol{\Omega_p} \times \mathbf{r} - \bar{\mathbf{u}} + \mathbf{U_p} \quad \text{on} \quad r = 1, \\
\mathbf{u} &= \mathbf{0} \quad \text{on the walls}, \\
\mathbf{u} &= \mathbf{0} \quad \text{as} \quad z \to \pm\infty.
\end{aligned}
\tag{2.4}
$$

11

We call the variables that appear in (2.4) the inner variables. Appendix A.1 summarizes the notations used for dimensionless and dimensional variables.

We formulated (2.4) as a finite element model (FEM) with $\sim 650,000$ linear tetrahedral elements, and solved for $\mathbf{u}$ and p using Comsol Multiphysics (COMSOL, Los Angeles) in a rectangular domain with dimensions $\frac{\ell}{a} \times \frac{\ell}{a} \times 5\frac{\ell}{a}$, prescribing $\mathbf{u}$ at the inlet $z = -5\frac{\ell}{a}$, and imposing neutral boundary conditions (vanishing stress) at the outlet $z = +5\frac{\ell}{a}$. In the FEM, we vary U_p and $\mathbf{\Omega}_p$ until there is no drag force or torque on the particle. The FEM Lagrange multipliers, which enforce the velocity boundary condition on the particle, are used to compute the lift force F_L on the drag free and force free particle. [6] rigorously demonstrates the accuracy of flux calculations from Lagrange multipliers for a Poisson's equation with Dirichlet boundary conditions. Additionally, we discuss accuracy tests of the FEM discretization for our problem in Appendix A.2.

First, we consider the lift force for particles located on the line of symmetry $x_0 = 0$. Fixing particle position y_0, we found curves of lift force F_L against particle size a collapsed for different Reynolds numbers. Particles in different positions have different apparent scaling's for F_L as a function of a (figure 2.5a-b). By assaying a large range of particle sizes α we see that the empirical fit $F_L \sim \rho U^2 a^3$ observed by [23] is not asymptotic as $a \to 0$. The data for smallest particle sizes ($\alpha < 0.07$) are consistent with a scaling law of $F_L \sim \rho U^2 a^4 / \ell^2$ as predicted by [32] and [63], but extrapolation of the asymptotic force law to the moderate particle sizes used in real inertial microfluidic devices ($\alpha \approx 0.1 - 0.3$) over-predicts the lift force by more than an order of magnitude.

2.3 Dominant balances in the equations of motion

The governing equation (2.4) is a balance between momentum flux and the pressure and viscous stresses. Testing the hypothesis that two of these three contributions might form a dominant balance within the equation, we plotted the resultants of the three fluxes as functions of distance from the particle. Specifically, we integrate the ℓ_2 norm of each flux
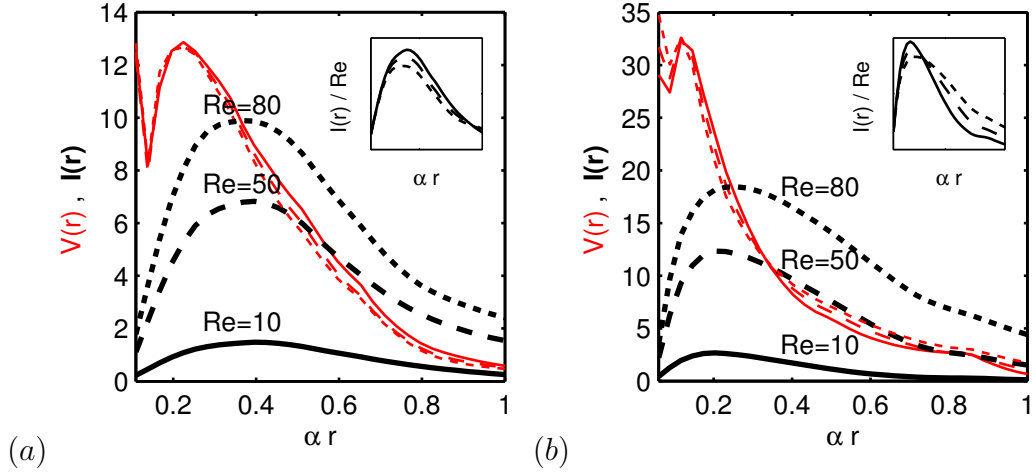
Figure 2.2: We examine the dominant balance of the Navier-Stokes equation for (a) a particle near the channel center ($y_0 = 0.15/\alpha$ and $\alpha = 0.11$), and (b) a particle near the channel walls ($y_0 = 0.35/\alpha$ and $\alpha = 0.06$). The viscous stresses $V(r)$ for various Reynolds numbers are plotted as thin red lines, and the inertial stresses $I(r)$ are plotted as thick black lines. Reynolds numbers are indicated by line style, $Re = 10$ solid line, $Re = 50$ dashed line, and $Re = 80$ dotted line. The inset figures show that the inertial stresses $I(r)$ collapse when scaled by Re, suggesting that the high Reynolds number dynamics are determined by the low Reynolds number dynamics.

over spherical control surfaces centered at the particle. Let S_r be the boundary of a sphere of radius r centered at the origin, and define the ℓ_2 norm by $\|\mathbf{u}\|_2 = \sqrt{u^2 + v^2 + w^2}$. Then the dimensionless viscous stress resultant acting on the sphere S_r is defined by:

$$V(r) = \int_{S_r} \|\nabla \mathbf{u} \cdot \mathbf{n}\|_2 \mathrm{d}s \; , \tag{2.5}$$

and the dimensionless inertial term $I(r)$ stress resultant by:

$$I(r) = Re_p \int_{S_r} \|[(\bar{\mathbf{u}} - \mathbf{U_p})\mathbf{u} + \mathbf{u}(\bar{\mathbf{u}} - \mathbf{U_p}) + \mathbf{u}\mathbf{u}] \cdot \mathbf{n}\|_2 \mathrm{d}s \tag{2.6}$$

The integrand in $I(r)$ is chosen to have divergence equal to the right hand side of (2.4), and we pick a form of the inertial flux that decays in ℓ_2 norm as $r \to \infty$.

Numerically evaluating these two terms as well as $\frac{1}{r} \int_{S_r} \|p\mathbf{n}\|_2 \, \mathrm{d}s$ we find that contrary

to the predictions of [32] and [63] that at moderate channel Reynolds numbers, the viscous and pressure stress resultants are numerically larger than the momentum flux. In particular there is no region in which $V(r)$ and $I(r)$ are co-dominant at $Re = 10$ (figure 2.2). Indeed, even at higher Reynolds numbers ($Re = 50$, 80) for which inertial stresses are numerically larger than viscous stresses, inertial stresses can be collapsed onto a single curve (see inset of figures 2.2a-b) by rescaling with Re. This scaling suggests that the underlying dynamics, even at moderate values of Re, are inherited from the small Re dominant balance of pressure and viscous stresses. Dominance of viscous stresses over inertial stresses is surprising because as [32] noticed, the resulting dominant balance equations are not self-consistent for isolated particles in unbounded fluid flow.

We will now present a first order estimate of the size of the domain in which inertial stresses may be expected to be dominant. The slowest decaying component of the disturbance flow associated with a force free particle on the plane of symmetry ($x_0 = 0$) is given by the stresslet flow [3, 43]:

$$\mathbf{u}_{\text{stresslet}} = \frac{5\gamma_y(y - y_0)z\mathbf{r}}{2r^5} = O\left(\frac{1}{r^2}\right).$$ (2.7)

Recall that γ_y is the strain rate, defined in (5.8). For this flow field, the viscous stress term in (2.4) decays with distance like:

$$V(r) \sim O(\nabla \mathbf{u}_{\text{stresslet}}) \sim O\left(\frac{1}{r^3}\right),$$ (2.8)

whereas the inertial stresses vary with distance like:

$$I(r) \sim O(Re_p(\mathbf{u}_{\text{stresslet}})(\bar{\mathbf{u}} - \mathbf{U_p})) \sim O\left(\frac{Re_p}{r}\right).$$ (2.9)

We define the cross-over radius, r_*, to be the distance at which the viscous and inertial stresses are comparable,

$$r_* = O\left(\frac{1}{Re_p^{1/2}}\right).$$ (2.10)

In order to compare the cross-over radius to the width of the channel we consider when $\alpha r_* = O(1/Re^{1/2})$ is equal to one. To ensure that viscous stresses dominate over inertial stresses over the channel cross-section (i.e. $\alpha r_* \gg 1$) Ho & Leal restrict to cases where
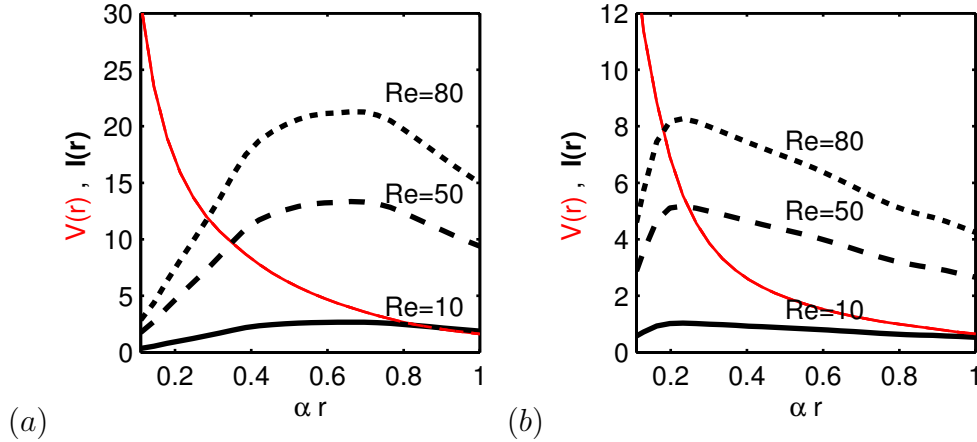
Figure 2.3: We examine the dominant balance that arises from the stresslet approximation of the flow for (a) a particle near the channel center ($y_0 = 0.15/\alpha$ and $\alpha = 0.11$), and (b) a particle near the channel walls ($y_0 = 0.35/\alpha$ and $\alpha = 0.06$). The viscous stresses $V(r)$ for various Reynolds numbers are plotted as thin red lines, and the inertial stresses $I(r)$ are plotted as thick black lines. Reynolds numbers are indicated by line style, $Re = 10$ solid line, $Re = 50$ dashed line, and $Re = 80$ dotted line.

$Re \ll 1$. The asymptotic analysis of [63] allows that $Re = O(1)$, but at the cost of needing to separately model and match the flows at $O(1)$ distances from the particle where viscous stresses are dominant, and at $O(1/Re^{1/2})$ distances where inertial and viscous stresses must both be included in the dominant balance.

However, the predicted cross over radius falls short of the numerical cross over radius (fig 2.2, table 2.2). There are two explanations for the dominance of viscous stresses over inertial in these experimental geometries. First, the above estimates do not consider the coefficients in the stresslet; merely the order of magnitude of the terms. Second, although the stresslet describes the flow disturbance for a force free particle in an unbounded fluid, the leading order flow is considerably altered by the presence of the channel walls. Below we demonstrate that both explanations contribute to the dominance of viscous stresses throughout the channel cross section, pushing the cross-over radius r^* out beyond the channel walls (table 2.2).

15
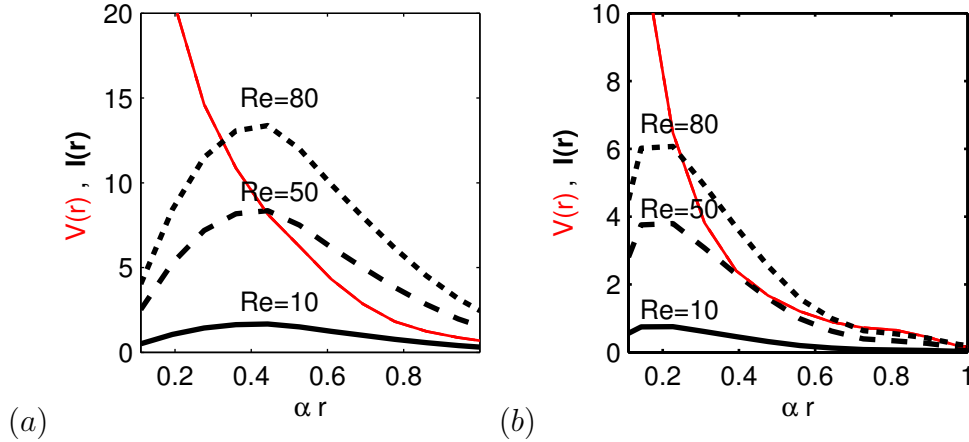
Figure 2.4: We examine the dominant balance that arises from the stresslet and first wall correction of the flow for (a) a particle near the channel center ($y_0 = 0.15/\alpha$ and $\alpha = 0.11$), and (b) a particle near the channel walls ($y_0 = 0.35/\alpha$ and $\alpha = 0.06$). The viscous stresses $V(r)$ for various Reynolds numbers are plotted as thin red lines, and the inertial stresses $I(r)$ are plotted as thick black lines. Reynolds numbers are indicated by line style, $Re = 10$ solid line, $Re = 50$ dashed line, and $Re = 80$ dotted line.

2.3.1 Role of the stresslet constants

We compute $I(r)$ and $V(r)$ numerically for the stresslet flow field (i.e. substitute $\mathbf{u} = \mathbf{u}_{\mathrm{stresslet}}$ in equations (2.5-2.6)). We examine two representative cases; a medium sized particle near the channel center ($y_0 = 0.15/\alpha$, $\alpha = 0.11$) (figure 2.3a), and a small particle near the channel wall ($y = 0.35/\alpha$, $\alpha = 0.06$) (figure 2.3b). For $Re = 10$, in both cases the inertia is significantly smaller than the viscous stress throughout the channel. At larger values of Re, $I(r)$ eventually exceeds $V(r)$, but the cross-over radius r_* is much larger than simple order of magnitude estimates would suggest (table 2.2).

2.3.2 Role of Wall Effects

To estimate how wall modifications of the disturbance flow affect the dominant balances in Eq.(2.4), we numerically computed the first wall correction. That is, we substitute into

16

equations (2.5-2.6) $\mathbf{u} = \mathbf{u}_{\text{stresslet}} + \mathbf{u}_{\text{image}}$, where $\mathbf{u}_{\text{image}}$ is a solution of Stokes' equations with boundary condition $\mathbf{u}_{\text{image}} = -\mathbf{u}_{\text{stresslet}}$ on the channel walls. We examine the same two representative cases as in §2.3.1: $(y_0 = 0.15/\alpha, \alpha = 0.11)$ and $(y_0 = 0.35/\alpha, \alpha = 0.06)$ (figure $2.4a - b$). For $Re = 10$, in both cases the inertia is significantly smaller than the viscous stress throughout the channel. At larger values of Re, $I(r)$ eventually exceeds $V(r)$, but the cross-over radius r_* is larger than that predicted from the stresslet coefficients (table 2.2).

We can rationalize the larger values of the cross-over radius αr_* by considering the boundary conditions on the channel walls. Because the velocity field $\mathbf{u}$ vanishes on the channel walls, the inertial stresses vanish there. $I(r)$ is therefore suppressed at larger radii. We see less suppression of $V(r)$, presumably because viscous stresses do not need to vanish on the channel walls. Suppression of $I(r)$ increases the cross-over radius at which inertial stresses must be considered in the dominant balance.

2.4   A series expansion for the inertial lift force

Our careful evaluation of the stresslet prefactors and wall-contributions shows that viscous stresses are dominant over inertial stresses over much of the fluid filled domain, including at much greater distances from the particle than previous estimates have suggested. We therefore develop an asymptotic theory, based on [18] and [32], in which the flow field, $\mathbf{u}$, pressure, p, particle velocity $\mathbf{U_p}$, and rotation $\mathbf{\Omega_p}$ are expanded in powers of Re_p, with inertia completely neglected in the leading order equations:

$$\mathbf{u} = \mathbf{u}^{(0)} + Re_p\mathbf{u}^{(1)} + \dots \quad , \quad p = p^{(0)} + Re_p p^{(1)} + \dots \quad , \qquad \text{etc.} \qquad (2.11)$$

Notice that this is an expansion in the particle Reynolds number Re_p and not the channel Reynolds number Re. Although in experiments the channel Reynolds number is typically large, the expansion is formally valid provided that α^2 is small enough that $Re_p = \alpha^2 Re \lesssim 1$. In fact when we compare our theory with numerical simulations in §2.4.5 we find that the perturbative series gives a good approximation to the lift force even for $Re_p = 7$ (Fig. 3.1b).

17

Cross over radius αr_*	$y_0 = 0.15/\alpha$			$y_0 = 0.35/\alpha$		
		$\alpha = 0.11$			$\alpha = 0.06$	
Re	10	50	80	10	50	80
$\alpha r_* = 1/Re^{1/2}$	0.31	0.14	0.11	0.31	0.14	0.11
Stresslet with constants (from figure 2.3)	0.9	0.4	0.3	1	0.3	0.2
Stresslet with wall effects (from figure 2.4)	>1	0.45	0.35	>1	0.4	0.3
NSE with wall effects (from figure 2.2)	>1	0.6	0.4	>1	0.4	0.3

Table 2.2: The cross-over radius $\alpha\,r_*$ at which $I(r) \geq V(r)$ computed for $Re = 10, 50, 80$ using the following methods: (i) Ho & Leal's calculation using the stresslet, (ii) our calculation using the stresslet, (iii) our calculation using the stresslet and first wall correction, and (iv) our calculation using the numerical solution to the full Navier-Stokes equation (NSE).

First we compute the first two terms in the perturbative series $\mathbf{u}^{(0)} + Re_p \mathbf{u}^{(1)}$ numerically, showing that retaining these two terms gives the lift force quantitatively accurately over the entire dynamical range of experiments.

Series expanding (2.4) and collecting like terms in Re_p we arrive at equations for $(\mathbf{u}^{(0)}, p^{(0)})$, the first order velocity and pressure:

$$\nabla^2 \mathbf{u}^{(0)} - \nabla p^{(0)} = \mathbf{0}, \qquad \nabla \cdot \mathbf{u}^{(0)} = 0,$$

$$\mathbf{u}^{(0)} = \mathbf{U_p}^{(0)} + \mathbf{\Omega_p}^{(0)} \times \mathbf{r} - \bar{\mathbf{u}} \text{ on } r = 1, \tag{2.12}$$

$$\mathbf{u}^{(0)} = \mathbf{0} \text{ on channel walls and as } z \to \pm\infty.$$

Similarly, the next order velocity and pressure $(\mathbf{u}^{(1)}, p^{(1)})$ satisfy the equations:

$$\nabla^2 \mathbf{u}^{(1)} - \nabla p^{(1)} = (\bar{\mathbf{u}} \cdot \nabla \mathbf{u}^{(0)} + \mathbf{u}^{(0)} \cdot \nabla \bar{\mathbf{u}} + \mathbf{u}^{(0)} \cdot \nabla \mathbf{u}^{(0)}), \qquad \nabla \cdot \mathbf{u}^{(1)} = 0,$$

$$\mathbf{u}^{(1)} = \mathbf{U_p}^{(1)} + \mathbf{\Omega_p}^{(1)} \times \mathbf{r} \text{ on } r = 1, \tag{2.13}$$

$$\mathbf{u}^{(1)} = \mathbf{0} \text{ on channel walls and as } z \to \pm\infty.$$

For both cases, we only need to solve the Stokes equations with a known body force term. In (2.12), the body force term is equal to $\mathbf{0}$; in (2.13) the body force term is equal to the

inertia of flow $\mathbf{u}^{(0)}$.

In fact we can apply Lorentz's reciprocal theorem [45] to calculate the lift force associated with $\mathbf{u}^{(1)}$ without needing to directly solve (2.13). We define the test fluid flow $(\hat{\mathbf{u}}, \hat{p})$ representing Stokes flow around a sphere moving with unit velocity in the y-direction: viz satisfying (2.12) with the velocity condition on the sphere replaced by $\hat{\mathbf{u}} = \boldsymbol{e}_y$. If $\boldsymbol{\sigma}^{(1)}$ and $\hat{\boldsymbol{\sigma}}$ are the viscous stress tensors associated with the flow fields $(\mathbf{u}^{(1)}, p^{(1)})$ and $(\hat{\mathbf{u}}, \hat{p})$ respectively: $\boldsymbol{\sigma}^{(1)} = \nabla\mathbf{u}^{(1)} + (\nabla\mathbf{u}^{(1)})^T - p^{(1)}\mathbf{1}$, etc., and $\hat{\mathbf{e}}$ and $\mathbf{e}^{(1)}$ the respective rate-of-strain tensors: $\mathbf{e}^{(1)} = \frac{1}{2}[\nabla\mathbf{u}^{(1)} + (\nabla\mathbf{u}^{(1)})^T]$, etc., then by the divergence theorem, the following relation is valid for any volume V enclosed by a surface S.

$$\int_S \left(\boldsymbol{n} \cdot \hat{\boldsymbol{\sigma}} \cdot \mathbf{u}^{(1)} - \boldsymbol{n} \cdot \boldsymbol{\sigma}^{(1)} \cdot \hat{\mathbf{u}}\right) \mathrm{ds} = \int_V \left[\nabla \cdot \left(\hat{\boldsymbol{\sigma}} \cdot \mathbf{u}^{(1)}\right) - \nabla \cdot \left(\boldsymbol{\sigma}^{(1)} \cdot \hat{\mathbf{u}}\right)\right] \mathrm{dv}. \qquad (2.14)$$

By setting V equal to the fluid filled domain and substituting boundary conditions from (2.4), we deduce:

$$\begin{aligned}
\mathbf{U}_p^{(1)} \cdot \int_S (\hat{\boldsymbol{\sigma}} \cdot \boldsymbol{n}) \, \mathrm{ds} &+ \int_S \left(\boldsymbol{\Omega}_p^{(1)} \times \mathbf{r}\right) \cdot \hat{\boldsymbol{\sigma}} \cdot \boldsymbol{n} \, \mathrm{ds} - \mathbf{e_y} \cdot \int_S \boldsymbol{\sigma}^{(1)} \cdot \boldsymbol{n} \, \mathrm{ds} \\
&= \int_V \left[\left(\nabla \cdot \boldsymbol{\sigma}^{(1)}\right) \cdot \hat{\mathbf{u}} + \boldsymbol{\sigma}^{(1)} : \hat{\mathbf{e}} - (\nabla \cdot \hat{\boldsymbol{\sigma}}) \cdot \mathbf{u}^{(1)} - \hat{\boldsymbol{\sigma}} : \mathbf{e}^{(1)}\right] \mathrm{dv}.
\end{aligned} \qquad (2.15)$$

On the left hand side of the equation, the first term is zero by symmetry. Similarly, the integrand of the second term can be rearranged:

$$\left(\boldsymbol{\Omega}_p^{(1)} \times \mathbf{r}\right) \cdot \hat{\boldsymbol{\sigma}} \cdot \boldsymbol{n} = \boldsymbol{\Omega}_p^{(1)} \cdot \left(\mathbf{r} \times \hat{\boldsymbol{\sigma}} \cdot \boldsymbol{n}\right), \qquad (2.16)$$

which also integrates to zero. On the right hand side of (2.15), the third term is zero by definition (since $\hat{\mathbf{u}}$ solves the Stokes equations). Furthermore, we can rearrange the second and fourth terms:

$$\boldsymbol{\sigma}^{(1)} : \hat{\mathbf{e}} - \hat{\boldsymbol{\sigma}} : \mathbf{e}^{(1)} = 2\mathbf{e}^{(1)} : \hat{\mathbf{e}} - p^{(1)}\nabla \cdot \hat{\mathbf{u}} - 2\hat{\mathbf{e}} : \mathbf{e}^{(1)} + \hat{p}\nabla \cdot \mathbf{u}^{(1)} = 0 \qquad (2.17)$$

since both flows are incompressible. So, on the right hand side of (2.15), only the first term of the volume integral remains. Using the definitions of $\boldsymbol{\sigma}^{(1)}$ and $\hat{\boldsymbol{\sigma}}$, we obtain the following formula, which we refer to as the reciprocal theorem.

$$\mathbf{e_y} \cdot \mathbf{F_L} = \int_V \hat{\mathbf{u}} \cdot \left(\bar{\mathbf{u}} \cdot \nabla\mathbf{u}^{(0)} + \mathbf{u}^{(0)} \cdot \nabla\bar{\mathbf{u}} + \mathbf{u}^{(0)} \cdot \nabla\mathbf{u}^{(0)}\right) \mathrm{dv} \qquad (2.18)$$

19
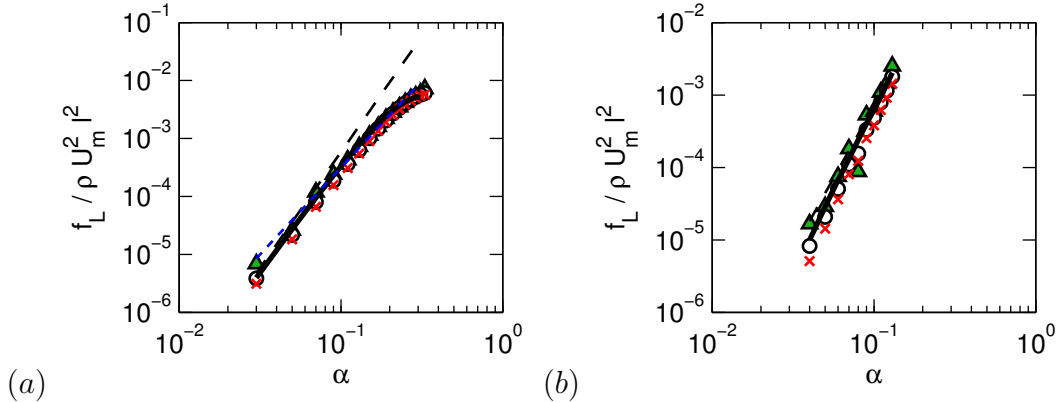
Figure 2.5: We compute numerically the scaled lift force $F_L/\rho U_m^2 \ell^2$ using the Navier-Stokes equations in (2.4) as a function of particle size α for various channel Reynolds numbers, $Re = 10$ (green triangles), $Re = 50$ (circles), and $Re = 80$ (red x's). The black dashed line represents a scaling law with exponent 4, i.e. $F_L \sim \rho U_m^2 \alpha^2 a^2$ as in [32], while the dotted blue line represents a scaling law with exponent 3, i.e. $F_L \sim \rho U_m^2 \alpha a^2$, which is the line of best fit computed in [23]. The solid line represents the regular perturbation expansion computed numerically using the reciprocal theorem in (2.18). We compare all of these force predictions at two locations in the channel, (a) a particle near the channel center ($y_0 = 0.15/\alpha$ and $\alpha = 0.11$), and (b) a particle near the channel walls ($y_0 = 0.35/\alpha$ and $\alpha = 0.06$).

We have now reduced our calculation of the lift force to that of solving two homogeneous Stokes equations and performing a volume integral. Numerically, we let V be the truncated numerical domain modeled by our FEM. Next we solve numerically for $\mathbf{u}^{(0)}$ from (2.12) and $\hat{\mathbf{u}}$. Again, we choose $U_p^{(0)}$ and $\Omega_p^{(0)}$ so that the particle travels force free and torque free. We compute the lift force using the reciprocal theorem in (2.18) for particles at two different channel positions (figure 2.5a-b). We see close quantitative agreement between the lift force computed from the full Navier-Stokes equations and the lift force computed from the reciprocal theorem using the two term expansion in Re_p. The comparison is accurate even when, as for $y_0 = 0.15/\alpha$, there is no simple scaling law for the dependence of F_L upon a (figure 2.5a). In the next section, we develop a model that nevertheless allows analytic evaluation of the lift force.

2.4.1 Approximation of $\mathbf{u}^{(0)}$ and $\hat{\mathbf{u}}$ by method of images

In the previous section we showed that a single, regular perturbation in Re_p of Stokes equations agrees excellently to the numerically computed lift force. We calculated the terms in this perturbation series numerically but to rationally design inertial microfluidic devices, we need an asymptotic theory for how the lift force and the inertial focusing points depend on the size of the particle and its position within the channel. We derive this theory from asymptotic expansion of $\mathbf{u}^{(0)}$ and $\hat{\mathbf{u}}$ in powers of α, the dimensionless particle size. We follow [32] and use the method of reflections to generate expansions in powers of α for the Stokes flow fields appearing in (2.18) [30]:

$$\mathbf{u}^{(0)} = \mathbf{u}_1^{(0)} + \mathbf{u}_2^{(0)} + \mathbf{u}_3^{(0)} + \mathbf{u}_4^{(0)} + \dots , \tag{2.19}$$

with similar expansions for p, $\hat{\mathbf{u}}$, and $\hat{p}$. Here, $\mathbf{u}_1^{(0)}$ is the Stokes solution for a particle in unbounded flow, $\mathbf{u}_2^{(0)}$ is the Stokes solution with boundary condition $\mathbf{u}_2^{(0)} = -\mathbf{u}_1^{(0)}$ on the channel walls, and $\mathbf{u}_3^{(0)}$ is the Stokes solution with boundary condition $\mathbf{u}_3^{(0)} = -\mathbf{u}_2^{(0)}$ on the particle surface, etc. Odd terms impose the global boundary conditions on the particle, whereas even terms impose the global boundary conditions on the channel walls. We will show below that the terms in this series constitute a power series in α.

Since the odd terms in the expansion, $\mathbf{u}_{2i-1}^{(0)}$, are prescribed on the sphere's surface they can be calculated using Lamb's method for solving the flow external to a sphere [44, 30]. This method expands the velocity field as a sum of multipoles located at the sphere center. Namely,

$$\mathbf{u}_{2i-1}^{(0)} = \sum_{n=0}^{\infty} \frac{1}{r^{n+1}} \mathbf{f}_n^i \left(\frac{x - x_0}{r}, \frac{y - y_0}{r}, \frac{z}{r} \right) , \tag{2.20}$$

where each term $\mathbf{f}_n^i / r^{n+1}$ is a combination of the stokeslet n-pole and the source $(n-1)$-pole. We can similarly expand the odd terms of $\hat{\mathbf{u}}$:

$$\hat{\mathbf{u}}_{2i-1} = \sum_{n=0}^{\infty} \frac{1}{r^{n+1}} \mathbf{g}_n^i \left(\frac{x - x_0}{r}, \frac{y - y_0}{r}, \frac{z}{r} \right) . \tag{2.21}$$

The full analytic forms for the $\mathbf{f}_n^1$ and $\mathbf{g}_n^1$ are listed in Appendix A.3. From the analytic form of $\mathbf{u}_1^{(0)}$, we can find $\mathbf{u}_2^{(0)}$ by solving the associated Stokes problem numerically. Given $-\mathbf{u}_2^{(0)}$

21

on the particle surface, we can appeal to Lamb's solution to find $\mathbf{u}_3^{(0)}$, and so on. The same sequence of reflections can be used to expand the reference velocity $\hat{\mathbf{u}}$.

2.4.2   Approximation to the reciprocal theorem integral

Given the Stokes velocities $\mathbf{u}^{(0)}$ and $\hat{\mathbf{u}}$ we can compute the inertial lift force F_L up to terms of $O(Re_p)$ using the reciprocal theorem (2.18). As in [32], it is advantageous to divide the fluid filled domain V into two subdomains, V_1 and V_2, where:

$$V_1 = \{\mathbf{r} \in V : r \le \xi\} \quad \text{and} \quad V_2 = \{\mathbf{r} \in V : r \ge \xi\}. \tag{2.22}$$

The intermediate radius ξ is any parameter satisfying $1 \ll \xi \ll \frac{1}{\alpha}$. Call the corresponding integrals the inner integral and the outer integral, and identify their contributions to the lift force as F_{L_1} and F_{L_2}, respectively ($F_L = F_{L_1} + F_{L_2}$). The division of the integral into inner and outer regions allows one to incorporate varying length scales (a for the inner region and ℓ for the outer region) into our model. Note that, distinct from [63], inertia remains subdominant even in the outer region V_2. In the next two sections, we will separately consider the contributions from the inner and outer integrals.

2.4.3   The Inner Integral

For the inner integral we continue to scale lengths by a, so that $1 \le r \le \xi \ll \alpha^{-1}$. The inner integral can be expressed as the following expansion in α.:

$$F_{L_1} = \rho U_m^2 a^2 (h_4 \alpha^2 + h_5 \alpha^3 + \dots) \quad . \tag{2.23}$$

In order to calculate the terms h_4 and h_5, we sort the terms of the Stokes velocities by leading order in α. The terms contributing at $O(\alpha^2)$ in the inner region are:

$$\mathbf{u}_1^{(0)} \sim \alpha \left(\frac{1}{r^2} \mathbf{f}_1^1 + \frac{1}{r^4} \mathbf{f}_3^1 \right), \qquad \hat{\mathbf{u}}_1 \sim \frac{1}{r} \mathbf{g}_0^1 + \frac{1}{r^3} \mathbf{g}_2^1, \qquad \bar{\mathbf{u}} \sim \gamma \alpha r. \tag{2.24}$$

All of these terms are known analytically (see Appendix A.3), and it can be shown that their contribution to the inner integral evaluates to zero, i.e. $h_4 = 0$.

At $O(\alpha^3)$ the velocity terms contributing to calculation of h_5 are:

$$\mathbf{u}_1^{(0)} \sim \alpha \left(\frac{1}{r^2}\mathbf{f}_1^1 + \frac{1}{r^4}\mathbf{f}_3^1 \right) + \alpha^2 \left(\frac{1}{r^3}\mathbf{f}_2^1 + \frac{1}{r^5}\mathbf{f}_4^1 \right), \qquad \bar{\mathbf{u}} \sim \gamma \alpha r + \delta \alpha^2 r^2,$$

$$\hat{\mathbf{u}}_1 \sim \frac{1}{r}\mathbf{g}_0^1 + \frac{1}{r^3}\mathbf{g}_2^1 , \qquad \hat{\mathbf{u}}_2 \sim \alpha \mathcal{SI} \left[\frac{1}{r}\mathbf{g}_0^1 \right]_0 , \qquad \hat{\mathbf{u}}_3 \sim \alpha \left(\frac{1}{r}\mathbf{g}_0^3 + \frac{1}{r^3}\mathbf{g}_2^3 \right). \tag{2.25}$$

where we define $\mathbf{v} \equiv \mathcal{SI}[\mathbf{u}]$ as the image of the function $\mathbf{u}$, and we define $\mathbf{v}_0 \equiv \mathcal{SI}[\mathbf{u}]_0$ as the velocity $\mathbf{v}$ evaluated at the particle center. That is, $\mathbf{v}$ solves the Stokes equations with boundary condition $\mathbf{v} = -\mathbf{u}$ on the channel walls, and $\mathbf{v}_0 = \mathbf{v}(x_0, y_0, 0)$. We determine $\mathcal{SI}\left[\frac{1}{r}\mathbf{g}_0^1 \right]$ numerically, by discretizing Stokes equations as a FEM, with quadratic elements for the velocity field and linear elements for the pressure field, and solving the FEM in Comsol Multiphysics.

The $O(\alpha^3)$ contribution to the inner integral is:

$$\begin{aligned} h_5 &= \int_{\mathbb{R}^3} (\hat{\mathbf{u}}_1 + \hat{\mathbf{u}}_2 + \hat{\mathbf{u}}_3) \cdot \left(\bar{\mathbf{u}} \cdot \nabla \mathbf{u}_1^{(0)} + \mathbf{u}_1^{(0)} \cdot \nabla \bar{\mathbf{u}} + \mathbf{u}_1^{(0)} \cdot \nabla \mathbf{u}_1^{(0)} \right) \mathrm{d}v \\ &= \int_{\mathbb{R}^3} \hat{\mathbf{u}}_1 \cdot \left(\bar{\mathbf{u}} \cdot \nabla \mathbf{u}_1^{(0)} + \mathbf{u}_1^{(0)} \cdot \nabla \bar{\mathbf{u}} + \mathbf{u}_1^{(0)} \cdot \nabla \mathbf{u}_1^{(0)} \right) \mathrm{d}v \end{aligned} \tag{2.26}$$

where we have made use of the fact that the contributions to the integral from $\hat{\mathbf{u}}_2$ and $\hat{\mathbf{u}}_3$ evaluate to zero. Since all of the terms in the integrand are $O(r^3)$ as $r \to \infty$, we can take $\xi \to \infty$; viz, replace integration over V_1 by integration over $\mathbb{R}^3$. In doing so, we pick up an error that is $O(1/\xi)$. We neglect this contribution, since $\xi \gg 1$; in fact the error terms can be shown to cancel with corresponding contributions from the outer integral if expansions are continued to higher order powers of α. Evaluating the final integral, we obtain:

$$F_{L_1} = \frac{\rho U_m^2 h_5 a^5}{\ell^3} + O(a^6) , \tag{2.27}$$

where

$$h_5 = -\frac{26171\pi\gamma_y^2}{277200} - \frac{53\pi\gamma_y\delta_{xx}}{1728} - \frac{283\pi\gamma_y\delta_{yy}}{3150} \tag{2.28}$$

is $O(1)$, and depends only on the location of the particle. Recall that the constants γ_y, δ_{xx}, and δ_{yy} were defined in the expansion of $\bar{u}$ in (5.8), and depend on the particle position.

2.4.4 The Outer Integral

For the outer integral we will consider alternate dimensionless variables, by using the rescaled distance $\mathbf{R} = \alpha\mathbf{r}$. This corresponds to using ℓ to non-dimensionalize lengths, rather than a. We call these variables the outer variables, and we will denote them with uppercase roman letters. A detailed comparison of the dimensionless variables is given in Appendix A.1.

In the outer region V_2, we must express our functions in terms of $\mathbf{R}$ and rearrange our functions by order of magnitude in α. These expansions are listed in full in Appendix A.4. In the outer region, the reciprocal theorem integral takes the following dimensional form:

$$F_{L_2} = \rho U_m^2 \ell^2 \int_{V_C} \hat{\mathbf{U}} \cdot \left(\bar{\mathbf{U}} \cdot \nabla \mathbf{U}^{(0)} + \mathbf{U}^{(0)} \cdot \nabla \bar{\mathbf{U}} + \mathbf{U}^{(0)} \cdot \nabla \mathbf{U}^{(0)} \right) dv, \qquad (2.29)$$

where we have expanded our domain of integration from $V_2 = \{\mathbf{R} \in V : R \geq \xi\}$ to the entire empty channel V_C. This expansion of the domain is justified since the contribution from the region that we add to the integral $\{\mathbf{R} : 0 \leq R \leq \alpha\xi\}$ is $O(\alpha^4\xi)$, and $\xi \ll 1/\alpha$. In fact this residue (which would show up in the $O(\alpha^3)$ inner integral) is exactly zero.

As we did for the inner integral, we can write the outer integral as an expansion in α.

$$F_{L_2} = \rho U_m^2 \ell^2 (k_4 \alpha^4 + k_5 \alpha^5 + \dots) . \qquad (2.30)$$

The velocity terms that contribute to k_4 are the following:

$$\mathbf{U}_1^{(0)} \sim \alpha^3 \frac{1}{R^2} \mathbf{f}_1^1 , \qquad \mathbf{U}_2^{(0)} \sim \alpha^3 \mathcal{SI}\left[\frac{1}{R^2} \mathbf{f}_1^1 \right] ,$$

$$\hat{\mathbf{U}}_1 \sim \alpha \frac{1}{R} \mathbf{g}_0^1 , \qquad \hat{\mathbf{U}}_2 \sim \alpha \mathcal{SI}\left[\frac{1}{R} \mathbf{g}_0^1 \right] , \qquad \bar{\mathbf{U}} \sim \gamma R + \delta R^2 + \dots \quad . \qquad (2.31)$$

Again, we define $\mathbf{V} = \mathcal{SI}[\mathbf{U}]$ as the image of the function $\mathbf{U}$, and we compute $\mathcal{SI}\left[\frac{1}{R^2}\mathbf{f}_1^1\right]$ and $\mathcal{SI}\left[\frac{1}{R}\mathbf{g}_0^1\right]$ numerically. Furthermore, we can approximate the term $\mathbf{f}_1^1$ by the stresslet terms, since the rotlet terms have coefficients that are order $O(\alpha^2)$ higher than the coefficients of the stresslet terms. The $O(a^4)$ contribution to the reciprocal theorem integral takes the following form:

$$k_4 = \int_{V_C} (\hat{\mathbf{U}}_1 + \hat{\mathbf{U}}_2) \cdot \left[\bar{\mathbf{U}} \cdot \nabla(\mathbf{U}_1^{(0)} + \mathbf{U}_2^{(0)}) + (\mathbf{U}_1^{(0)} + \mathbf{U}_2^{(0)}) \cdot \nabla \bar{\mathbf{U}} \right] dv. \qquad (2.32)$$

We run into a problem numerically evaluating the integral in (2.32) when considering only the first terms in the series expansions, $\mathbf{U}_1^{(0)}$ and $\hat{\mathbf{U}}_1$. The problem arises because $\mathbf{U}_1^{(0)}$ and $\hat{\mathbf{U}}_1$ have singularities of the form:

$$\mathbf{U}_1^{(0)} \approx -\frac{5\gamma_y}{2} \frac{(Y - Y_0)Z\mathbf{R}}{R^5}, \qquad \hat{\mathbf{U}}_1 \approx \frac{3}{4}\left(\mathbf{e}_Y + \frac{(Y - Y_0)\mathbf{R}}{R^2}\right)\frac{1}{R}, \tag{2.33}$$

which are respectively the stresslet and stokeslet components of the two velocity fields. When the singularities are integrated against the shear term of $\bar{\mathbf{U}}$, that is $\bar{\mathbf{U}}_\gamma \approx \gamma_y Y\, \mathbf{e_z}$, the result is an integral that is undefined near $R = 0$.

$$\int_{R<\epsilon} \hat{\mathbf{U}}_1 \cdot \left[\bar{\mathbf{U}}_\gamma \cdot \nabla\mathbf{U}_1^{(0)} + \mathbf{U}_1^{(0)} \cdot \nabla\bar{\mathbf{U}}_\gamma\right] \mathrm{d}v \tag{2.34}$$

However, converting to spherical coordinates, we find that the angular dependence forces the integral in (2.34) to be zero:

$$\int\limits_0^\pi \int\limits_0^{2\pi} \int\limits_0^\epsilon \left(\frac{15\gamma_y^2(1 + 2\cos 2\theta)\sin^4\theta \sin^3\phi}{4R}\right)\, \mathrm{d}R\mathrm{d}\phi\mathrm{d}\theta = 0. \tag{2.35}$$

This angular behavior is difficult to capture numerically, especially if the mesh is not symmetric. Instead, we propose a regularization of the outer integral, where we integrate the problematic terms analytically in a small region near $R = 0$. Now considering the full expansion of $\bar{u}$, we derive the following analytic form for the integral in the region near the origin:

$$\int_{R<\epsilon} \hat{\mathbf{U}}_1 \cdot \left[\bar{\mathbf{U}} \cdot \nabla\mathbf{U}_1^{(0)} + \mathbf{U}_1^{(0)} \cdot \nabla\bar{\mathbf{U}}\right] \mathrm{d}v = -\pi\gamma_y(\delta_{xx} + 3\delta_{yy})\epsilon \tag{2.36}$$

Recall that the constants γ_y, δ_{xx}, and δ_{yy} were defined in the expansion of $\bar{\mathbf{u}}$ in (5.8). Using this analytic expression, we split up the rest of the reciprocal theorem integral (2.32) into the following parts.

25

$$
\begin{aligned}
k_4 &= \int_{V_C} \hat{\mathbf{U}}_2 \cdot \left[\bar{\mathbf{U}} \cdot \nabla(\mathbf{U}_1^{(0)} + \mathbf{U}_2^{(0)}) + (\mathbf{U}_1^{(0)} + \mathbf{U}_2^{(0)}) \cdot \nabla \bar{\mathbf{U}} \right] \mathrm{dv} \\
&+ \int_{V_C} \hat{\mathbf{U}}_1 \cdot \left[\bar{\mathbf{U}} \cdot \nabla \mathbf{U}_2^{(0)} + \mathbf{U}_2^{(0)} \cdot \nabla \bar{\mathbf{U}} \right] \mathrm{dv} \\
&+ \int_{\{\mathbf{r} \in V_C : R \geq \epsilon\}} \hat{\mathbf{U}}_1 \cdot \left[\bar{\mathbf{U}} \cdot \nabla \mathbf{U}_1^{(0)} + \mathbf{U}_1^{(0)} \cdot \nabla \bar{\mathbf{U}} \right] \mathrm{dv} \\
&- \pi \gamma_y (\delta_{xx} + 3\delta_{yy}) \epsilon \; .
\end{aligned}
\tag{2.37}
$$

The first three lines in (2.37) are evaluated numerically using the FEM. Evaluating the integral in (2.37), we arrive at the scaling law:

$$
F_{L_2} = \frac{\rho U_m^2 k_4 a^4}{\ell^2} + O(a^5) \; ,
\tag{2.38}
$$

where $k_4 = O(1)$ is a constant that depends on the location of the particle in the channel, and is computed numerically.

Similarly, the $O(\alpha^5)$ correction to the outer integral comes from terms:

$$
\mathbf{U}_1^{(0)} \sim \alpha^3 \frac{1}{R^2} \mathbf{f}_1^1 \; , \qquad \mathbf{U}_2^{(0)} \sim \alpha^3 \mathcal{SI} \left[\frac{1}{R^2} \mathbf{f}_1^1 \right] ,
$$
$$
\hat{\mathbf{U}}_3 \sim \alpha^2 \frac{1}{R} \mathbf{g}_0^3 \; , \qquad \hat{\mathbf{U}}_4 \sim \alpha^2 \mathcal{SI} \left[\frac{1}{R} \mathbf{g}_0^3 \right], \quad \bar{\mathbf{U}} \sim \gamma R + \delta R^2 + \dots \; .
\tag{2.39}
$$

Again, we must regularize the outer integral, since $\hat{\mathbf{U}}_3$ also has a stokeslet singularity. We use the same regularization as before, replacing $\hat{\mathbf{U}}_1$ and $\hat{\mathbf{U}}_2$ with $\hat{\mathbf{U}}_3$ and $\hat{\mathbf{U}}_4$, respectively.

And, combining terms at $O(a^4)$ and $O(a^5)$, we obtain:

$$
F_{L_2} = \frac{\rho U_m^2 k_4 a^4}{\ell^2} + \frac{\rho U_m^2 k_5 a^5}{\ell^3} + O(a^6) \; ,
\tag{2.40}
$$

where $k_5 = O(1)$ is a constant that depends on the location of the particle in the channel. We have now calculated the V_2 contribution to the reciprocal theorem integral up to order $O(a^5)$.

2.4.5 Results

In the last section, we described our method of computing the correction to the scaling law made by [32]. Combining the inner and outer integrals, the result is a new approximation of the form:

$$F_L = \frac{\rho U_m^2 c_4 a^4}{\ell^2} + \frac{\rho U_m^2 c_5 a^5}{\ell^3} + O(a^6) \,, \tag{2.41}$$

where $c_4 = k_4$ from (2.37), and $c_5 = h_5 + k_5$ from (2.28) and (2.40). The prefactors c_4 and c_5 are $O(1)$ in α, and depend only on the location of the particle in the channel. The extended series agrees well with numerical data for particle sizes up to $\alpha = 0.2 - 0.3$ (Fig. 6). This calculation could in principle be extended by computing the contributions from higher order terms. Completing the series [31], i.e. approximating:

$$F_L \approx \frac{\rho U_m^2 c_4 a^4}{\ell^2 \left(1 - \frac{c_5 a}{c_4 \ell}\right)} \,, \tag{2.42}$$

produces a modest increase in the accuracy of the asymptotic approximation (Fig. 6).

By including two terms in our asymptotic expansion, we can describe how the particle equilibrium position depends on its size – a key prediction for rationally designing devices that use inertial lift forces to fractionate particles, or to transfer them between fluid streams [23, 38, 50, 13, 69] (figure 2.8). We compare our asymptotic calculation predictions directly with experiments of [23], finding good agreement in focusing positions up to $a = 0.3$ (Fig. 2.8b.).

2.5 3D asymptotic expansion

Previous asymptotic studies have considered inertial migration in 2D flows [32, 63, 33, 2]. At sufficiently small values of a there is qualitative agreement between the 2D theories and our theory, but only when the particle is located on a symmetry plane e.g. $x_0 = 0$ or $y_0 = 0$. However, real inertial microfluidic devices focus in x and y- directions, taking initially uniformly dispersed particles to four focusing positions. Our asymptotic approach

(a) (b)
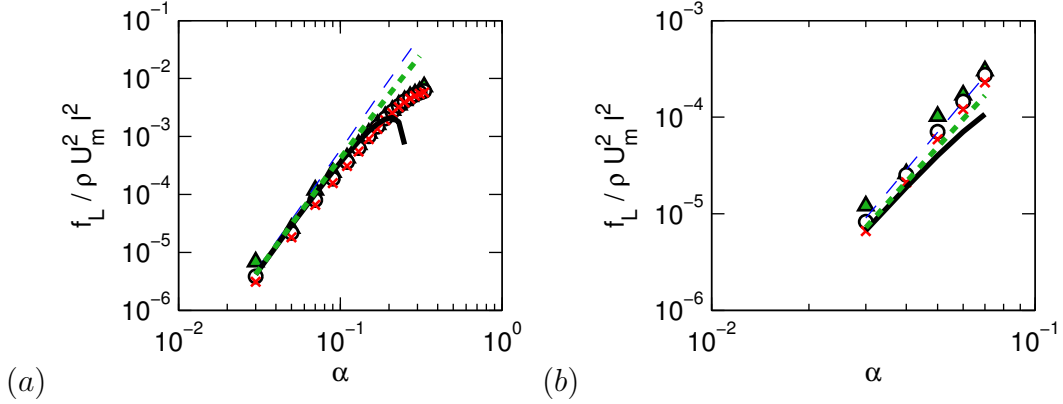
Figure 2.6: We compute lift force F_L numerically using the Navier-Stokes equations in (2.4) and plot as a function of particle radius a for channel Reynolds numbers $Re = 10$ (triangles), $Re = 50$ (circles), and $Re = 80$ (x's). The blue dashed line represents a scaling law of particle radius to the fourth power $F_L = \rho U_m^2 c_4 \alpha^2 a^2$, the solid black line represents the sum of the fourth and fifth power terms in (2.41), and the green dotted line represents the completion of series in (2.42), with (a) particle displacement $y_0 = 0.15/\alpha$, and (b) particle displacement $y_0 = 0.4/\alpha$.

allows us to compute the focusing forces for particles placed at arbitrary positions in the channel.

The calculation is very similar to the one outlined in §2.4; we only need to add similar terms driven by the shear in the x-direction, and allow for a reciprocal velocity $\hat{\boldsymbol{u}}$ associated with moving the particle in this direction. The full Lamb's solution for $\mathbf{u}_1^{(0)}$ has additional terms from the shear in the x-direction (i.e. the terms with coefficients γ_x), shown in Appendix A.3. The only additional components of $\mathbf{u}_1^{(0)}$ that contribute to the 3D calculation are the stresslet and source quadrupole.

The inner integral in 3D evaluates to:

$$F_{L_1}^{(3D)} = \frac{\rho U_m^2 h_5^{(3D)} a^5}{\ell^3} + O(a^6) \; , \tag{2.43}$$

28
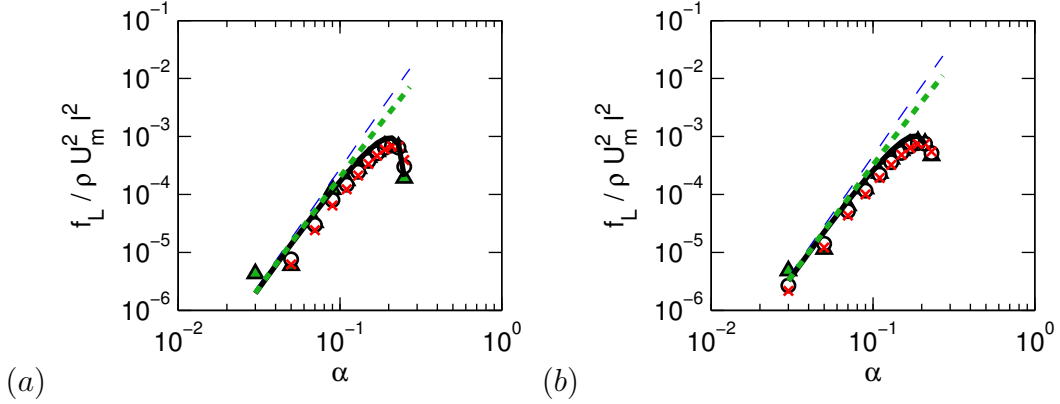
Figure 2.7: We compute lift force F_L numerically from (2.4) as function of particle radius for channel Reynolds numbers $Re = 10$ (triangles), $Re = 50$ (circles), and $Re = 80$ (x's). The blue dashed line represents a scaling law of particle radius to the fourth power $F_L = \rho U_m^2 c_4 \alpha^2 a^2$, the solid black line represents the fifth power correction term in (2.46), and the green dotted line represents the completion of series in (2.42), with particle displacement $x_0 = 0.2/\alpha$ and $y_0 = 0.15/\alpha$ for (a) lift force in the x-direction and (b) in the y-direction.

where

$$
\begin{aligned}
h_5^{(3D)} &= \frac{4381\pi\gamma_x\gamma_y}{554400} - \frac{26171\pi\gamma_y^2}{277200} + \frac{527\pi\psi_y\gamma_x\gamma_y}{116424} - \frac{53\pi\gamma_y\delta_{xx}}{1728} \\
&+ \frac{19\pi\gamma_x\delta_{yy}}{3150} - \frac{283\pi\gamma_y\delta_{yy}}{3150}.
\end{aligned}
\tag{2.44}
$$

We define ψ_y to be the value of y-component of image of the stokeslet evaluated at the location of the particle:

$$
\psi_y = \left[\mathcal{SI}\left[\frac{1}{r}\mathbf{g}_0^1\right] \cdot \mathbf{e_y} \right]\Bigg|_{(x,y,z)=(x_0,y_0,0)},
\tag{2.45}
$$

where $\mathbf{g}_0^1$ is the stokeslet and the leading term of $\hat{\mathbf{u}}_1$ defined in (A.8) in Appendix A.3. The outer integral remains the same, however, $\mathbf{u}_1^{(0)}$ and $\mathbf{u}_3^{(0)}$ each now include a stresslet contribution associated with shear in the x-direction. Computing this integral gives a scaling law of the form:

$$
F_L^{(3D)} = \frac{\rho U_m^2 c_4^{(3D)} a^4}{\ell^2} + \frac{\rho U_m^2 c_5^{(3D)} a^5}{\ell^3} + O(a^6) .
\tag{2.46}
$$

29
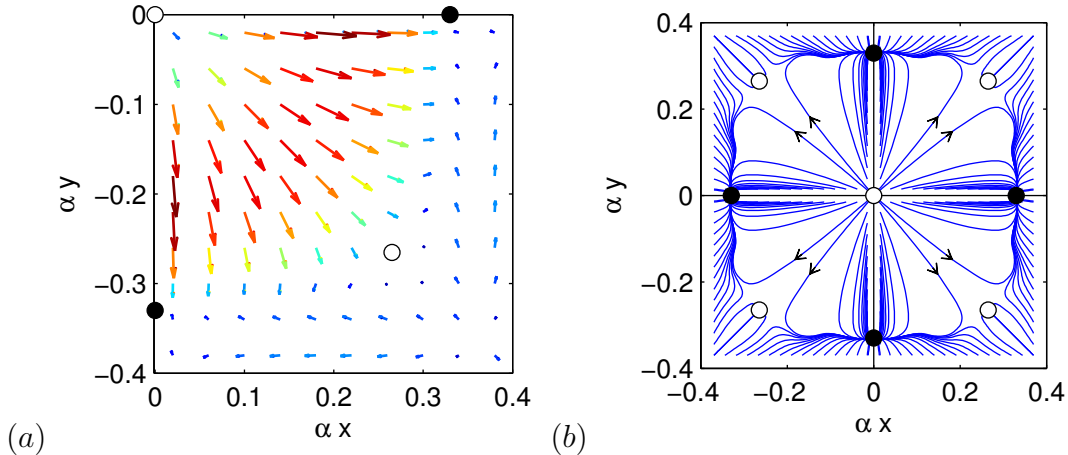
Figure 2.8: (a) Lift force calculated using (2.46) for locations in the lower right quadrant of the channel for a particle of radius $\alpha = 0.11$, and $Re = 80$. The solid black circles mark stable equilibrium points, while the open white circles mark unstable equilibrium points. (b) Trajectories of particles calculated using (3.4) for particle size $\alpha = 0.11$ and $Re = 80$. The solid black circles mark stable equilibrium points, while the open white circles mark unstable equilibrium points.

It remains true that for particles located arbitrarily in the square channel, the lift force scales like a^4 in the asymptotic limit $\alpha \to 0$. Additionally, our $O(a^5)$ correction to the scaling law remains accurate for moderately large α, shown in figure 2.7a and 2.7b for the forces in the x and y-direction, respectively. We provide the calculated values of the three dimensional lift force in a square channel in a Matlab code in the online supplementary materials. In particular we find that lift forces vanish only at 8 symmetrically placed points around the channel, with 4 points being stable and 4 unstable, in good agreement with experimental observations (Fig. 2.8a).

We can compute particle streamlines using the lift force prediction, and confirm that there are four stable focusing positions in the channel (figure 2.8b). Particles are advected using a Forward Euler time stepping scheme. We find the particle velocity by equating the $O(a^5)$ lift force (2.46) with the $O(a)$ drag force [30]. That is, v_L, the y-component of velocity

(a) (b)
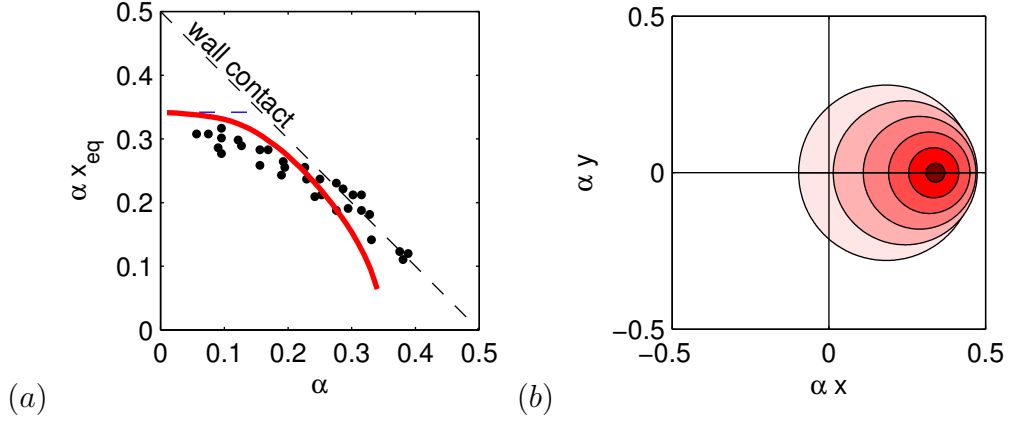
Figure 2.9: (a) Our theory predicts inertial focusing position as a function of particle size. The markers are data collected by [23], the dashed blue line is the theory predicted by the first term of $O(a^4)$ in (2.41), and the solid red line is the theory predicted by (2.41). (b) In this schematic diagram we plot the outlines of particles at their predicted focusing position along the positive x-axis. The particle sizes range between $\alpha = 0.03$ and $\alpha = 0.29$.

v, satisfies the equation:

$$6\pi\mu a(v_L + \psi_y) = \left[\frac{\rho U_m^2 c_4^{(3D)} a^4}{\ell^2} + \frac{\rho U_m^2 c_5^{(3D)} a^5}{\ell^3}\right]\Bigg|_{(x_0, y_0, 0)}, \tag{2.47}$$

where ψ_y is the image velocity of the stokeslet defined in (2.45). The velocity u_L, the x-component of velocity u, is computed in the same way by substituting ψ_x from the x-stokeslet for ψ_y.

In addition, the distance of the focusing positions from the channel center-line can be predicted by solving the implicit equation $F_L^{(3D)} = 0$. Recall that the lift force coefficients depend on the location of the particle, i.e. $c_4^{(3D)} = c_4^{(3D)}(x_0, y_0)$ and $c_5^{(3D)} = c_5^{(3D)}(x_0, y_0)$. Since the lift force formula has both $O(a^4)$ and $O(a^5)$ terms, the focusing position will have a functional dependence on the particle size a. This prediction of the focusing position compares well with experimental data by [23], especially for particle sizes up to $\alpha \leq 0.3$ (Fig. 2.9b).

31

2.6 Discussion

Our findings resolve confusion about the size dependence of inertial lift forces experienced by particles traveling through microchannels. Many asymptotic and numerical studies have been employed to determine how the lateral force scales with particle radius, and have found power laws with exponents two, three, four, and five. By numerically dissecting the equations of fluid flow around the particle, we find that viscous stresses dominate over inertial stresses even at moderate channel Reynolds numbers. We rationalize this finding by showing that this ordering of fluxes is inherited from the stresslet flow field approximation to the far field of a particle, provided that the contribution from channel walls is included. We make use of this fact to develop a perturbation series expansion for the lift force, extending the theory of Ho & Leal both to three dimensions and to include $O(a^5)$ sized terms. We find that the scaling is a power law with exponent four for asymptotically small particle radius, but that additional terms must be included to predict lift forces for the range of particle sizes and flow speeds accessed in real inertial microfluidic devices. By including these additional terms, we are also able to predict asymptotically how focusing position depends on particle size.

Somewhat surprisingly, the regular perturbation expansion accurately predicts the particle lift force even at channel Reynolds numbers and particle sizes where the parameters in our expansion are not small (e.g. up to $Re_p \approx 10$). This is consistent with our determination that inertial stresses fluxes scale simply with U^2 even outside of the regime of velocities and channel sizes at which viscous stresses are numerically larger than momentum fluxes. Thus although assuming a viscous stress-pressure dominant balance is not justified based on simple comparison of the order of magnitude of terms, the perturbation expansion continues to give good results.

We hope that the results in this paper will provide a first step toward predictive theory for the design of inertial microfluidic devices. The biggest unmet challenge here is to determine whether unsteady effects scale like momentum fluxes for determining dominant balances. If the unsteady scaling can be established, then it will be possible to model time varying

problems, including the migration of particles in non-rectilinear geometries, such as the microcentrifuge, or the interactions of particles, such as the recently discovered phenomena of self-organization by inertially focused particles into stably ordered chains [47, 37]. We have shown that the viscous-pressure stress dominant balance leads to a particularly simple far-field form to the flow disturbance, potentially allowing simplified modeling of particle interactions. Additionally we provide a Matlab code with the calculated values of the lift force in the online supplementary materials.

CHAPTER 3

Direct Measurement of Particle Inertial Migration in Rectangular Microchannels

3.1 Introduction

Inertial migration; the systematic movement of particles across streamlines due to finite Reynolds number forces, is exploited in systems to separate, focus and filter particles and cells [69]. Though there are many theories for the magnitudes of inertial focusing forces, direct experimental measurement of these forces remains an unmet challenge. Indeed existing theory [62, 32, 63, 36], numerical simulations [23, 57, 49], and indirect experimental measurements [78] have produced contradictory scalings for the dependence of forces on particle size and velocity. In this paper, we directly measure inertial migration velocities by tracking the motion of particles in a rectangular channel over Reynolds numbers ranging from 30 to 180, and find that their measured migration velocities agree well with existing asymptotic theory [36].

Inertial migration of neutrally buoyant particles was first reported in flows through circular pipes [64]. In a pipe with radius R, particles are inertially focused into a ring with radius approximately $0.6R$. Furthermore, particles with different sizes are focused at different rates and to rings with slightly different radii [39, 41, 73, 74, 8]. However, microfluidic channels are more readily built with a rectangular geometry, in which particles are inertially focused to either two or four stable equilibrium streamlines [23]. Focusing occurs in two phases, with apparently well-separated natural time scales: (Fast phase) first particles quickly focus to a
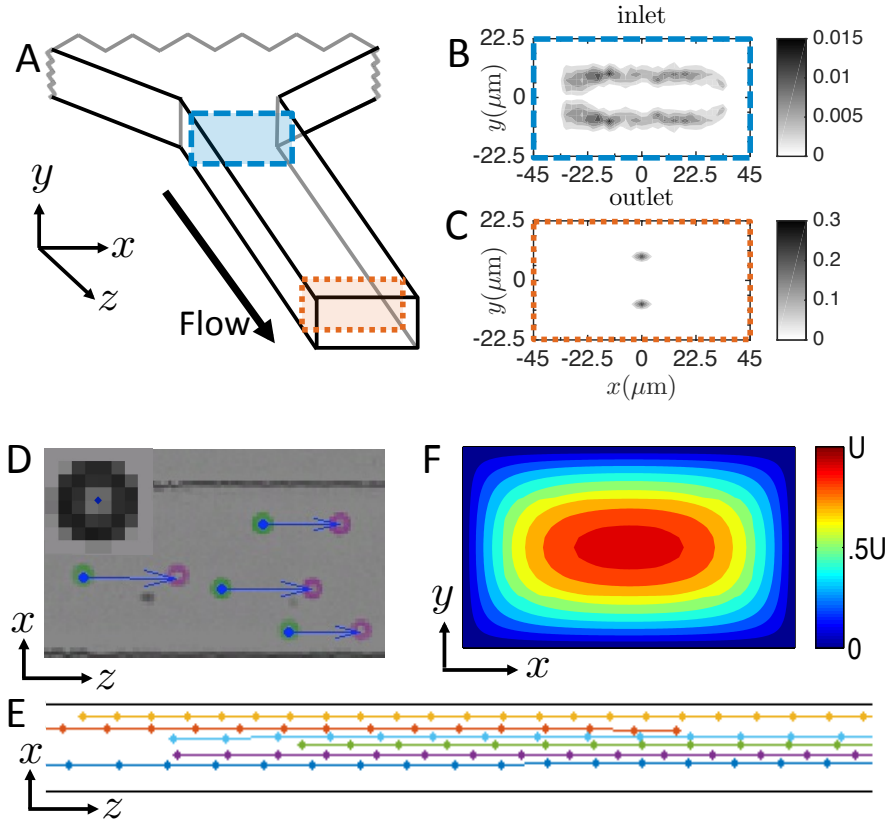
Figure 3.1: Reconstruction of particle focusing velocities and three dimensional positions in a rectangular channel. (A) Schematic of the inlet of the channel. (B) Reconstructed probability density function (PDF) of particle distributions across the channel cross-section for $10\,\mu$m particles at $Re = 30$ shows that within the first 1 mm of the channel particles are initially focused to two narrow bands of streamlines (density shown in grayscale). (C) After 1.5 cm of inertial focusing, the same particles are fully focused to two streamlines on the channel mid-line. (D) A hybrid PIV-particle tracking scheme is used to track the particles, green circles show particles in present frame, magenta circles show the particles in the next frame. (inset) Template matching (blue circle) allows particle center to be located with sub-pixel accuracy. (E) Representative trajectories of six particles tracked over $700\,\mu$s. (F) Numerically computed downstream particle velocity as a function of x and y positions across the channel cross-section: using this plot and the particle velocity in the z-direction, we can compute its $y-$position.

two-dimensional manifold of streamlines and then (Slow phase) particles travel within the manifold to one of the focusing streamlines. Two stage focusing has been experimentally measured [9], and is consistent with numerical simulations of the spatial pattern of lift forces across the channel cross-section [28, 57, 49, 36].

Focusing in rectangular channels has been studied asymptotically, generating disagreement over the scaling of the inertial lift force. Recent asymptotic studies [32, 63, 2] predicted that the inertial lift force F_L is proportional to the fourth power of the particle radius a, i.e. $F_L \sim a^4$. This scaling hinges on the assumption that the particle radius is asymptotically smaller than the channel size, $a \ll H$. Di Carlo et al showed that the a^4 scaling did not agree with numerical simulations [23]. Rather, the numerical data suggested $F_L \sim a^3$. Hood et al [36] extended the asymptotic analysis of Ho & Leal [32]. The resulting scaling law $F_L \sim c_4 a^4 + c_5 a^5$, reconciles the asymptotic scaling $F_L \sim a^4$ in the limit $a \ll H$ with the numerical data of Di Carlo et al [23] up to experimentally used particle sizes, in which $a \sim H$. By contrast, Saffman's asymptotic study of inertial lift force assumes that the particle experiences an external force in the direction of flow in addition to the inertial lift force [62]. Using an indirect experimental measurement of inertial focusing, Zhou and Papautsky [78] report that $F_L \sim a^2$, in agreement with Saffman. But they do not explain why Saffman's result applies to particles that are traveling freely with the flow of fluid.

Here we present the first reconciliation of predictive theory and direct experimental measurement of inertial migration velocities. While holographic techniques have been used to measure 3D particle distributions and velocities in microfluidic capillaries [67, 42, 9, 10], but to the best of our knowledge holographic techniques have not been used to measure inertial migration velocities. In this paper we propose an alternative to holographic techniques for measuring the 3D positions and velocities in PDMS microchannels. Our method allows accurate measurement of particle migration velocities in two dimensions, and via a velocity-based reconstruction method, of their position in the third dimension. This method provides position readouts for thousands of particles and allows particle positions and particle trajectories to be measured. Thus, our method provides the first direct measurement of inertial

migration velocities. In addition to verifying the existence of a slow-focusing manifold, our position measurements show that significant inertial focusing occurs while particles are funneled into the channel, and that once this contribution is accounted for, inertial migration velocities agree fully with an asymptotic theory [36].

3.2   Experimental methods

Inertial focusing was measured in a 1.5 cm long PDMS microchannel fabricated using Sylgard 184 PDMS kit (Dow Corning Corp.) bonded to a glass slide as shown in Duffy et al [25]. The microchannel mold was fabricated using KMPR 1025 (MicroChem). The channel cross-section dimensions were 90μm $\times$ 45μm ($W \times H$), respectively, with the shortest dimension identified as the depth (y) dimension (Fig. 1A) and the longer dimension as the width or lateral dimension (x). The schematics of the channel are displayed in Fig. 3.1A. Particles enter the channel through an contracting inlet region whose depth is constant (45μm) and tapers in width from 1.5 mm to 90 μm over a 2.4 mm downstream length.

The particles were dispersed at 0.004 volume fraction in a suspending fluid composed of deionized water and 0.002 (wt/vol) triton X-100. This suspension was pumped into the channel at controlled flow rate using a syringe pump (Harvard Apparatus, Holliston MA). The solutions were infused using PEEK tubing (Idex: 1/32" OD*0.02" ID*5ft). The polystyrene spherical particles were chosen to be near-neutrally buoyant with a particle density of 1.05 g/cm^3. The particle density does not match the density of the suspending fluid (density 1.00g/cm^3), never the less the effects of sedimentation can be ignored in this experiment. The sedimentation velocity can be determined by balancing buoyancy force with the drag force for a sphere. For this experiment, the sedimentation velocity is at most 10μm/s, meaning that the particles sediment a distance of less than 0.3 μm over the entire length of the channel. Therefore, sedimentation effects are negligible compared to the downstream velocity ($\sim$0.6m/s) and inertial migration velocity ($\sim$3mm/s).

The channel Reynolds number is defined by $Re = UH/\nu$, where $\nu = 1 \times 10^{-6}$ m^2/s is

the kinematic viscosity of deionized water at room temperature, $H = 45\mu$m is the short dimension of the channel, and U is the average fluid velocity in the channel. The ratio of particle size to channel size is defined by $\alpha = a/H$, where a is the particle radius, and the particle Reynolds number is given by $Re_p = \alpha^2 Re = Ua^2/\nu H$. Four particle radii were separately used, $a = 2.4, 5, 6,$ and 9.5μm, along with four different total flow rates $Q = 160, 320, 640,$ and 960μL/min, corresponding to a range of channel Reynolds numbers $Re = 30 - 180$ and particle Reynolds numbers $Re_p = 0.08 - 3.2$. The maximum Reynolds number of 180 was chosen to avoid delamination of the PDMS from the glass slide, while the minimum Reynolds number of 30 was chosen so that the inertial particle migration rate would be observable in the channel of length of 1.5cm.

Particle velocities were tracked by high speed imaging (14000 frames per second and 2μs exposure time, using a Phantom V710 camera) over the first and last 1 mm of the channel. The microchannel was viewed from above using a microscope (Nikon Ti-U) with 4x objective with effective pixel size of 3μm. The depth of field is listed to be 50 μm by the manufacturer, however blurry particles are still observable even for a range of upwards of 200 μm, so that the particles can be observed over the entire channel depth. For all diameters and velocities, particles were eventually focused to two streamlines on the mid-plane $x = 0$ (Fig. 3.1B-C).

3.3 Determining the particle migration velocity

High speed videography provided only x- and z- (lateral and streamwise) coordinates for each particle, and provided no direct measurement of the particle depth (y-coordinate). We measured the x- and z- velocities by hybridizing particle image velocimetry (PIV) and particle tracking, similar to an algorithm previously developed for tracking fluorescent organelles [60]. First, we use the PIV code MatPIV [72] to develop a vector field representing the displacements of all particles from one frame to the next. Second, template matching is used to align a template consisting of a single 8×8 pixel image of a particle with both the first frame and the next. The template matching process gives a single correlation value for every

pixel in the image, representing how closely the template matches the real image centered at that pixel. Then we use cubic polynomials to interpolate the correlation data and find each particle location with sub-pixel precision. After locating particles in both frames, the PIV velocity field is used to predict the particles' locations in the subsequent frame. We identify the detected particle in the next frame that is closest to this predicted location. The particle tracking adjustment allows us to correct PIV velocity fields to obtain sub-pixel accurate particle displacements (Fig. 3.1D).

Multiple frames are needed to measure the migration velocity since the lateral displacements of particles over a single frame are typically sub-pixel. Indeed, inertial migration velocities are typically two orders of magnitude smaller than particle downstream velocities (3 mm/s in a typical experiment compared to 0.6 m/s downstream velocity). To accurately measure the migration velocities, we track single particles over at least 10 consecutive frames, and average their total lateral displacement over all of these frames (Fig. 3.1E).

We reconstruct the $y-$positions of the particles using a numerical prediction of the downstream velocity. We used a finite-element model built in Comsol Multiphysics (Comsol, Los Angeles) to compute the downstream velocities for force-free and torque-free finite particles whose size matched the experiments [36] located anywhere within the channel (Fig. 3.1F). The Stokes timescale $\tau_s = 2\rho a^2/9\mu$, gives a measure of the time needed for a particle at any point in the channel cross-section to accelerate until it is both force and torque free. For the particles in our study $\tau_s = 5 - 80\,\mu$s, is much less than a typical tracking time of $700\,\mu$s, so particles are effectively force-free and torque-free throughout their migration. Downstream velocities vary across the depth of the channel, with no slip boundary conditions on the upper and lower walls of the channel and fastest velocities attained on the mid-plane of the channel. For each x-position there is a two-to-one mapping of downstream velocity to particle depth, allowing particles to be assigned one of two $y-$coordinates that are symmetric about the depth mid-plane $y = 0$ (Fig. 3.1F).

We measured the two dimensional probability density function (PDF) for the $x-$ and $y-$ coordinates of particles at the entrance to the microchannel and after 1.5cm of inertial

focusing (Fig. 3.1B-C). Particles within 1mm of the microchannel entrance are not uniformly dispersed in channel depth but instead are focused to a thin band of $y-$ coordinates (Fig. 3.1B). We call this phenomenon pre-focusing because it is a consequence of inertial migration that occurs in the contracted inlet region before the particle enters the channel. Along the channel, particles move laterally within this band until they are also focused close to the channel center-line, with typically 71% of particles focused to within $4\,\mu$m of the focusing streamline after traveling 1.5cm through the microchannel (Fig. 3.1C).

The thin band on which particles are concentrated in the first 1 mm of the channel coincides with an asymptotic calculation for the slow manifold, described in more detail below (Fig. 3.3A-D). Since the particles are already focused to their slow manifold, the observed lateral migration within the microchannel represents only the second phase of particle focusing, i.e. the migration of particles along the slow manifold to their eventual focusing streamline (Fig. 3.4).

Validation of the reconstruction algorithm

In order to validate the measurement of particle heights via the velocimetric method, we ran the following experiment to independently measure the particle heights. Since particles outside the focal plane appear blurry, we exploit this blurriness to distinguish particle heights. We will call this method the laplacian algorithm, because it uses the discrete Laplacian to measure the sharpness of the edges of the particle.

The experiment is designed as follows: we vary the focal plane height of the microscope and at each height measure the number of particles that appear to be in-focus. In this experiment there are two potential sources of blur: out-of-focus blur and motion blur. In order to reduce the motion blur, we ran this experiment at $Re = 1$ and flow rate $Q = 5\mu$L/min. We used 12μm diameter particles and kept the exposure time constant (2μs) and reduced the frame rate to 500fps. During the experiment the focal plane is raised in 6μm increments. We measured these increments using a Nikon inverted microscope with
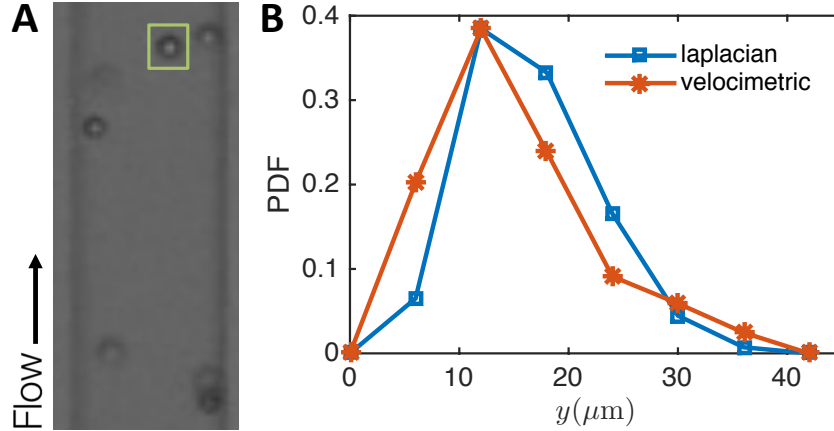
Figure 3.2: Validation measurement for $Re = 1$ and $a = 6\mu$m. (A) Raw image of particles with focal plane height of 6μm above the bottom of the channel. The laplacian algorithm measures only one particle to be in focus (inside green box). (B) Experimental calibration of the particle height measurement. The PDF of particle height compares well between the velocimetric algorithm (blue square) and the laplacian algorithm (orange asterisk).

programmable focus, which allows the focal plane to be precisely controlled.

The laplacian algorithm works as follows. We average the discrete Laplacian on a 7×7 pixel sub-image around the particle to get a single laplacian measurement for each particle. A larger value indicates the particle is more in focus, and we can reference each value against a calibration measurement to measure the relative height of the particle to the focal plane. The calibration measurement comes from running the laplacian algorithm on stationary particles resting on the bottom of the channel at various focal plane heights.

At each focal plane height we count the number of particles that are measured to be within 3μm of the focal plane via both the laplacian and velocimetric algorithms. Recall that the reconstruction algorithm cannot distinguish between particles in the top half of the channel and the bottom half, so we use the laplacian algorithm to make that distinction.

A comparison of the PDF of particles via the velocimetric algorithm and particles via the laplacian algorithm shows good agreement (Figure 3.2). We observe that the particles are much more likely to be in the bottom half of the channel. This is to be expected, since at

$Re = 1$ sedimentation is a significant effect, indeed we predict that particles should sediment 9μm over the length of the channel.

The two algorithms produce consistent results in experiments where both algorithms can be used. The velocimetric algorithm has two major advantages over the laplacian algorithm. First, the velocimetric algorithm is much more precise: we can measure heights to a precision of less than a micron, whereas the laplacian algorithm depends on the precision of the focal plane height (in this case, 3μm). Second, the velocimetric algorithm can be used at much larger Reynolds numbers than the laplacian algorithm since motion blur does not interfere with the height measurements.

3.4   Theory of inertial migration

We adapt the asymptotic theory developed by Hood et al [36] for square channels to predict the inertial forces in rectangular channels. Since numerical experiments show that viscous stresses dominate momentum flux terms over the entire fluid filled domain, V, we can perform a regular perturbation expansion in the particle Reynolds number Re_p, treating the viscous and pressure stresses as dominant terms, and the inertial stress as a perturbative correction.

We use the Lorentz reciprocal theorem [45] to represent the inertial lift force $\mathbf{F}_L$ as a volume integral that involves the following three solutions of Stokes equations ($Re_p = 0$): (1) $\bar{\mathbf{u}}$, the undisturbed flow through the channel, (2) $\mathbf{u}$, the solution for a force-free and torque-free sphere moving through the microchannel, and (3) a test velocity $\hat{\mathbf{u}}$ for the slow ($Re_p = 0$) movement of a particle in the lateral direction in a quiescent fluid. The total force on a particle that is constrained from migrating across streamlines can be written as an integral:

$$\mathbf{F}_L = Re_p \int_V \hat{\mathbf{u}} \cdot (\bar{\mathbf{u}} \cdot \nabla \mathbf{u} + \mathbf{u} \cdot \nabla \bar{\mathbf{u}} + \mathbf{u} \cdot \nabla \mathbf{u}) \, \mathrm{dv}. \tag{3.1}$$

To expose the role played by particle size in determining the lift force,we expanded $\mathbf{u}$ and $\hat{\mathbf{u}}$ as a two-term series in $\frac{a}{H}$, the ratio of the particle radius to the channel depth. The lift force $\mathbf{F}_L$ at the point $\mathbf{x}_0$ in the channel can be expressed as a two term asymptotic expansion with

42

coefficients $\mathbf{c}_4(\mathbf{x}_0)$ and $\mathbf{c}_5(\mathbf{x}_0)$. Specifically,

$$\mathbf{F}_L(\mathbf{x}_0) \sim \frac{\rho U^2 a^4}{H^2} \left[\mathbf{c}_4(\mathbf{x}_0) + \frac{a}{H} \mathbf{c}_5(\mathbf{x}_0) \right], \tag{3.2}$$

where ρ is the fluid density, H is the channel depth, and U is the average velocity of the undisturbed flow. The coefficients $\mathbf{c}_4(\mathbf{x}_0)$ and $\mathbf{c}_5(\mathbf{x}_0)$ are dimensionless constants including both analytical and numerically computed components, and that depend on the location of the particle $\mathbf{x}_0$ and the aspect ratio of the rectangular cross-section. A text file giving the values of $\mathbf{c}_4(\mathbf{x}_0)$ and $\mathbf{c}_5(\mathbf{x}_0)$ for a grid of particle locations is included in the supplemental materials [34].

The method above, which adapts the results from Hood et al [36] for a channel with aspect ratio two, gives only the focusing force on a particle that is not free to migrate across streamlines. The particles in our experiments are free to migrate under inertial focusing forces. We find the migration velocity $\mathbf{u}_m = (u_m, v_m)$ of a force-free particle by equating the lift force (5.10) with the drag force computed for a particle translating with a general velocity $\mathbf{u}_m$ [30]. This drag force can be evaluated by the method of reflections, to the same order of accuracy as equation (5.10):

$$6\pi\mu a[\mathbf{u}_m(\mathbf{x}_0) + \mathbf{u}_{im}(\mathbf{x}_0)] = \mathbf{F}_L(\mathbf{x}_0), \tag{3.3}$$

where $\mathbf{u}_{im}$ is the leading order backflow created at $\mathbf{x}_0$ due to the walls of the microchannel. Furthermore, $\mathbf{u}_{im}(\mathbf{x}_0)$ is the first order correction calculated by the method of reflections for a small sphere migrating across streamlines and therefore is linearly related to the lift force $\mathbf{F}_L(\mathbf{x}_0)$, namely there exists a matrix $\mathbf{S}(\mathbf{x}_0)$ such that $\mathbf{u}_{im}(\mathbf{x}_0) \simeq \mathbf{S}(\mathbf{x}_0) \cdot \mathbf{F}_L(\mathbf{x}_0)$. The terms of $\mathbf{S}(\mathbf{x}_0)$ are determined by computing the reflection $\hat{\mathbf{u}}_2$ of the test velocity $\hat{\mathbf{u}}$ and evaluating at the center of the particle $\mathbf{x}_0$. More specifically, denote the method-of-reflections correction for a point force located at $\mathbf{x}_0$ and and pointing in the direction $\mathbf{e}_i$ by $\hat{\mathbf{u}}_{2,i}(\mathbf{x}_0)$. In this case $\mathbf{S}(\mathbf{x}_0) = S_{ij}(\mathbf{x}_0)$ is defined as:

$$S_{ij}(\mathbf{x}_0) = (\hat{\mathbf{u}}_{2,i}(\mathbf{x}_0) \cdot \mathbf{e}_j). \tag{3.4}$$

Rearranging the terms above for the migration velocity gives:

$$\mathbf{u}_m(\mathbf{x}_0) = \left[\mathbf{I} + \frac{a}{H} \mathbf{S}(\mathbf{x}_0) \right] \frac{\mathbf{F}_L(\mathbf{x}_0)}{6\pi\mu a}. \tag{3.5}$$

43
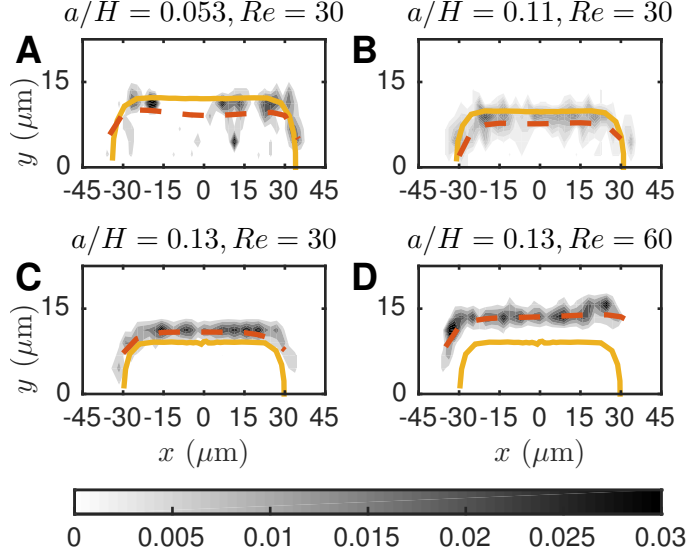
Figure 3.3: PDF of particle location in the upper half of the channel, with the gray scale indicating density. The predicted manifold (solid yellow line) is a good approximation of the measured manifold (dashed orange line). The particle size and Reynolds number in each figure are: (A) $a/H = 0.053$ $Re = 30$; (B) $a/H = 0.11$ $Re = 30$; (C) $a/H = 0.13$ $Re = 30$; and (D) $a/H = 0.13$ $Re = 60$.

The pre-factor here represents the tensorial mobility of the particle.

We are interested in how particles travel due to this migration velocity, which can be computed at any point $\mathbf{x}_0$ in the channel. Let $\mathbf{X}(t) = (X(t), Y(t))$ be the location of a given particle in the channel cross-section as a function of time t. For a particle migrating due to inertial lift forces:

$$\frac{d\mathbf{X}}{dt} = \mathbf{u}_m, \qquad \mathbf{X}(0) = (x_0, y_0). \tag{3.6}$$

The slow-focusing manifold is evaluated numerically by advecting particles according to (5.3) and finding the curve Λ which is invariant under (5.3). Note that Λ depends on the relative particle size $\frac{a}{H}$. At any point $\mathbf{x}_0$ in the channel, the migration velocity satisfies

$$\mathbf{u}_m(\mathbf{x}_0) \sim \frac{\rho U^2 a^3}{6\pi \mu H^2} \left[\mathbf{I} + \frac{a}{H} \mathbf{S}(\mathbf{x}_0) \right] \cdot \left[\mathbf{c}_4(\mathbf{x}_0) + \frac{a}{H} \mathbf{c}_5(\mathbf{x}_0) \right]. \tag{3.7}$$

where the coefficients $\mathbf{c}_4(\mathbf{x}_0)$ and $\mathbf{c}_5(\mathbf{x}_0)$ are the same as those calculated in (5.10).

The limiting assumptions in the development of equation (5.4) are twofold: (i) in order to make our regular perturbation expansion we assume $Re_p \ll 1$ and (ii) in order to represent the particle by a singularity we assume that the particle is much smaller than h the distance from the particle to the wall, $a \ll h \sim \frac{1}{6}H$. However, in practice conditions (i) and (ii) can be relaxed to a larger set of values for Re_p and α. Hood et al[36] show that, because the presence of the walls diminishes the size of the inertial term in the NSE, empirically this model is accurate up to $Re_p \leq 7$. Furthermore, Hood et al[36] empirically that the particle size limitation can be relaxed to $\alpha \leq 0.2$. In our experiments we have $Re_p \leq 3.2$ and $\alpha \leq 0.21$, so equation (5.4) should be a good approximation of the migration velocity.

The prediction of the focusing manifold Λ compares well to the measured manifold in experiments (Fig. 3.3A-D). The measured manifold is found by fitting a quadratic polynomial to the measured (x, y) locations of all the particles. Even though our theory assumes that $Re_p \ll 1$, the predicted manifold Λ is a fair approximation even when $Re_p = 1.01$ (Fig. 3.3D). Additionally, deformation of the PDMS channel has been reported at higher Reynolds numbers [70], which is not taken into account in our theory.

Lateral migration velocities along the manifold quantitatively agree with the asymptotic theory in equation (5.4). We filtered the measured velocities to select particles that were within a distance 2.25μm of the slow manifold. We then binned these particles into $3\,\mu$m $x-$intervals, and averaged migration velocities for particles within the same bin. Experimental measurements of migration velocity along the slow manifold agree almost exactly with the asymptotic prediction of the migration velocity along the theoretical manifold (Fig. 3.4A-D) including different particle sizes and flow speeds.

There are no free parameters in the prediction of the migration velocity in equation (5.4). The asymptotic result supports that $\mathbf{u}_m \propto U^2$, just as was found in previous numerical simulations [23]. The asymptotic theory also shows that migration velocity has no clear power law dependence on particle size. This asymptotic theory is most accurate for small particle sizes and moderate Reynolds numbers; in practice requiring that $\frac{a}{H} < 0.2$, and that channel Reynolds number $Re \lesssim 80$.
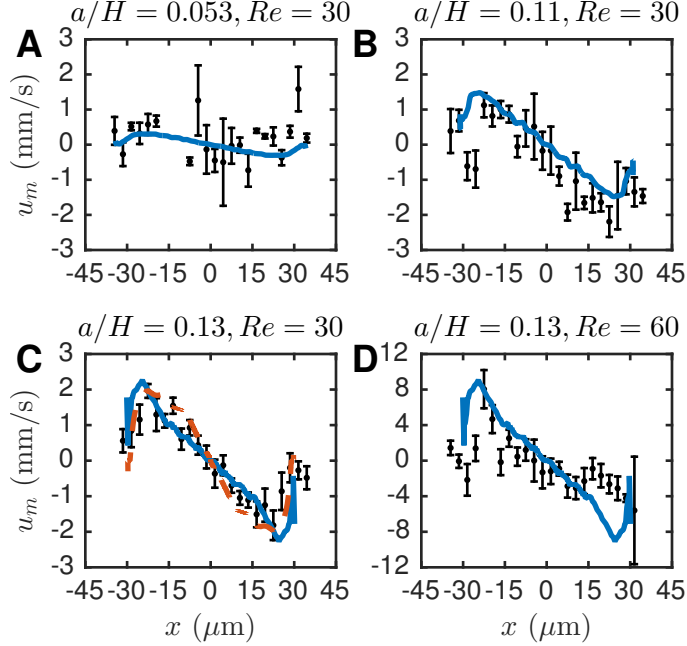
Figure 3.4: The measured migration velocity along the measured manifold (black markers) agrees quantitatively with the asymptotic theory (blue line) in equation (5.4) and numerical solution of the NSE (orange dashed line). The particle size and Reynolds number in each figure are: (A) $a/H = 0.053$ $Re = 30$; (B) $a/H = 0.11$ $Re = 30$; (C) $a/H = 0.13$ $Re = 30$; and (D) $a/H = 0.13$ $Re = 60$.

3.5 Dependence of focusing forces on particle size and Reynolds number

We performed similar analysis of migration velocities for particles of different sizes and for different flow velocities. Note that the migration velocity is a vector field $\mathbf{u}_m = (u_m, v_m)$, and recall that in our experimental setup, we can only measure the slow phase of inertial migration. This corresponds to measuring the x-component u_m of the migration along the manifold. We define the average migration velocity $\langle u_m \rangle$ as the average of $-\mathrm{sign}(x)u_m$ over all bins, where u_m is first averaged in each bin. The $-\mathrm{sign}(x)$ factor prevents left and right sides of the channel from canceling since u_m is an odd function across $x = 0$.

Average migration velocity $\langle u_m \rangle$ does not have a power law dependence upon particle
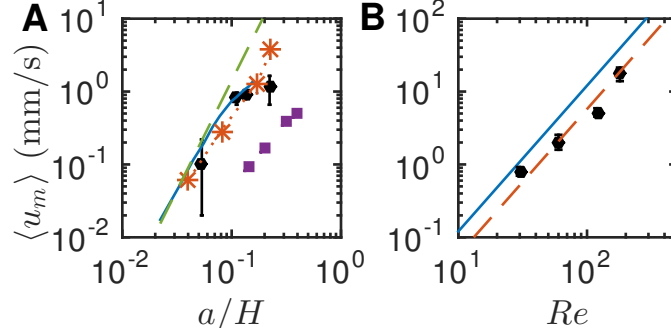
Figure 3.5: (A) Over the range of measured particle sizes there is no simple power law for the dependence of migration velocity upon particle size, a. Here we fixed $Re = 30$ and varied particle diameter (dashed green line: a^3 scaling law, blue line: Equation (5.4), black circles: measured average migration velocity $\pm$ s.e., orange stars: numerical prediction of average migration velocity). Zhou and Papautsky's [78] indirect measurements (purple squares) show a similar trend, but are an order of magnitude smaller. (B) Average migration velocities scale like U^2. Here we fixed particle diameter at $d = 12\mu m$ and varied the flow rate (blue line: Equation (5.4), dashed orange line: numerical fit of U^2 with one free parameter, black circles - measured average migration velocity$\pm$ s.e.).

size a, but agrees quantitatively with (5.4). For very small particles, migration velocities increase with a^3 scaling law, as predicted asymptotically [32, 63], but this power law breaks down even at small particle sizes. Incorporating an extra term in the series expansion produces good fit up to $\frac{a}{H} = 0.16$ in our data. To clarify that there is no conflict between numerical data and experimental data we computed the migration forces on a particle using the same finite element simulation that was used to extract the downstream velocity of the particle over a range of particle sizes ($\frac{a}{H} = 0.04, 0.08, 0.17$, and 0.23) that covered the entire experimental range. Numerical migration velocities averaged over the slow manifold agreed with experimental measurements and, over their range of validity, with the asymptotic series also (Fig. 3.5A).

Migration velocities scale like U^2. Asymptotic studies agree [32, 63, 36] that if particle size is fixed while the flow rate through the microchannel is varied then since in (3.1) both $\mathbf{u}$ and
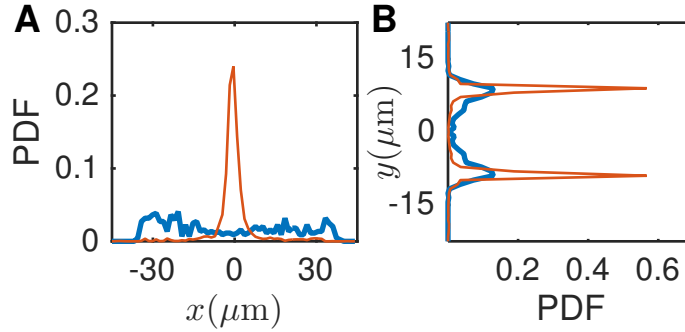
Figure 3.6: Particles enter the microchannel prefocused to a thin band of $y-$ coordinates, so only slow focusing dynamics can be measured. (A) The particle x-position PDF is nearly uniform at channel entry (thick blue line) becoming focused after traveling 1.5cm through the channel (orange line). (B) However, the particle y-position PDF is strongly focused both at entry (blue), and after particles have reached their focusing streamline. Recall that the reconstruction algorithm cannot decipher between $+y$ and $-y$ values, we have made the distribution symmetric to illustrate that both positive and negative $y-$values can be achieved. (Relative particle size $a/H = 0.11$, channel Reynolds number $Re = 30$).

$\bar{\mathbf{u}}$ vary in proportion to U, the total migration force $\mathbf{F}_L$ and total migration velocity u_m will scale like U^2. Our experimental measurements confirm this scaling (Fig. 3.5B). Experiments at much higher Reynolds numbers have shown that additional focusing positions appear in channel corners [14, 54], but we find no evidence of alternate focusing positions over the range $Re = 30 - 180$.

Our direct measurements of particle migration show that asymptotic theory adapted for rectangular micro-channels can quantitatively predict inertial lift forces on particles, including their dependence on particle size and channel velocity. Why have indirect measurements of migration velocities by Zhou and Papautsky [78] contradicted theory? First we note that our inertial migrational velocities are an order of magnitude larger than previous experiments (Fig. 3.5A), likely because indirect focusing measurements do not equally weight trajectories across the entire slow manifold, but rather only the slowest focusing that occurs as particles approach the focusing streamline. Additionally, Zhou and Papautsky [78] assume that par-

ticles are uniformly spread across the microchannel cross-section before focusing. We found that particles appeared to be uniformly dispersed (Fig. 3.6A) at the inlet. However, our reconstruction of particle depth showed that particles entered the microchannel already focused in their y-coordinate (Fig. 3.1B and 3.6B). Thus, our in-channel measurements showed only the second phase of inertial migration along a single slow manifold. Thus, pre-focusing makes it impossible to separate fast and slow phases of focusing in the manner attempted by Zhou and Papautsky [78].

3.6 Pre-focusing in the channel inlet

Pre-focusing is due to inertial lift forces acting in the channel inlet. We can use asymptotic theory to predict the ammount of prefocusing, which occurs primarily in the depth (y-) dimension where velocity shear is largest. In this section we will derive an expression for the y-distance a particle migrates in the channel inlet.

We model the inlet region as a linear contraction in the $x-$direction, with maximum width W_i at $z = -L_i$ and minimum width W_0 at the opening of the channel at $z = 0$, and constant depth H (Fig. 3.7). Assuming constant flow rate Q throughout the channel, and self-similar velocity profiles across each cross-section of the channel inlet, the downstream characteristic velocity in the inlet region takes the form: $U(z) = \frac{U_0 W_0}{W(z)}$, where $W(z)$ is the width of the channel inlet, specifically,

$$W(z) = W_0 - \frac{z}{L_i}(W_i - W_0). \tag{3.8}$$

For a particle lying on the symmetry plane $x = 0$, then the time-evolution of the y-component of the particle location obeys the ODE:

$$\frac{dy}{dt} = v_m(x = 0, y) \sim \frac{\rho U^2 a^3}{6\pi \mu H^2} c_L(x = 0, y). \tag{3.9}$$

Here we take the first order approximation of the migration velocity $\mathbf{u}_m = (u_m, v_m)$ in equation (5.4). By Taylor expanding the migration velocity around the equilibrium position

49

y_{eq}, and making the change of variables $Y = y - y_{eq}$ we obtain the following ODE:

$$\dot{Y} = -\Gamma(z)Y, \tag{3.10}$$

where $-\Gamma(z) = \frac{d}{dy}v_m$. Let $\Gamma_0 = \Gamma(0)$ be the rate of change of the migration velocity at the widest point of the channel $z = 0$, then since the migration velocity scales with U^2 we have:

$$\Gamma(z) = \frac{W_0^2}{W(z)^2}\Gamma_0. \tag{3.11}$$

So:

$$\frac{dY}{dz}\frac{dz}{dt} = \frac{dY}{dz}\frac{U_0 W_0}{W(z)} = -\frac{W_0^2}{W(z)^2}\Gamma_0 Y \tag{3.12}$$

Integrating and rearranging gives:

$$\frac{Y_0}{Y_i} = \left(\frac{W_0}{W_i}\right)^{\eta L_i} \quad, \text{ where } \quad \eta = \frac{\Gamma_0 W_0}{U_0(W_i - W_0)}. \tag{3.13}$$

From equation (5.4) we estimate:

$$\Gamma_0 = -120.3\left(\frac{a^3 Re U_0}{6\pi H^4}\right). \tag{3.14}$$

Using the channel dimensions from this experiment, with $Re = 30$ and $a = 5\mu$m, we find that particles are within 1.5μm of the equilibrium position y_{eq} by the end of the inlet region, $z = 0$, consistent with our measurements (Fig. 3.6B). However, little focusing occurs in the $x-$direction, so that if particle $x-$ positions only are measured, as in Zhou & Papautsky [78] particles appear to be uniformly dispersed across the channel (Fig. 3.6A).

Can a microchannel inlet be designed to measure fast-focusing dynamics? Equation (3.13) shows that shorter inlet regions (smaller values of L_i) lead to less particle pre-focusing. To enforce that focusing produces a less than 10% disturbance of particle depths during their passage through the inlet, i.e. that $\frac{Y_0}{Y_i} > 0.9$, we invert (3.13) and find that if the particle radius a is measured in microns, then the maximum inlet length, also in microns, is given by $L_i = 2100/a^3$. In particular for a particle with radius $a = 5\mu$m, the maximum channel inlet length is only $L_i = 17\,\mu$m.

However, to see fast-focusing dynamics there must also be fully developed Poiseuille flow at the channel inlet. The inlet must therefore be longer than the development length, L_d,
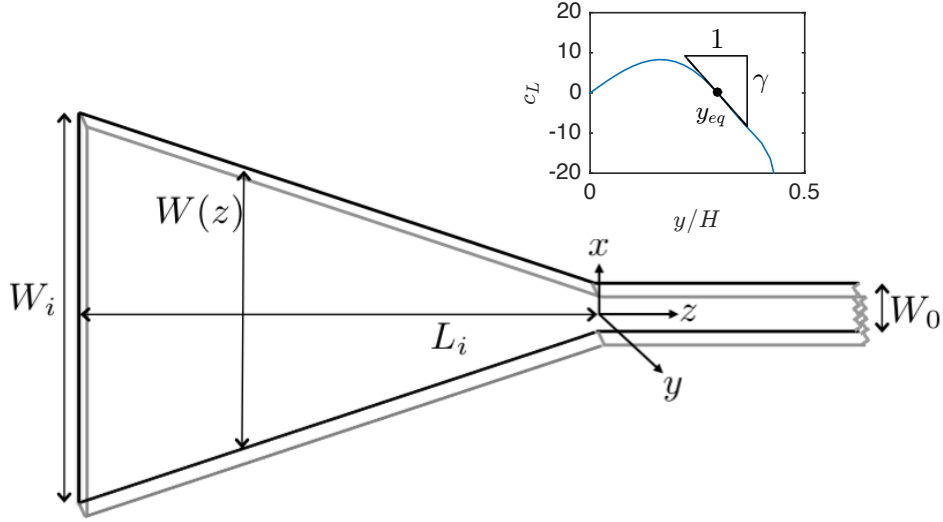
Figure 3.7: Diagram of inlet region (not to scale). (Inset) Plot of c_L, the particle lift force coefficient, the slope of the tangent line at the equilibrium focusing depth is $\gamma = -120.3$.

required for viscous boundary layers to diffuse from the channel floor and ceiling and to fill the entire channel. Ciftlik et al[14] give $L_d = \frac{1}{30} Re H = 45 \, \mu\text{m}$ at the lowest Reynolds numbers used in our experiments, exceeding the minimum L_i. These competing constraints make it impossible to design a microchannel inlet to measure fast focusing dynamics. Fast focusing dynamics can nevertheless be observed in glass capillaries [9] where inlet regions can be removed, however glass microfluidic capillaries can not be machined into *de novo* geometries.

3.7 Conclusions

The first reported experimental measurements of inertial migration velocities show that there is no conflict between asymptotic theory and the measured inertial migration velocities of particles in microchannels. However, a theory capable of quantitatively describing these forces does not produce a simple power law dependence of migration velocities upon particle size, contributing to previous contradictions between experiments, numerical data and theory. Additionally, we show that in soft lithography microchannels, fast focusing dynamics

51

occur in the channel inlet, causing pre-focusing of particles before they enter the microchannel imposing previously unexamined constraints over the control that can be exerted over particle focusing trajectories.

CHAPTER 4

Dynamical formation of one-dimensional microfluidic crystals

4.1 Introduction

Fluid inertia is a dominant effect in inertial microfluidic devices – aligning submerged particles to a finite number of preferred streamlines. Once particles are aligned on a streamline, viscous particle interactions produce regularly spaced chains of particles. These chains of particles can be viewed as a one-dimensional crystal lattice. While particle chains are exploited for high-speed imaging, flow cytometry, and entrapment of live cells in droplets for tissue printing applications [26]; there is no predictive theory that can be used to engineer devices. While mechanisms for chain formation have been suggested, there is still no quantitative theory for chain formation.

There are four dimensionless parameters that define the dynamics of chain formation in an inertial microfluidic channel. A rectangular channel with cross-section dimensions $H \leq W$ has an aspect ratio $AR = W/H$ (Figure 4.1A). Spherical particles with radius a have a relative particle size $\alpha = a/H$. The particles have density ρ and are suspended in a fluid with density ρ and viscosity μ. The suspension is pumped through the channel with an average velocity U. The channel Reynolds number is defined by $Re = \rho U H/\mu$, and the particle Reynolds number is defined as $Re_p = \alpha^2 Re = \rho U a^2/\mu H$.

The inertial lift force, which pushes particles across streamlines to a finite number of focusing streamlines, has been studied extensively both theoretically [32, 31, 2, 36, 57] and

53

study	Re	Re_p	α	AR	λ
Matas *et al.* [51]	$100 - 2600$	$0.5 - 8$	$0.015 - 0.03$	circular pipe	$2.5d - 4.5d$
Di Carlo *et al.* [24]	120	—	0.10	1	$3.6d$
Lee *et al.* [47]	$7.4 - 26.7$	—	$0.11 - 0.20$	2	$3d - 6d$
Humphrey *et al.* [37]	—	$0.8 - 1.3$	0.20	$0.8 - 6.4$	$4d$, $4.5d$
Kahkeshani *et al.* [40]	$30 - 120$	$2.8 - 8.3$	0.17	1.7	$2.5d$, $5d$
Reece and Oakey [59]	—	$0.1 - 1.5$	0.20	$1.6 - 9.6$	buckling

Table 4.1: A comparison experimental results with parameters Re, Re_p, α, AR, and the measured separation length λ between neighbors in a particle chain.

experimentally [64, 51, 23, 47, 8, 9, 78, 40]. Once particles are focused to their inertial focusing streamline, they interact with their neighbors to form chains. The equilibrium spacing λ between neighboring particles in a chain varies from $2d$ to $6d$, where $d = 2a$ is the particle diameter [51, 24, 47, 37, 40]. Futhermore, there are several trends between λ and other parameters (Table 4.1). The chain spacing λ decreases with Re_p [51, 40]. The chain spacing λ decreases as the particle volume fraction ϕ increases [37, 40]. Lattice Boltzman (LBM) simulations predict that there are attractors for pairs of particles at $\lambda = 2.5d$ (high Re_p) and $\lambda = 5d$ (low Re_p), but the chain spacing doesn't change with particle size α if AR is kept constant [40].

Different particle spacings have been observed between chains on the same focusing streamline and chains with particles on different focusing streamlines [47] (Figure 4.1B-C). Furthermore, it seems that there are different mechanisms for forming chains on the same streamline than for forming chains across streamlines. LBM simulations [37] of an inertially focused particle shows two stagnation points on the opposing streamline (Figure 4.1E) offset by a downstream length of $2d$ ($AR = 1.6$) or $2.25d$ ($AR = 2$). Thus a stable chain can form with particles alternating between two inertial focusing streamlines (Figure 4.1B).

How do chains form when particles are constricted to a single inertial focusing streamline? (Figure 4.1C) Chain formation is assumed to occur at the balance of attractive and replu-
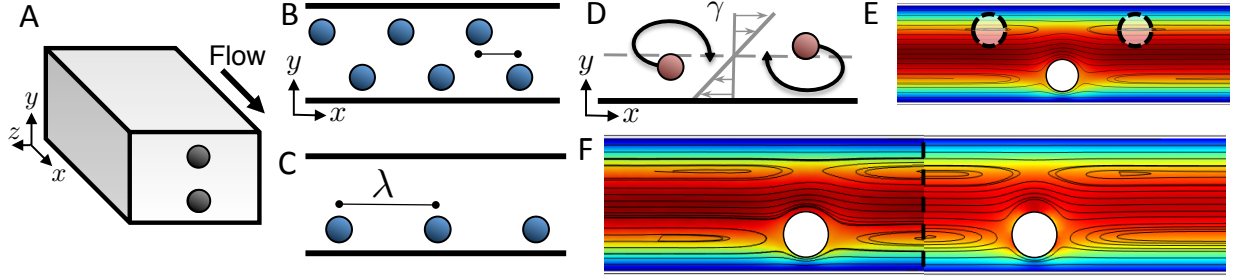
Figure 4.1: (A) In a rectangular channel with $AR = 1.7$, particles inertially focus to two streamlines on the symmetry plane $z = 0$. (B) Lattice of particles on two streamlines. (C) Chain on particles on the same streamline. (D) The trajectories for a pair of particles crystalizing in a shear flow with inertial focusing. (E) The streamlines around one inertially focused particle are reversing, but on the opposite side of the channel there are two closed eddies. (F) We solved the NSE numerically to compute the streamlines around two inertially focused particles (left) matches with Stokes equation approximation (right).

sive inter-particle forces. The repulsive forces appear to be symmetric, while the attractive forces appear to be nonsymmetric, and therefore are believed to have separate origins [47]. Lee *et al.* hypothesize that the repulsive forces are not due to fluid inertia – rather are due to viscous interactions with the channel wall pushing the particles away from the focusing streamline. This vertical displacement in a shear flow results in downstream displacement (Figure 4.1D). They assert that the attractive force arises from the inertial lift force pushing the particles back to their focusing streamliens and over-shooting, creating a harmonic oscillator type potential.

While this mechanism gives a qualitative theory of chain formation, it generates more questions about the dynamics of chain formation: What are the magnitudes of the attractive and repulsive forces? How do these forces depend on the experimental parameters α, Re, and AR? Can we predict the chain spacing λ as a function of the experimental parameters? While general trends are well documented, and numerical LBM simulations can predict dynamics for a single device, there is no theoretical model that can predict the particle spacing λ for a general class of devices and range of parameters Re, α, and AR. Such a theory could be

used to engineer devices to have a specific particle spacing λ.

4.2   Dimerization

To develop an asymptotic model of chain formation, we must determine the dominant balance of the terms in the Navier-Stokes equations (NSE) for interacting particles. The dominant balance for a single force-free and torque-free particle in a channel has been studied extenisively [18, 32, 63, 2, 36]. Near the particle, the flow can be modeled by a stresslet — a singularity approximation of an infinitessimal particle in a viscous shear flow [3, 32, 63, 36], in which case the dominant balance includes the viscous and pressure stresses. Recently, Hood *et al.* [36] showed that the near-particle approximation (dominant balance of viscous and pressure stresses) holds throughout the channel due to the fact that the no-slip boundary condition limits the growth of inertial stresses.

We find that the same dominant balance holds for two inertially focused particles. This can be seen from the streamlines around the particles: the streamlines in Navier-Stokes[1] flow match the streamlines in Stokes flow with the particles represented by stresslets (Figure 4.1E). Therefore, we claim that particle interactions are viscous. Fluid inertia only serves to focus the particles to the same streamline so that they must interact. This matches the mechanism proposed by Lee *et al.* [47], where viscous particle interactions are repulsive and inertial focusing is indirectly an attractive force.

Now we derive a viscous model of particle interactions [19, 43]. We consider the flow around two particles (radius a) near a wall located at $y = 0$. Initially, we assume the particles are inertially focused a distance h from the wall, and we assume symmetry in the $z-$direction. Each particle is centered at $(x_i, h, 0)$ for $i = 1, 2$ and has an image system centered at the reflection point across the wall $(x_i, -h, 0)$. Furthermore, we assume that $a \ll h \ll \lambda$.

The background flow in a rectangular channel is the Poisuille flow [55]. Here we will

---

[1]Verification of the NSE solver is presented in Appendix B.1

56

approximate this flow by its Taylor expansion in the coordinate y around h:

$$\bar{\mathbf{u}} \sim \beta + \gamma_y (y - h) + \delta_{yy}(y - h)^2 \,. \tag{4.1}$$

The flow around the particle can be derived using the Lamb's solution for the flow exterior to a sphere [44, 43]. Here we will only keep the terms that are $O(r^{-2})$ and $O(r^{-3})$. In order to derive the image system in the next step, we must convert the Lamb's solution into multipole singularities. In this case the $O(r^{-2})$ term becomes the stresslet $\mathbf{v}^{\mathrm{ST}}$, and the $O(r^{-3})$ term is decomposed into the source dipole $\mathbf{v}^{\mathrm{D}}$ and two stokeslet quadrupoles $\mathbf{v}^{\mathrm{SQ}}$ and $\mathbf{w}^{\mathrm{SQ}}$. Define $\mathbf{r}_i = (x - x_i, y - y_i, z - z_i)$ and $r_i = |\mathbf{r}_i|$, then the flow $\mathbf{v}_i^0 \sim \mathbf{v}_i^{\mathrm{ST}} + \mathbf{v}_i^{\mathrm{D}} + \mathbf{v}_i^{\mathrm{SQ}} + \mathbf{w}_i^{\mathrm{SQ}}$ around each particle satisfies

$$\mathbf{v}_i^{\mathrm{ST}} = -\frac{5\gamma_y}{2}\left[\frac{(x - x_i)(y - y_i)}{r_i^3}\mathbf{r}_i\right]\frac{1}{r_i^2}\,, \qquad \mathbf{v}_i^{\mathrm{D}} = -\frac{7\delta_{yy}}{24}\left[\mathbf{e}_x - \frac{3(x - x_i)}{r_i^2}\mathbf{r}_i\right]\frac{1}{r_i^3}\,, \tag{4.2}$$

$$\mathbf{v}_i^{\mathrm{SQ}} = -\frac{\delta_{yy}}{12}\left[\mathbf{e}_x - \frac{3(y - y_i)^2}{r_i^2}\mathbf{e}_x - \frac{3(x - x_i)}{r_i^2}\mathbf{r}_i + \frac{15(x - x_i)(y - y_i)^2}{r_i^4}\mathbf{r}_i\right]\frac{1}{r_i^3}\,, \tag{4.3}$$

$$\mathbf{w}_i^{\mathrm{SQ}} = -\frac{5\delta_{yy}}{24}\left[-\mathbf{e}_x + \frac{3(y - y_i)^2}{r_i^2}\mathbf{e}_x - \frac{6(x - x_i)(y - y_i)}{r_i^2}\mathbf{e}_y - \frac{3(x - x_i)}{r_i^2}\mathbf{r}_i\right. \tag{4.4}$$

$$\left. + \frac{15(x - x_i)(y - y_i)^2}{r_i^4}\mathbf{r}_i\right]\frac{1}{r_i^3}\,.$$

For each particle, we model the viscous wall effects by computing the image system for a plane wall. Blake [4] derived the image system for a stokeslet, an using a similar procedure we derive the image systems for the stresslet $\mathbf{v}^{\mathrm{STim}}$, source dipole $\mathbf{v}^{\mathrm{Dim}}$, and stokeslet quadrupoles $\mathbf{v}^{\mathrm{SQim}}$ and $\mathbf{w}^{\mathrm{SQim}}$ [5, 71]. Define $\mathbf{R}_i = (x - x_i, y + y_i, z - z_i)$ and $R_i = |\mathbf{R}_i|$. Then the image system for the stresslet is:

$$\mathbf{v}_i^{\mathrm{STim}} = \left[\frac{(x - x_i)(y + y_i)}{2R_i^3}\mathbf{R}_i - \frac{5yy_i(x - x_i)(y + y_i)}{R_i^5}\mathbf{R}_i + \frac{yy_i(y + y_i)}{R_i^3}\mathbf{e}_x\right. \tag{4.5}$$

$$\left. - \frac{y_i^2(x - x_i)}{R_i^3}\mathbf{e}_y\right]\frac{5\gamma_y}{R_i^2}$$

The image system for the source dipole is:

$$\mathbf{v}_i^{\mathrm{Dim}} = \frac{\delta_{yy}}{4}\left[\frac{30y(y + y_i)}{R_i^4}\mathbf{R}_i - \frac{3(3y + y_i)}{R_i^2}\mathbf{R}_i - \frac{6(y^2 - y_i^2)}{R_i^2}\mathbf{e}_y - \mathbf{e}_y\right]\frac{1}{R_i^3} \tag{4.6}$$

57

The image system for the first stokeslet quadrupole is:

$$\mathbf{v}_i^{\text{SQim}} = -\frac{\delta_{yy}}{24}\left[\frac{3(x-x_i)}{R_i^2}\mathbf{R}_i - \frac{15(x-x_i)(y+y_i)^2}{R_i^4}\mathbf{R}_i - \frac{30yy_i(x-x_i)}{R_i^4}\mathbf{R}_i \right.$$

$$+ \frac{210yy_i(x-x_i)(y+y_i)^2}{R_i^6}\mathbf{R}_i - \frac{30y_i(x-x_i)(y^2-y_i^2)}{R_i^4}\boldsymbol{e}_y$$

$$\left. - \frac{6y_i(x-x_i)}{R_i^2}\boldsymbol{e}_y - \frac{30yy_i(y+y_i)^2}{R_i^4}\boldsymbol{e}_x + \frac{3(y+y_i)^2}{R_i^2}\boldsymbol{e}_x + \frac{6yy_i}{R_i^2}\boldsymbol{e}_x - \boldsymbol{e}_x\right]\frac{1}{R_i^3}. \qquad (4.7)$$

Finally, the image system for the second stokeslet quadrupole is:

$$\mathbf{w}_i^{\text{SQim}} = -\frac{5\delta_{yy}}{24}\left[\frac{3(x-x_i)}{R_i^2}\mathbf{R}_i - \frac{15(x-x_i)(y+y_i)^2}{R_i^4}\mathbf{R}_i - \frac{30(x-x_i)(2y+3y_i)}{R_i^4}\mathbf{R}_i\right.$$

$$+ \frac{210yy_i(x-x_i)(y+y_i)^2}{R_i^6}\mathbf{R}_i - \frac{30y_i(x-x_i)(y^2-y_i^2)}{R_i^4}\boldsymbol{e}_y - \frac{3(y+y_i)^2}{R_i^2}\boldsymbol{e}_x$$

$$\left. + \frac{6(x-x_i)(y-2y_i)}{R_i^2}\boldsymbol{e}_y + \frac{6y(2y+3y_i)}{R_i^2}\boldsymbol{e}_x - \frac{30yy_i(y+y_i)^2}{R_i^4}\boldsymbol{e}_x + \boldsymbol{e}_x\right]\frac{1}{R_i^2}. \qquad (4.8)$$

Then the flow around each particle is:

$$\mathbf{v}_i \sim (\mathbf{v}_i^{\text{ST}} + \mathbf{v}_i^{\text{STim}}) + (\mathbf{v}_i^{\text{D}} + \mathbf{v}_i^{\text{Dim}}) + (\mathbf{v}_i^{\text{SQ}} + \mathbf{v}_i^{\text{SQim}}) + (\mathbf{w}_i^{\text{SQ}} + \mathbf{w}_i^{\text{SQim}}). \qquad (4.9)$$

For each particle we can compute the induced velocity from the other particle and image system,

$$\mathbf{U}_1 = \left(1 + \frac{a^2}{6}\nabla^2\right)(\bar{\mathbf{u}} + \mathbf{v}_2)\Big|_{\mathbf{x}=\mathbf{x}_1}, \qquad \mathbf{U}_2 = \left(1 + \frac{a^2}{6}\nabla^2\right)(\bar{\mathbf{u}} + \mathbf{v}_1)\Big|_{\mathbf{x}=\mathbf{x}_2}. \qquad (4.10)$$

Then we define the relative velocity $d\mathbf{U} = \mathbf{U}_2 - \mathbf{U}_1$. The particles are considered to be in equilibrium when their induced velocities are equal, that is $d\mathbf{U} = 0$. Then we define the separation length as $dx = x_1 - x_2$. The objective is to find dx for which $d\mathbf{U} = 0$.

Let $d\mathbf{U} = (dU, dV, dW)$, then each component satisfies:

$$dU = -\frac{10\gamma_y h dx^2(dx^2 + 5h^2)}{3(dx^2 + 4h^2)^{7/2}}, \qquad (4.11)$$

$$dV = -\frac{5\gamma_y a^2}{3dx^4} + \frac{10h^2\gamma_y dx(dx^4 - 12h^2 dx^2 - 64h^4)}{(dx^2 + 4h^2)^{9/2}} + \frac{5a^2\gamma_y dx(dx^4 - 72h^2 dx^2 + 256h^4)}{3(dx^2 + 4h^2)^{9/2}}$$

$$\qquad (4.12)$$

$$+ \frac{5h^3\delta_{yy}dx(27dx^4 + 20h^2 dx^2 - 352h^4)}{(dx^2 + 4h^2)^{11/2}} + \frac{10ha^2\delta_{yy}dx(15dx^4 - 265h^2 dx^2 + 464h^4)}{3(dx^2 + 4h^2)^{11/2}},$$

$$dW = 0. \qquad (4.13)$$
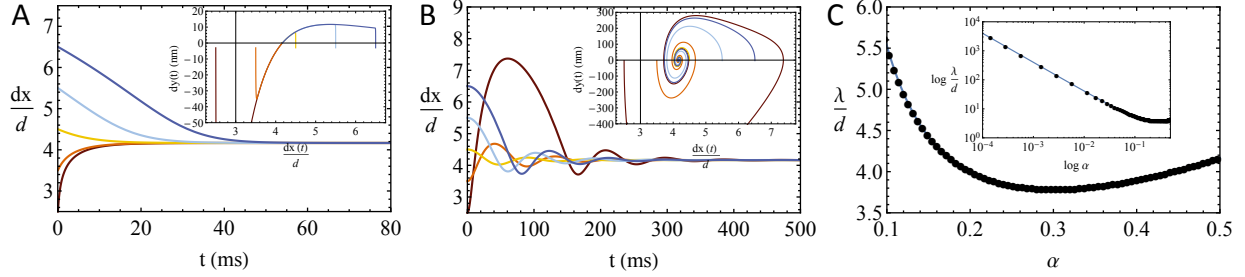
Figure 4.2: (A) The separation of two particles $dx(t)$ as a function of time for $Re = 30$, $a = 6\mu m$, and different initial separation lengths. (Inset) The dynamics of (dx, dy) as a function of time are overdamped. (B) The dynamics for $a = 6\mu m$ and $Re = 1$ are underdamped. (C) The equilibrium separation length λ is a function of the relative particle size α matches equation (4.16). Here λ is independent of Re. (Inset) The equilibrium separation length λ has a singularity of α^{-1} near zero.

We can model inertial focusing by Taylor expanding the migration velocity from Hood et al. [35] in the coordinate y around h. This gives $\dot{y}_i = -\Gamma(y_i - h)$, where the inertial focusing constant is $\Gamma = 120.3 U Re a^3/6\pi H^4$. Combining the visous particle interactions $d\mathbf{U} = (dU, dV, 0)$ with the inertial focusing we arrive at a system of ODEs for the dynamics of particle interactions:

$$\dot{x} = dU, \qquad\qquad dx(0) = k_0 d, \qquad\qquad (4.14)$$

$$\dot{y}_i = V_i - \Gamma(y_i - h), \qquad y_i(0) = h, \qquad i = 1, 2. \qquad (4.15)$$

The ODEs depend explicitly on the particle size α, the Reynolds number Re, and the initial separation length $k_0 d$. The equations implicitly depend on the channel aspect ratio AR, but throughout this paper we will consider the same channel as Kahkeshani et al. [40], where $W = 60\mu m$, $H = 35\mu m$, and $AR = 1.7$.

Solving ODEs (4.14-4.15) numerically for $Re = 30$, $a = 6\mu m$, and various initial conditions shows that there is an equilibrium separation length $\lambda = 4.15d$ (Figure 4.2A). The existence and stability of λ is promising, and the value $\lambda = 4.15d$ is consistentent with the experimental measurements of Kahkeshani et al. [40]. The dynamics of (dx, dy) shows that

59

the system is an overdamped harmonic oscillator (Figure 4.2B). In contrast, the same system for $Re = 1$ converges to the same value of $\lambda = 4.15d$, but the harmonic oscillator becomes underdamped (Figure 4.2B). As a result, the Re is a measurement of the damping of the harmonic oscillator.

Furthermore, we use numerical solutions of equations (4.14-4.15) to invesigate the dependence of λ on the relative particle size α (Figure 4.2C). The equilibrium separation length can be approximated by:

$$\frac{\lambda}{d} = \frac{0.40}{\alpha} + 1.06 + 4.60\alpha \,. \tag{4.16}$$

As the particle size vanishes, the equilibrium separation length grows like $1/\alpha$ (Figure 4.2C Inset). We note that the scaling length λ/d is independent of Re. That is, Re does not impact the equilibrium of the system, only the degree of damping.

We have shown that, in order to engineer a given chain separation length λ, one must tune the particle size α. However, thus far we have assumed that both particles have the same radius a. What is the separation length λ for two particles of different radii a and b? Let $b = \kappa a$ and define the averaged diameter of the two particles $d_\kappa = (1 + \kappa)a$. We will also denote λ_κ to be the equilibrium separation length for two particles with sizes a and κa. Now we can solve the ODEs (4.14-4.15) numerically for a range of κ.

We observe that for $Re = 30$ and $a = 6\mu$m, as κ decreases from 1, so does dx/d_κ (Figure 4.3A). The dynamics of (dx, dy) show that the system remains overdamped, but the equilibrium point moves negatively both in dx in dy, relative to the $\kappa = 1$ case (Figure 4.3A Inset). Overall, λ_κ/d_κ is a quadratic function with a minimum at $\kappa = 0.53$ and a max at $\kappa = 1$ (Figure 4.3B). When $Re = 1$ we see that initially, as κ decreases, so does λ_κ/d_κ (Figure 4.3B). However, comparing λ_κ/d_κ over the full range of κ we see very different behavior between $Re = 30$ and $Re = 1$ (Figure 4.3C). At $Re = 1$, λ_κ/d_κ is a quadratic function with a minimum at $\kappa = 0.86$ and a maximum near $\kappa = 0$ (Figure 4.3C). Here, Re not only impacts damping but also the equlibrium separation length λ_κ/d_κ.
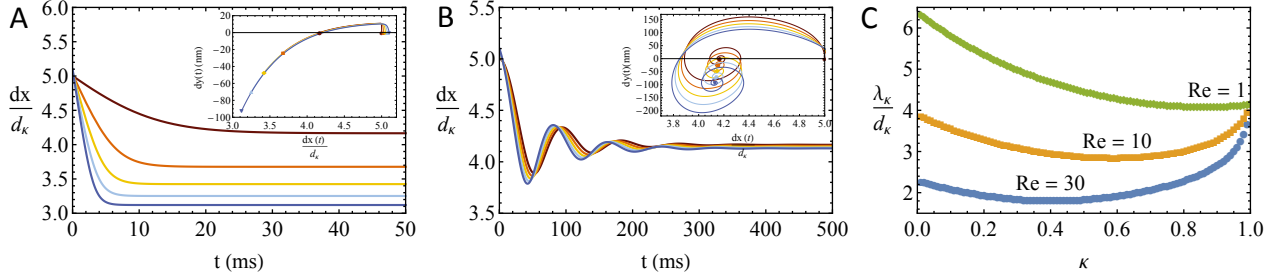
Figure 4.3: (A) The separation of two particles $dx(t)$ as a function of time for $Re = 30$, $a = 6\mu$m, and different relative sized particles with ratio $\kappa = 1$ (red), $\kappa = 0.99$ (orange), $\kappa = 0.98$ (yellow), $\kappa = 0.97$ (light blue), and $\kappa = 0.96$ (dark blue). (Inset) As κ decrases the final separation length $\lambda/(1+\kappa)a$ decreases while the final $y-$displacement increases. The dynamics of (dx, dy) as a function of time are overdamped. (B) The dynamics for $Re = 1$ are underdamped. (C) The equilibrium separation length $\lambda/(1+\kappa)a$ as a function of decreasing κ is parabolic and decreasing for $Re = 30$ and $Re = 10$ and parabolic and increasing for $Re = 1$.

4.3 Trimerization

Is this the only mechanism for the formation of chains? Humphry *et al.* [37] argued that cross-channel chains form because particles would focus at the center of a closed eddy (Figure 4.1E). We showed that two inertially focused particles on the same streamline produce a closed eddy at their midpoint (Figure 4.1F), and by the same argument, a particle could focus at the midpoint. Here we prove that the inertial lift force can make a particle focus at the center of a closed eddy.

We will derive a system of ODEs for the particle dynamics near an eddy. We choose our coordinates so that $y = 0$ is the inertial focusing streamline and $x = 0$ is the midpoint between two inertially focused particles. Then streamlines show that an elliptical closed eddy forms with major axis $2r$ and minor axis $2c$ (Figure 4.4B). We represent this closed eddy by the equations:

$$\dot{y} = -\omega^2 x, \qquad \dot{x} = \frac{r^2\omega^2}{c^2}y.$$

(4.17)

61

Here ω^2 is determined by the velocity near the eddy. For example, if the eddy is generated by a stresslet, $\omega^2 = 5\gamma\alpha^5/2r^5$.

We add inertial lift force to this ODE system by adding the term $-\Gamma y$ to the equation for $\dot{y}$. Rearranging terms, we arrive at a damped oscillator equation:

$$\ddot{x} + \Gamma\dot{x} + \frac{r^2\omega^4}{c^2}x = 0\,, \tag{4.18}$$

the solution of which is:

$$x(t) = x_0 \exp^{-\frac{\Gamma}{2}t}\cos(\omega_0 t)\,, \quad \omega_0 = \sqrt{\Gamma^2 - \frac{4r^2\omega^4}{c^2}}\,. \tag{4.19}$$

This implies that the particle spirals inwards towards the center of the closed eddy with frequency ω_0 and decay rate $\Gamma/2$.

This reduced model shows that if a particle is placed between two stationary particles on an inerital focusing streamline, it will find the midpoint of the two particles. This is an argument against a set scaling length for particle chains, since the midpoint has no set scale.

However, this model relies on the assumption that the two outside particles are stationary, which is generally not true. Instead we need to model three freely moving particles. We now turn to the viscous model described above for two particles. For each particle $i = 1, 2, 3$, we know the flow areound a particle near a wall $\mathbf{v}_i$ from equation (4.9). Then the induced velocities from the neighboring particles become:

$$\mathbf{U}_i = \left(1 + \frac{a^2}{6}\nabla^2\right)(\bar{\mathbf{u}} + \mathbf{v}_{i-1} + \mathbf{v}_{i+1})\Big|_{\mathbf{x}=\mathbf{x}_i}\,. \tag{4.20}$$

Then we solve the ODE system:

$$\dot{dx} = U_2 - U_1, \qquad dx(0) = k_0 d, \tag{4.21}$$

$$\dot{gx} = U_3 - U_2, \qquad gx(0) = j_0 d, \tag{4.22}$$

$$\dot{y}_i = V_i - \Gamma(y_i - h), \qquad y_i(0) = h, \quad i = 1, 2, 3. \tag{4.23}$$

First we compare this model (4.21-4.23) to our reduced ODE model (4.18). We fix the two outside particles at a distance L from each other, and define $dx = x_2 - x_1$. Then a chain
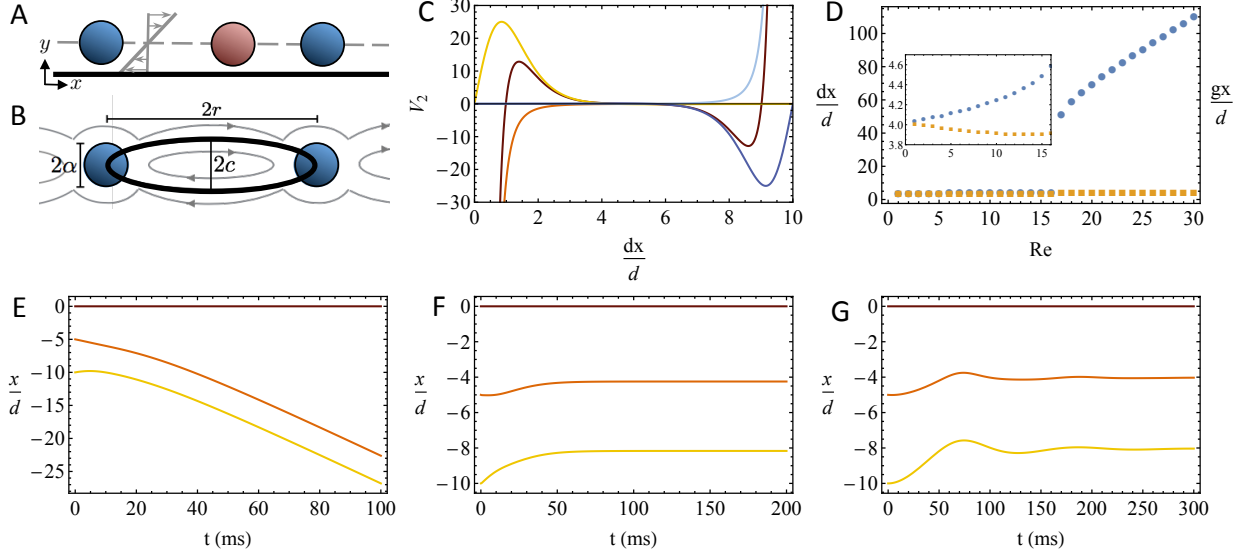
Figure 4.4: (A) Diagram for three particles. (B) Diagram of the elliptical streamlines shows that the length of the major axis is $2r$ and the length of the minor axis is $2c$. (C) The velocity V_2 of the center particle as a function of dx (red) broken into its constituent parts: contributions from particle 1 (orange) and the image of particle 1 (yellow), from particle 3 (light blue) and the image of particle 3 (dark blue). (D) The separation lengths dx/d (blue) and gx/d (orange) at $t = 500$ms as a function of Re. (E-G) Full ODE solution for three particles for (E) $Re = 30$, (F) $Re = 10$, and (G) $Re = 1$.

is formed with separation lengths dx and $L - dx$ when $V_2(dx) = 0$. In the case $L = 10d$, the separation lengths are equal, $dx = 5d = L - dx$ (Figure 4.4C). Furthermore we can break V_2 down into its constituent parts: interactions with particle 1, particle 1's image, particle 3, and particle 3's image. The interactions with the particles are both repulsive, while the interactions with the images are are attractive (Figure 4.4C). The reduced ODE model (4.18) only includes the repulsive particle forces. However, both models agree that the center particle will focus to the midpoint of two stationary particles. However, since $L > 2\lambda$, there is a range of dx for which V_2 is small but nonzero. This range makes the dynamics unstable.

Now let's consider three freely moving particles and define $gx = x_3 - x_2$. One might

expect that is the particle system is initially symmetric, that is $dx = gx$, then the system should remain symmetric. However, numerically we find that almost instantaneously dx and gx diverge and symmetry is broken. Furthermore the dynamics strongly depend on Re. For $Re \geq 17$, gx converges while dx diverges (Figure 4.4D). For $Re \leq 16$, both gx and dx converge to about $4d$, but there is a slight discrepancy that grows as Re increases (Figure 4.4D Inset).

To visualize the dependence on Re, we plot the velocities $x_i(t)$ for $i = 1, 2, 3$ in the moving frame of x_1. We examine three cases: $Re = 30$, $Re = 10$, and $Re = 1$. At $Re = 30$, initially particle 2 is pushed towards particle 3. Since the system is overdamped, there is no opportunity for particle 2 to move back in the direction of particle 1. So particles 2 and 3 form a pair withour particle 1 (Figure 4.4E).

In contrast, at $Re = 10$ and $Re = 1$, the system is underdamped. So although initially particle 2 is pushed toward particle 3, damping is weak so that the repulsive force from particle 3 moves both particles 2 and 3 toward particle 1. After several cycles the system converges to an equilibrium (Figure 4.4F-G).

A three particle chain can form below a critical $Re \leq 16$. This limit is not unexpected because this model is a low Re approximation for the NSE. This limit on three isolated particles does not preclude the formation of trimers by other means. For example, in the $Re = 30$ case only a dimer forms, but it may interact with a singleton later on to form a trimer. Furthermore, we have shown that when the outside particles are stationary, the center particle finds the midpoint. But when all particles are allowed to move freely, the separation lengths are close to λ.

4.4   The crystalization process for long chains

Thus far we have shown two different mechanisms for chain formation. Dimerization produced a fixed length scale λ that depends on the particle size α. Trimerization produces chains that are equally spaced, and a priori do not have a set scale. Is the crystalization pro-

cess driven by the dimerzation mechanism (fixed λ) or the trimerization mechanism (equally spaced λ)? We investigate experimental data collect by Kahkeshani *et al.* [40] to determine the crystalization mechanism for long chains[2].

First some notation. A group of particles is considered to be a chain if the particles are all on the same side of the channel within 3μm of the inertial focusing streamline and the downstream distance between each particle is less than $8d$. We disregard the presence of particles on the opposite focusing streamline, because they are very rare. We measure the length of each chain and the mean downstream $z-$separation between each particle in the chain.
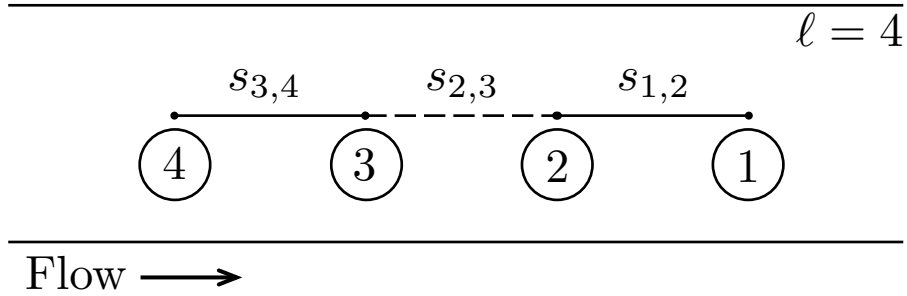
Figure 4.5: A chain with length $\ell = 4$.

We define ℓ, the length of a chain, to be the number of particles in the chain (Figure 4.5). We number each particle a number according to its downstream position, with the first or leading particle as the furthest downstream. We define the separation distance $s_{i,j}$ to be the z-distance between the i-th and j-th particle. We define the average separation distance $\langle s \rangle$ to be the average of all separation distances in the chain, specifically:

$$\langle s \rangle = \frac{1}{\ell} \sum_{i=1}^{\ell-1} s_{i,i+1}. \tag{4.24}$$

The number of length ℓ chains decreases as ℓ increases — in fact the decay is exponential (Figure 4.6A). We compare the chain length with a stochastic coalescence model, as described by the Smoluchowski equations [1]. Recall that the Smoluchowski coagulation equations

---

[2]The experimental methods are described in Appendix B.2.
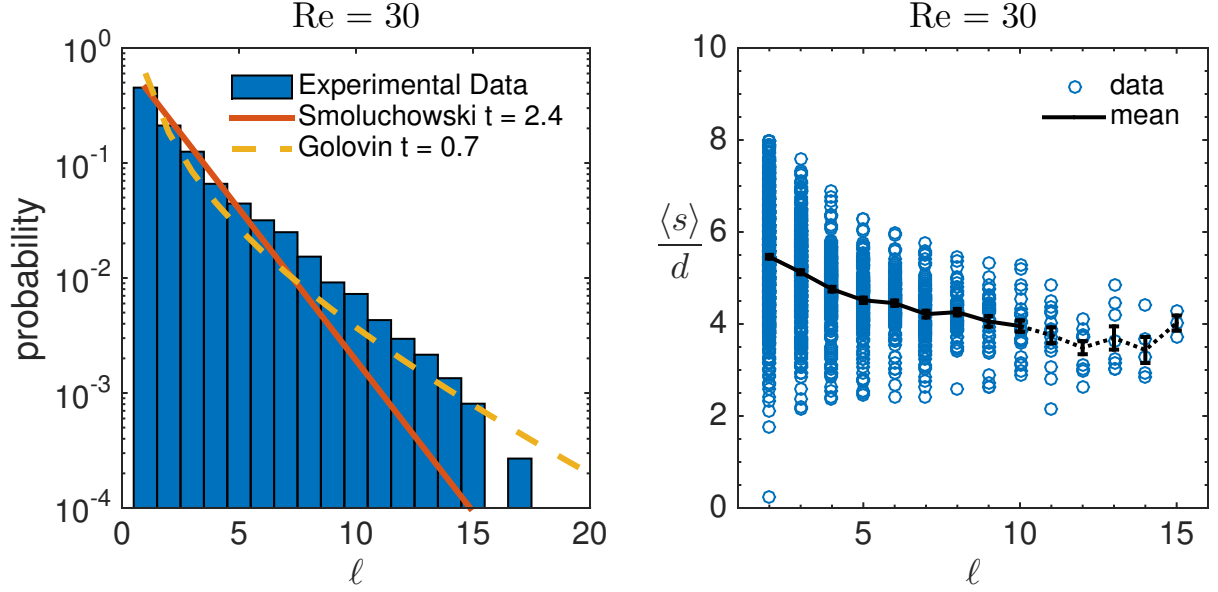
Figure 4.6: (A) PDF of chain length measured in the experiment compared to the PDF predicted by Smouluchowski equations (orange) and the Golovin equations (dashed yellow). (B) The mean separation length $\langle s \rangle$ between particles in a chain decreases as the chain length grows. The dotted line shows the mean $\langle s \rangle$ where the data are under-sampled. Data from the experiment with $Re = 30$ and $\alpha = 0.17$, error bars are standard error.

describe how particles merge into clusters according to the following rule: a cluster of size ℓ and a cluster of size ℓ' merge at (stochastic) rate $K(\ell, \ell')$, where K is a specified rate kernel. In our case, the size of a cluster is the length of a particle chain, which takes integer values. So we consider the discrete Smoluchowski equations for the evolution of $n(\ell, t)$ the number of clusters of size ℓ at time t:

$$\frac{d}{dt}n(\ell, t) = \frac{1}{2}\sum_{\ell'=1}^{\ell-1} K(\ell', \ell - \ell')n(\ell', t)n(\ell - \ell', t) - n(\ell, t)\sum_{\ell'=1}^{\infty} K(\ell, \ell')n(\ell', t). \qquad (4.25)$$

Smoluchowski derived an exact solution for (4.25) in the case that the specified rate kernel is $K(\ell, \ell') = 1$ [68]. This kernel implies that the probability of two clusters coalescing is independent of the size of the clusters. The resulting distribution is:

$$n_S(\ell, t) = \left(1 + \frac{t}{2}\right)^{-2} \left(\frac{t}{2+t}\right)^{\ell-1}. \tag{4.26}$$

Golovin [27] derived an exact solution for (4.25) in the case that the specified rate kernel is $K(\ell, \ell') = \ell + \ell'$. This kernel implies that the probability of two clusters coalescing is proportional to the sum of the cluster sizes. In order to express the Golovin distribution, we must first define the Borel distribution $B(\lambda, \ell)$, which is regarded as the total population size Z_λ in a Galton-Watson branching process with one progenitor and Poisson (λ) offspring distribution [1]. Explicitly,

$$B(\lambda, \ell) = P(Z_\lambda = \ell) = \frac{(\lambda \ell)^{\ell-1} e^{-\lambda \ell}}{\ell!}, \qquad \ell = 1, 2, 3, \ldots, \quad 0 \le \lambda \le 1. \tag{4.27}$$

Then the Golovin distribution is:

$$n_G(\ell, t) = e^{-t} B(1 - e^{-t}, \ell). \tag{4.28}$$

We compare our experimental data to the Smoluchowski distribution $n_S(\ell, t)$ in equation (4.26) and the Golovin distribution $n_G(\ell, t)$ in equation (4.28). The variable t is chosen so that $n(1, t)$ matches the number of chains with length 1 in the experimental data. In order to compare to experimental data the Smoluchowski and Golovin distributions must be rescaled. Because of the finite size of our view window, we can only observe chains lengths at most 20, and in particular chains with $\ell \le 10$ seem to be well sampled. So we renormalize the Smoluchowski and Golovin distributions so that they have the same mass as the experimental data when restricted to the set of chains with $\ell \le 10$.

The Golovin distributions shows better agreement with the experimental data than the Smoluchowski distribution (Figure 4.6A). While the Smoluchowski distribution is a fair fit, it under-predicts the number of chains with $\ell > 5$. Recall that the Golovin distribution has specified rate kernel $K(\ell, \ell') = \ell + \ell'$, which states that the probability of two chains coalescing is proportional to the sum of their lengths. This implies that the rules for forming a chain depend more on multiple particle interactions than on pairwise interactions, a trait observed in the trimerization process.

We also observe that the mean separation length $\langle s \rangle$ between particles in a chain decreases as the chain length increases (Figure 4.6B). This implies that there is no set scale for long chains. Trimerization also produced no set scale, only equally spaced chains.

Do chains of a given length ℓ have uniform spacing between particles? In order to test this hypothesis we must first make a few definitions. For a given chain of length ℓ, let s_* be the separation distance for a uniformly spaced chain. Specifically,

$$s_* = \frac{s_{1,\ell}}{\ell - 1}. \tag{4.29}$$

Now define S_ℓ to be the set of all length ℓ chains. Then we define $\bar{s}_\ell$ to be the average $\langle s \rangle$ over the set S_ℓ. Specifically.

$$\bar{s}_\ell = \frac{1}{|S_\ell|} \sum_{s \in S_\ell} \langle s \rangle. \tag{4.30}$$

Note that s_* is not constant over all chains with length ℓ, because the separation $s_{1,\ell-1}$ between the first and last particle varies for each measured chain. However, $\bar{s}_\ell$ is a constant as long as ℓ is kept constant.

Now we define a measure $\|s\|_2$ of uniformity of chain spacing. For a given chain of length ℓ, we define:

$$\|s - s_*\|_2 = \sqrt{\sum_{i=1}^{\ell-1} \frac{(s_{i,i+1} - s_*)^2}{s_*^2}}, \qquad \|s - \bar{s}_\ell\|_2 = \sqrt{\sum_{i=1}^{\ell-1} \frac{(s_{i,i+1} - \bar{s}_\ell)^2}{\bar{s}_\ell^2}}. \tag{4.31}$$

This norm resembles the Euclidean ℓ^2-norm for vectors in $\mathbb{R}^\ell$, and measures the relative deviation from a uniformly spaced chain. We then compute $\langle \|s\|_2 \rangle$, the mean $\|s\|_2$ over all chains of length ℓ. When $\langle \|s - s_*\|_2 \rangle = 0$ then the chain has uniform spacing, and when $\langle \|s - \bar{s}_\ell\|_2 \rangle = 0$ the the chains has the set spacing $\bar{s}_\ell$.

Running these statistics on the experimental data, we observe that $\langle \|s - \bar{s}_\ell\|_2 \rangle \sim 0.176$ and is roughly constant across ℓ (Figure 4.7). In contrast, $\langle \|s - s_*\|_2 \rangle$ is substantially lower than $\langle \|s - \bar{s}_\ell\|_2 \rangle$. On average $\langle \|s - s_*\|_2 \rangle \sim 0.086$ and it increases as ℓ increases. We conclude that the chains prefer to be equally spaced than to have the set spacing $\bar{s}_\ell$.

From our fitting of the experimental data we make three conclusions. First, since the Golovin distribution is the best fit of the experimental distribution of chain lengths, we
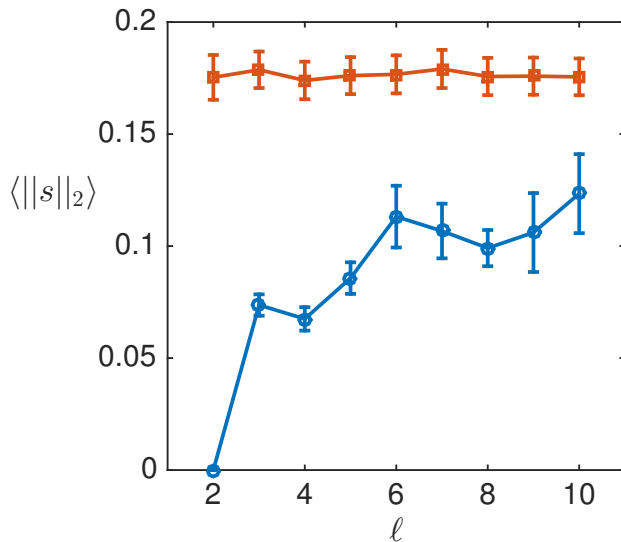
Figure 4.7: The relative deviation from uniformly spaced chain $\langle \|s - s_*\|_2 \rangle$ (blue circles) is less than the relative deviation from a chain with set length $\langle \|s - \bar{s}_\ell\|_2 \rangle$ (orange squares).

conclude that coalescence of chains is proportional to the relative lengths of each chain. This implies that many body interactions are more important for the dynamics than pairwise interactions. Secondly, since the mean separation length $\langle s \rangle$ decreases with chain length, we conclude that there is not a fixed preferred separation length. This also suggests that the interactions between particles are nonlocal, that is, the distance between two neighboring particles depends on the locations of all the particles in the chain. Thirdly, chains prefer to be uniformly spaced, however the ideal spacing varies with the length of the chain.

4.5 Conclusions

We have shown that the formation of one-dimensional microfluidic crystals is a dynamical procress. We derived a reduced model of the dynamics, the chief components of which are particle-particle interactions, particle-wall interactions, and inertial focusing. We find two mechanisms for crystalization: dimerization which has a fixed length scale λ, and trimerization which prioritizes being equally spaced but has not set scale. In experimental data, we observe that long chains prefer to be equally spaced, but have not set scale, similar to the

trimerization process.

We showed that the dimerization process for two particles of different sizes can be tuned by both the relative particle size κ and the channel Reynolds number Re. It is still an open question how different particle sizes impacts the trimerization process. If symmetry is broken, one might expect that the center particle should not find the midpoint of the two outer particles, but instead a sort of weighted average of the positions of the outside particles. Furthermore, how might having particles of different sizes impact the formation and scaling of long chains?

While there is no fundamental scale for the crystal, we believe that the scaling can be tuned by various parameters. In particular, there is an opportunity here for experiments to examine crystaliation for a suspension with particles of two different sizes. We suspect that tuning the concentration of each particle size will tune the length scale of the crystal.

We have reported a new mechanism for crystalization by a dynamical process. This crystalization cannot be adequately described by existing stochastic coagulation models. Furthermore, this dynamical procress allows the length scale to be tuned through the manipulation of experimental parameter. The dynamical crystalization process should be studied in more detail both theoretically and experimentally. We wonder if other systems exhibiting dynamical crystalization exist in nature.

CHAPTER 5

Number of focusing positions in inertial microfluidic channels

Can we engineer a channel to have any given number of inertial focusing positions? Thus far we have only considered rectangular channels, which because of the symmetry, particles must focus to either two or four inertial focusing positions. But with soft-lithography methods, inertial microfluidic devices can have channels with a wide range of cross-sections.

In this final chapter I publish some works in progress. While the stories here aren't completed, the partial results are illuminating and give greater insight into the physics of inertial focusing. First we derive a theory for the number of focusing positions in a rectangular channel. Then we develop a heuristic explanation of the inertial lift force in order to develop a theory for engineering devices.

5.1 Number of inertial focusing positions in a rectangular channel

While there has been great interest to model this inertial cross-stream migration theoretically and numerically [32, 63, 23, 36], there is yet disagreement on the number of focusing positions in rectangular channels [78]. In a circular pipe with radius R, Segré and Silberberg [64, 65, 66] reported that partices migrate to form a ring with radius $0.6R$. This observation is justified due to the rotational symmetry of the circular cross-section of the pipe (Figure 5.1A).

In a square channel, there is general consensus that particles focus to four positions [22], while some numerical studies [12, 57] suggest that there are an additional four focusing positions in the corners of the channel, especially at large Reynolds numbers (Figure 5.1B).
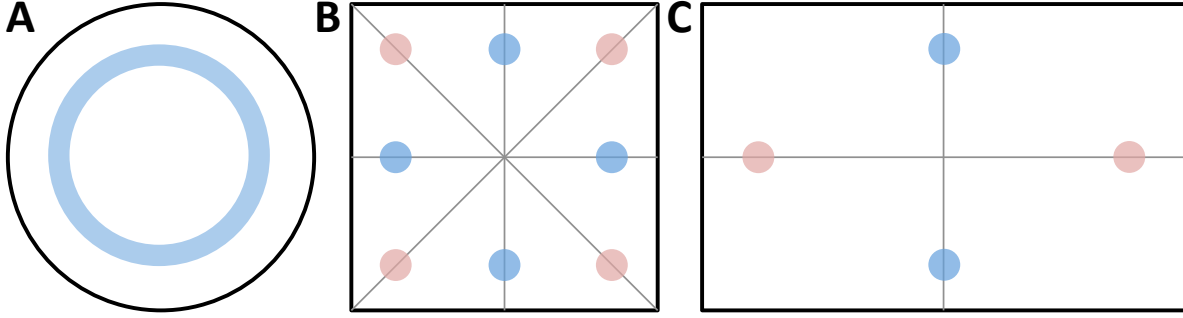
Figure 5.1: Inertial focusing positions for different channel cross-sections. (A) A circular cross-section has rotational symmetry and focuses particles to a ring. (B) A square cross–section has four lines of symmetry and focuses particles to either four focusing positions (blue) or eight (blue and red). (C) A rectangular cross-section has two lines of symmetry and focuses particles to either two focusing positions (blue) or four (blue and red).

Since a square channel has four lines of symmetry, we cannot a priori determine whether there are four or eight focusing positions. Additionally, standard optical methods involve recording streak images from above the channel and cannot distinguish between four and eight focusing positions [22, 78]. Using holographics techniques, Choi *et al.* [10] measure the PDF of particle position in the a square cross-section and observe only four focusing positions for $Re \leq 120$. In a similar experiment, Miura *et al.* [54] observe four focusing positions for lower Reynolds numbers ($Re = 260$) and eight focusing positions at higher Reynolds numbers ($Re = 444, 737$). Futhermore, Miura *et al.* observe the the four original focusing positions (Figure 5.1B blue) move towards the center of the channel as Re increases. It is unclear why the additional four focusing positions emerge at large Reynolds numbers.

In a rectangular channel particles focus to either two or four focusing positions [22, 78, 57] (Figure 5.1C). Due to the symmetry of the rectangular channel, we cannot a priori determine whether there are two or four focusing positions. Define the aspect ratio of a rectangular channel to be $AR = W/H$, where W is the long dimension of the cross-section and H the short dimension. Using lattice boltzman model (LBM), Prohm and Stark [57] fix $Re = 10$ and vary the AR of the channel. They suggest that there are four focusing positions at

lower aspect ratios ($AR = 2$), and two focusing positions at higher aspect ratios ($AR = 3$). Using numerical models, Liu *et al.* [49] fix $AR = 1, 2, 4, 6$ and vary the Re and particle size a/H. For $AR = 2$ and $a/H = 0.3$, Liu *et al.* predict that there are two focusing positions at $Re = 100$ and four focusing positions at $Re = 200$, and confirm with experiments. Furthermore, they predict that smaller particles ($a/H = 0.1$) will focus to four positions even at $Re = 100$.

Current numerical and experimental literature suggests that the number of focusing positions in a rectangular channel depends on three parameters: AR, Re, and a/H. General trends suggest that there are two focusing positions when Re is small, AR is large, and a/H is large. However, there is little theory explaining these observed behaviors.

In this section we use the asymptotic model of Hood *et al.* [36, 34] to understand the physics contributing to the number of focusing positions in rectangular channels. We show that indeed number of focusing positions depends on particle size. Furthermore, the failure of the side focusing positions is related to the failure of asymptotic series to converge. We predict when a channel will have four focusing positions and when it will have two focusing positions.

To begin our analysis, we consider a rectangular channel with aspect ratio $AR = 2$. Using the theory developed in Hood *et al.* [36], we calculate lift force at each point $\mathbf{x}_0$ in the cross-section, according to equation (5.10). As in Hood *et al.* [34], we find the migration velocity $\mathbf{u}_m = (u_m, v_m)$ of a force-free particle by equating the lift force (5.10) with the drag force computed for a particle translating with a general velocity $\mathbf{u}_m$ [30]. This drag force can be evaluated by the method of reflections, to the same order of accuracy as equation (5.10):

$$6\pi\mu a[\mathbf{u}_m(\mathbf{x}_0) + \mathbf{u}_{im}(\mathbf{x}_0)] = \mathbf{F}_L(\mathbf{x}_0), \tag{5.1}$$

where $\mathbf{u}_{im}$ is the leading order backflow created at $\mathbf{x}_0$ due to the walls of the microchannel. Furthermore, $\mathbf{u}_{im}(\mathbf{x}_0)$ is the first order correction calculated by the method of reflections for a small sphere migrating across streamlines and therefore is linearly related to the lift force $\mathbf{F}_L(\mathbf{x}_0)$, namely there exists a matrix $\mathbf{S}(\mathbf{x}_0)$ such that $\mathbf{u}_{im}(\mathbf{x}_0) \simeq \mathbf{S}(\mathbf{x}_0) \cdot \mathbf{F}_L(\mathbf{x}_0)$. The terms of

$\mathbf{S}(\mathbf{x}_0)$ are determined by computing the reflection $\hat{\mathbf{u}}_2$ of the test velocity $\hat{\mathbf{u}}$ and evaluating at the center of the particle $\mathbf{x}_0$. Rearranging the terms above for the migration velocity gives:

$$\mathbf{u}_m(\mathbf{x}_0) = \left[\mathbf{I} + \frac{a}{H}\mathbf{S}(\mathbf{x}_0)\right]\frac{\mathbf{F}_L(\mathbf{x}_0)}{6\pi\mu a}. \tag{5.2}$$

The pre-factor here represents the tensorial mobility of the particle.

We are interested in how particles travel due to this migration velocity, which can be computed at any point $\mathbf{x}_0$ in the channel. Let $\mathbf{X}(t) = (X(t), Y(t))$ be the location of a given particle in the channel cross-section as a function of time t. For a particle migrating due to inertial lift forces:

$$\frac{d\mathbf{X}}{dt} = \mathbf{u}_m, \qquad \mathbf{X}(0) = (x_0, y_0). \tag{5.3}$$

The slow-focusing manifold is evaluated numerically by advecting particles according to (5.3) and finding the curve Λ which is invariant under (5.3). Note that Λ depends on the relative particle size $\frac{a}{H}$. At any point $\mathbf{x}_0$ in the channel, the migration velocity satisfies

$$\mathbf{u}_m(\mathbf{x}_0) \sim \frac{\rho U^2 a^3}{6\pi\mu H^2}\left[\mathbf{I} + \frac{a}{H}\mathbf{S}(\mathbf{x}_0)\right] \cdot \left[\mathbf{c}_4(\mathbf{x}_0) + \frac{a}{H}\mathbf{c}_5(\mathbf{x}_0)\right]. \tag{5.4}$$

where the coefficients $\mathbf{c}_4(\mathbf{x}_0)$ and $\mathbf{c}_5(\mathbf{x}_0)$ are the same as those calculated in (5.10).

Following particle streamlines, we confirm that the migration trajectory is exhibits two phases of dynamics – a fast phase and slow phase (Figure 5.2B). During the fast phase dynamics particles migrate outwards to a one dimensional manifold in the channel (red line in Figure 5.2C). During the slow phase of dynamics the particles migrate along the manifold to the final inertial focusing points (circle and cross markers in Figure 5.2C).

Furthermore, we can determine the zones of attraction for each focusing point by numerically integrating equation (5.3) for each $\mathbf{x}_0$ in a grid spanning the channel cross-section. In a square channel, the attraction zones for each focusing point are equal in size (Figure 5.2A). However, the side focusing points (Figure 5.2C, $\times$ markers) have attraction zones that remain roughly constant in size as AR increases (Figure 5.2). In contrast, the attraction zones for the central focusing points grow as AR increases (Figure 5.2A). The size of the attraction zones indicate that the central focusing points are increasingly preferred as the AR increases.
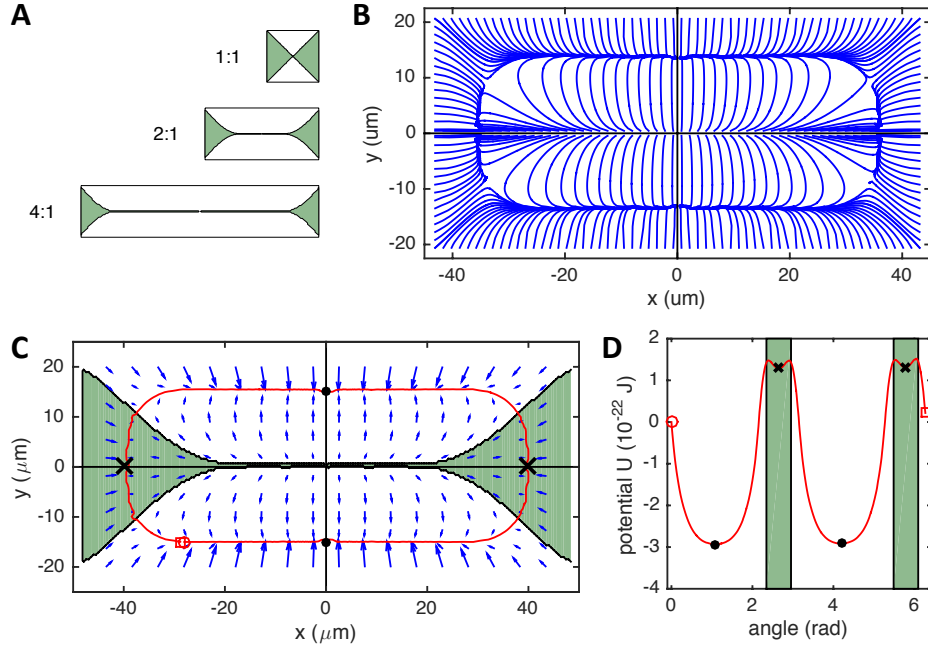
Figure 5.2: (A) The attraction zones for the side focusing points diminish as the aspect ratio increases. Here $Re = 30$ and $a/H = 0.022$ are kept constant. (B) In a channel with aspect ratio AR=2, $Re = 30$, and $a/H = 0.022$ the streamlines show that particles first migrate away from the center, then towards a one-dimensional manifold, and then along the manifold to the focusing point. (C) Particles migrate quickly to a one-dimensional manifold (red line), and then migrate slowly along the manifold to one of four focusing points. Particles that start in the shaded areas migrate to the focusing positions marked with an $\times$. (D) Integrating the negative force along the manifold gives the potential near each focusing point.

Interestingly, the focusing points along the short sides are stable, and not unstable equilibrium points. However, if particles have enough energy, either from thermal diffusion, particle interactions, or some other means, it is possible for particles to leave one stable focusing point, and migrate towards another. By integrating the negative lift force along the manifold, we can calculate the depth of the potential wells around each focusing point (Figure 5.2D). The depth of the potential of the focusing point along the long side of the channel is much greater than the depth of the side focusing point potentials, their ratio being 25.

5.1.1 Diffusion out of the potential well

Is it posible that particles can diffuse out of the potential well for the side focusing points? Using brownian dynamics we can calculate the time needed for a particle to diffuse out of the potential wells. Consider a particle in the slow phase of its inertial migration, moving along the one-dimensional focusing manifold towards the focusing point (Figure 5.2C). The potential along the manifold shows that each inertial focusing position is at the bottom of a potential well (Figure 5.2D). Our objective is to calculate the time needed for a particle to diffuse out of the potential well using brownian dynamics.

Let $x(t)$ be the position of the particle as a function of time. Define the diffusion constant $D = k_B T / 6\pi\mu a$ and the linearization of the potential $b = \beta/6\pi\mu a$, that is the friction coefficent reduced by the drag coefficent. Let $\xi(t)$ be gaussian white noise, satisfying:

$$
\begin{aligned}
< \xi(t) > &= 0 \,, \\
< \xi(t_1)\xi(t_2) > &= 2D\delta(t_1 - t_2) \,.
\end{aligned}
$$

Then $x(t)$ satisfies the overdamped Langevin equation [48] for a harmonic oscillator:

$$
\dot{x} + bx = \xi(t) \,. \tag{5.5}
$$

We see that $x(t)$ has the following solution:

$$
x(t) = x(0) + \int_0^t \xi(t_1)e^{b(t_1-t)}dt_1 \,. \tag{5.6}
$$

Then, the mean square displacement is:

$$
\begin{aligned}
< \sigma^2 > &= < [x(t) - x(0)]^2 > \\
&= \int_0^t dt_1 \int_0^t e^{b(t_1-t)}e^{b(t_2-t)} < \xi(t_1)\xi(t_2) > dt_2 \\
&= \int_0^t dt_1 \int_0^t e^{b(t_1+t_2-2t)} 2D\delta(t_1 - t_2)dt_2 \\
&= 2D \int_0^t e^{2b(t_1-t)}dt_1 \\
&= \frac{D}{b}\left[1 - e^{-2bt}\right] \,.
\end{aligned}
$$

Notice that as $t \to \infty$, the mean square displacement goes to a constant:

$$< \sigma^2 >_{t \to \infty} = \frac{D}{b} = \left(\frac{k_B T}{6 \pi \mu a} \right) \left(\frac{6 \pi \mu a}{\beta} \right) = \frac{k_B T}{\beta} .$$

In our simulation for AR=2, we find $b = \beta / \gamma$, where $\beta = 4 \, \mu\text{N/m}$ and $\gamma = 6 \pi \mu a$ is the drag coefficient. As well, for a particle to leave the small well, it must travel a distance of about $d = 25 \, \mu\text{m}$. So we can find the average time it takes to leave the well by solving: $d^2 = \frac{D}{b} \left[1 - e^{-2bt} \right]$. This yields the following equation for t_D, the time to diffuse out of the small potential well:

$$t_D = \frac{-1}{2b} \ln \left[1 - \frac{b d^2}{D} \right] = \frac{-3 \pi \mu a}{\beta} \ln \left[1 - \frac{\beta d^2}{k_B T} \right] . \tag{5.7}$$

So, in order to have mean square displacement as large as d^2 in finite time, we need:

$$k_B T > \beta d^2 = (4 \, \mu\text{N/m})(25 \, \mu\text{m})^2 = 2.5 \, \text{fJ} .$$

Comparing the two potential wells, we find that they have the same slope $\beta = 4 \, \mu\text{N/m}$, the only difference is the depths (and correspondingly widths d) of the wells.

If we assume $\frac{b d^2}{D} \ll 1$, then we can make the approximation $t_D \approx d^2 / D$. So if we want to clear the small potential well in $t_D = 5 \, \text{ms}$, then we must have $D \approx d^2 / t_D = 1.25 \times 10^{-7} \, \text{m}^2/\text{s}$. If we want to clear the small potential well in $t_D = 50 \, \text{ms}$, then we must have $D \approx d^2 / t_D = 1.25 \times 10^{-8} \, \text{m}^2/\text{s}$. Thermal diffusion is not strong enough to deplete the side focusing points. In contrast, particle interactions are on the correct order of magnitude.

5.1.2 Diffusion by particle interactions

Do particle interactions influence the number of focusing positions in a rectangular channel? We have shown that particle interactions give rise to a diffusion constant that is the correct order of magnitude. But in experiments, the volume fraction is deliberately chosen so that particle interactions are rare.
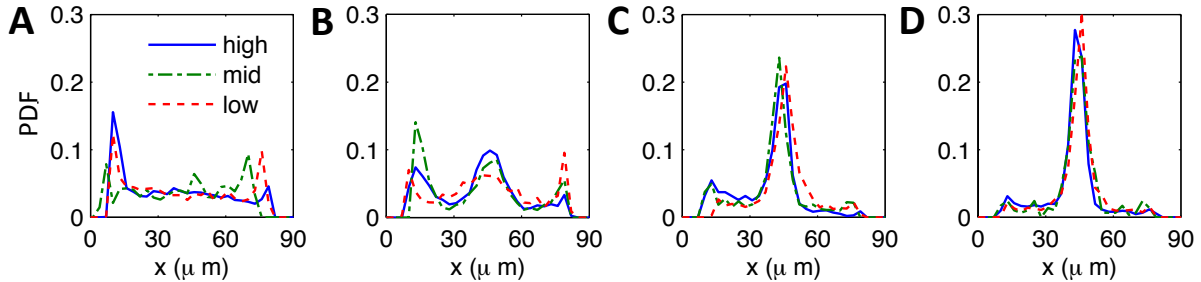
Figure 5.3: Distribution of particles measured across the channel, at downstream lengths of (A) $0.1L$, (B) $0.4L$, (C) $0.7L$, and (D) $0.9L$. We consider 12μm diameter particles in channels with height $H = 45\mu$m and width $W = 90\mu$m at Reynolds number $Re = 36$. We plot the results using three different particle fractions: $\phi = 0.009$ (blue), $\phi = 0.003$ (green), and $\phi = 0.001$ (red).

If particle interactions are the source of diffusion out of the side focusing points, the the number of focusing points should vary with the particle volume fraction. At low particle fractions, particle interactions are rare, so we should observe particles focusing to four focusing positions. In contrast, at high particle fractions interactions are common, so we should observe particles leaving the side focusing points and focusing to only to the two central focusing points.

To show that the number of focusing positions are not a result of particle interactions, we will show that they are independent of particle volume fraction. We run experiments similar to those in Hoo *et al.* [35]. The channel has cross-section with side lengths $H = 45\mu$m and $W = 90\mu$m, and we choose $Re = 30$. The particles have radius $a = 6\mu$m and we vary the particle fraction from $\phi = 0.001$ to 0.009. The channel has downstream length $L = 15$mm, and we record videos at downstream lengths of $0.1L$, $0.4L$, $0.7L$, and $0.9L$. In each video we record the $x-$position of each particle and create a PDF of particle position.

The experimental data showed that the PDF of particles are similar for all three volume fractions (Figure 5.3). Even though the initial PDF varies slightly for each particle fraction, the PDFs at $0.9L$ match extremely well across ϕ. We conclude that focusing is independent

of particle fraction, and therfore particle interactions are not the source of diffusion out of the side focusing points.

5.1.3 Breakdown with particle size

Thus far we have shown that in theory, particles may diffuse out of the side focusing points. However, the diffusion constant required is very large. This diffusion is too large to be thermal fluctuations, and particle interactions are too rare to be the source of diffusion.

Another possible source of depletion of the side focusing points is particle size. As the particle size increases , there is an excluded volume around the border of the channel where the particle cannot focus because it would hit the channel wall. This excluded volume reduces the size of the attraction zone, making the side focusing point even less favorable. Furthermore, the size of the particle directly affects the reciprocal theorem integral for the inertial lift force. Computing the trajectories for various particle sizes, we see that the side focusing points break down as particle size increases (Figure 5.4).
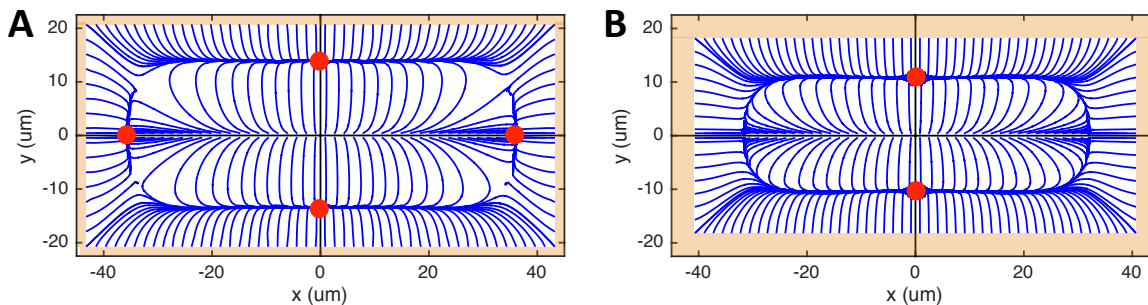
Figure 5.4: The streamlines for (A) $\alpha = 0.02$ and (B) $\alpha = 0.09$. The orange shaded area shows the excluded volume where the particle hits the wall, and the red markers show the focusing positions.

To show the breakdown of the asymptotic series for side focusing points we compare the location of the focusing manifold and the boundary $0.5W - a$, which marks the closest approach of the particle to the wall. For very small particles sizes $\alpha < 0.05$, the closest

approach of the particle lies outside of the zero contour of F_{Ly} (Figure 5.5A). This means that the particle can acheive the force free condition before it hits the wall. In contrast, for large particle sizes $\alpha \geq 0.05$, the closest approach of the particle lies inside of the zero contour of F_{Ly} (Figure 5.5A). This means that the particle can never achieve the force free condition because it will first come in contact with the wall. The critical particle size for finidng a stable focusing point is $\alpha = 0.039$.
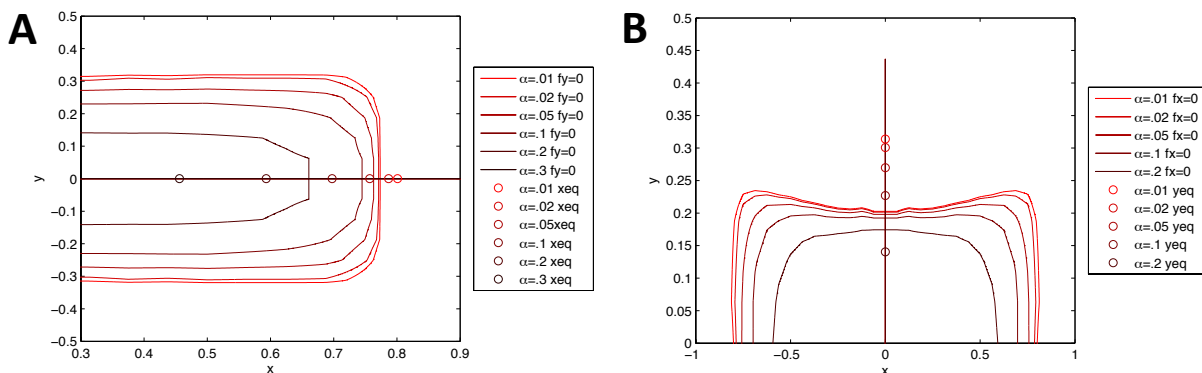
Figure 5.5: AR $= 2$. (A) We can predict the number of focusing positions by comparing the location of the equilibrium position along the x axis (xeq) with the zero contours of F_y. If xeq lies on the side of negative F_y, then xeq is a stable focusing position. Otherwise if xeq lies on the side of positive F_y, then xeq is not a stable focusing position. The critical α for finding a stable focusing position is $\alpha = 0.039$. (B) Do the same thing for yeq and F_x. The critical α for finding a stable focusing position at yeq is $\alpha = .16$

Similarly, we also observe a breakdown of the central focusing positions (Figure 5.5B). However, the critical particle size for focusing is $\alpha = 0.16$, which is close to the limit for which our model is accurate $\alpha \leq 0.2$.

How does this theory compare with experimental data? We ran experiments with $Re = 30$ and varied the particle size with diameters $d = 4.8\mu$m, 12μm, and 19μm. We measure the pdf of particle position across the width of the channel at various lengths downstream. Initially particles are distributed along the channel width with some transitory local maximums.

Downstream large particles ($\alpha = 0.13$ and $\alpha = 0.21$) are focused near $x = 0$ which corresponds to the dominant focusing positions. Small particles ($\alpha = 0.053$) show little to no focusing at 1.5cm downstream. Large particles focus to the two dominant focusing postions, while small particles show little evidence of migration (Figure 5.6).
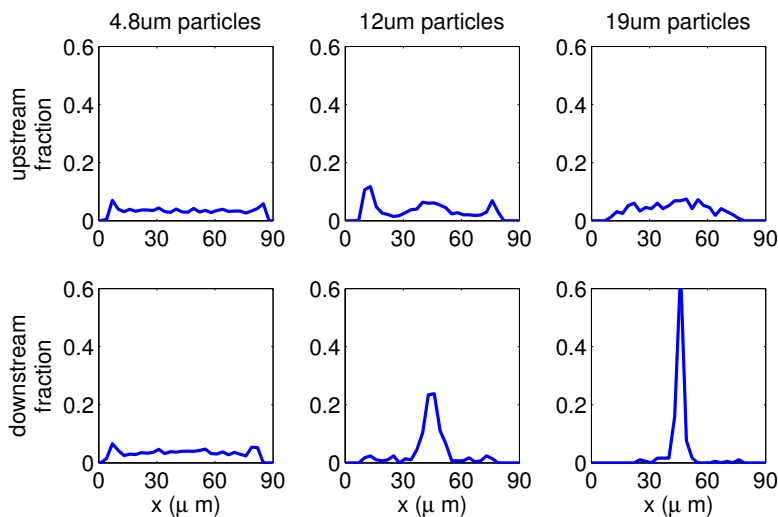
Figure 5.6: Pdf plots of experimental data shows the number of focusing positions for $Re = 30$. Small particles (4.8um) show now focusing in short channels (1.5cm), whereas larger particles (12um and 19um) show a preference for the two focusing positions in the center of the channel.

This confirms previous results that imply that large particles have two focusing points while smaller particles have four focusing points. The lack of the two side focusing points for large particles is explained by a breakdown of the asymptotic series for the lift force.

5.1.4   Further Work

We have closely examined the number of focusing positions for a rectangular channel with $AR = 2$. We have shown that the channel can have both two and four focusing positions. Furthermore we have shown that the preference for two focusing positions depends on the particle size. The side focusing point breaks down because large particles cannot occupy the predicted point because it lies too close to the channel wall.

To develop this theory further, I would like to do similar investigations for different AR. We know that for square channels ($AR = 1$), all particle sizes have four focusing positions. For each particle size, there should be a critical AR at which the particles transistion from having four focusing positions to two. Using our model, we can vary AR and α in order to make a prediction for this transistion. Furthermore, this theory should be validated experimentally.

5.2 Engineering the number of focusing positions

We have derived a hybrid asymptotic and numerical model of inertial migration. This model is an improvement over previous theories in that it is valid for larger particle sizes α and it describes how the inertial lift force changes as α changes. However, the formal derivation of the inertial lift force gives little insight into the physics of inertial focusing. Because the NSE are nonlinear and nonlocal, it is difficult to ascribe behavior to any single component. The effect of the channel walls, for example, mathematically appears in many places: (1) the images of the stresslet $\mathbf{u}_{2i}^{(0)}$ and the stokeslet $\hat{\mathbf{u}}_{2i}$, (2) the domain of integration V in the reciprocal theorem, and (3) implicitly, in the definition of the Poiseuille flow $\bar{\mathbf{u}}$. In the following section we analyze the contributions of each component of the reciprocal theorem integral for the inertial lift force.

5.2.1 Lift Force Theory

We proposed an asymptotic model [36] for computing the lift force on a solid sphere in a square channel in three dimensions. The model can be easily generalized for channels of arbitrary cross section, and in this chapter we explore the role of aspect ratio in the number of focusing positions.

We demonstrated that inertia was subdominant throughout the channel, so it is appropriate to use the regular perturbation expansion proposed by Ho & Leal [32], and unnecessary to consider the matched asymptotic expansion proposed by Schonberg & Hinch [63]. In our

model, we follow the regular perturbation expansion of Ho & Leal [32], with two exceptions: (a) we compute terms numerically in three dimensions, and (b) we calculate the next order term in the expansion for the lift force.

The regular purtubation expansion reduces the (nonlinear) Navier-Stokes equations to a pair of (linear) Stokes equations. The first, $\mathbf{u}^{(0)}$, is the velocity of a solid particle translating and rotating in the background Poiseuille flow. The second, $\hat{\mathbf{u}}$, is the velocity of a particle translating toward the channel wall. The background flow $\bar{\mathbf{u}} = \bar{u}(x, y)\mathbf{e}_z$ is the Poisuille flow for a rectangular pipe and has the following Taylor expansion around the point $\mathbf{x}_0 = (x_0, y_0)$:

$$\bar{u}(x, y) = \beta + \gamma_x(x - x_0) + \gamma_y(y - y_0) \tag{5.8}$$
$$+ \delta_{xx}(x - x_0)^2 + \delta_{xy}(x - x_0)(y - y_0) + \delta_{yy}(y - y_0)^2 + O(r^3) \,.$$

Let $\hat{\mathbf{u}}_x$ and $\hat{\mathbf{u}}_y$ be test velocities that represent a particle located at $\mathbf{x}_0$ moving with unit velocity in the direction $\mathbf{e}_x$ and $\mathbf{e}_y$, respectively. Then at the point $\mathbf{x}_0$, the lift force $\mathbf{F}_L = (F_{Lx}, F_{Ly})$ can be evaluated using the Lorentz Reciprocal theorem [44]:

$$F_{Lx}(\mathbf{x}_0) = Re_p \int_V \hat{\mathbf{u}}_x \cdot \left[\bar{\mathbf{u}} \cdot \nabla \mathbf{u}^{(0)} + \mathbf{u}^{(0)} \cdot \nabla \bar{\mathbf{u}} + \mathbf{u}^{(0)} \cdot \nabla \mathbf{u}^{(0)} \right] \, dV \,. \tag{5.9}$$

A similar formula holds for $F_{Ly}(\mathbf{x}_0)$ by replacing $\hat{\mathbf{u}}_x$ with $\hat{\mathbf{u}}_y$.

To expose the role played by particle size in determining the lift force, we expanded $\mathbf{u}$ and $\hat{\mathbf{u}}$ as a two-term series in α, the ratio of the particle radius to the channel depth. The lift force $\mathbf{F}_L$ at the point $\mathbf{x}_0$ in the channel can be expressed as a two term asymptotic expansion with coefficients $\mathbf{c}_4(\mathbf{x}_0)$ and $\mathbf{c}_5(\mathbf{x}_0)$. Specifically,

$$\mathbf{F}_L(\mathbf{x}_0) \sim \frac{\rho U^2 a^4}{H^2} \left[\mathbf{c}_4(\mathbf{x}_0) + \frac{a}{H} \mathbf{c}_5(\mathbf{x}_0) \right] \,, \tag{5.10}$$

where ρ is the fluid density, H is the channel depth, and U is the average velocity of the undisturbed flow. The coefficients $\mathbf{c}_4(\mathbf{x}_0)$ and $\mathbf{c}_5(\mathbf{x}_0)$ are dimensionless constants including both analytical and numerically computed components, and that depend on the location of the particle $\mathbf{x}_0$ and the aspect ratio of the rectangular cross-section.

5.2.2 Heuristic explanation of terms in the reciprocal theorem

In order to develop an expansion in a for the lift force, we must make an expansion of the creeping flow velocities $\mathbf{u}^{(0)}$ and $\hat{\mathbf{u}}$. These expansions take the form:

$$\mathbf{u}^{(0)} = \mathbf{u}_1^{(0)} + \mathbf{u}_2^{(0)} + \dots \quad \text{and} \quad \hat{\mathbf{u}}_k = \hat{\mathbf{u}}_{k1} + \hat{\mathbf{u}}_{k2} + \dots, \quad \text{for } k = x, y. \tag{5.11}$$

The first terms in each series are singularities that can be derived analytically. The first, $\mathbf{u}_1^{(0)} = \mathbf{u}_{x1}^{(0)} + \mathbf{u}_{y1}^{(0)}$ is the sum of two stresslets. The stresslet describes the velocity of a solid sphere in a creeping shear flow [3] and is defined as:

$$\mathbf{u}_{k1}^{(0)} = \frac{5\gamma_k(k - k_0)(z - z_0)\mathbf{r}}{2r^5} \quad \text{for } k = x, y, \tag{5.12}$$

and where $\mathbf{r} = \mathbf{x} - \mathbf{x}_0$ and $r = |\mathbf{r}|$. Recall that γ_x and γ_y are the shear terms from the Taylor expansion of the background flow $\bar{\mathbf{u}}$ in equation (5.8).

The second velocity, $\hat{\mathbf{u}}_{k1}$, is called the stokeslet and describes the motion of a solid sphere traveling at velocity $\mathbf{e_k}$,

$$\hat{\mathbf{u}}_{k1} = \frac{3}{4}\left(\frac{\mathbf{e}_k}{r} + \frac{(k - k_0)\mathbf{r}}{r^3}\right), \quad \text{for } k = x, y. \tag{5.13}$$

The second terms in the expansions are obtained by using the method of images and solving numerically. These four terms are the only terms in the expansion that contribute to the integral for the prefactor $\mathbf{c}_4 = (c_{4x}, c_{4y})$. The leads to an integral of the form:

$$c_{4k}(\mathbf{x}_0) = \frac{H^2}{\rho U_m^2 a^4}\int_V (\hat{\mathbf{u}}_{k1} + \hat{\mathbf{u}}_{k2}) \cdot \left[\bar{\mathbf{u}} \cdot \nabla(\mathbf{u}_1^{(0)} + \mathbf{u}_2^{(0)}) + (\mathbf{u}_1^{(0)} + \mathbf{u}_2^{(0)}) \cdot \nabla\bar{\mathbf{u}}\right] dV, \tag{5.14}$$

for $k = x, y$.

Now we ask: which of the terms $\hat{u}_{k1}$, $\hat{u}_{k2}$, $\mathbf{u}_1^{(0)}$ and $\mathbf{u}_2^{(0)}$ are necessary to qualitatively predict the behavior of inertial focusing? In order to answer this question, we will divide up

Terms in the reciprocal theorem	Label	Streamline dynamics
Stokeslet + dominant stresslet	$\mathbf{RT}_D^{11}$	Radiation from center
Stokeslet + sub-dominant stresslet	$\mathbf{RT}_S^{11}$	Repulsion from corners
Stokeslet + both stresslet images	$\mathbf{RT}^{12}$	Attraction to center

Table 5.1: Streamline dynamics observed in Figure 5.7 for each term in the reciprocal theorem.

the integral according to the six velocity terms above. Define

$$RT_{k\ell}^{ij}(\mathbf{x}_0) = Re_p \int_V \hat{\mathbf{u}}_{ki} \cdot \left[\bar{\mathbf{u}} \cdot \nabla \mathbf{u}_{\ell j}^{(0)} + \mathbf{u}_{\ell j}^{(0)} \cdot \nabla \bar{\mathbf{u}} \right] \, dV \,. \tag{5.15}$$

We define the vector quantity $\mathbf{RT}$ as follows:

$$\mathbf{RT}_\ell^{ij} = (RT_{x\ell}^{ij}, RT_{y\ell}^{ij}) \qquad \mathbf{RT}^{ij} = (RT_{xx}^{ij} + RT_{xy}^{ij}, RT_{yx}^{ij} + RT_{yy}^{ij}) \tag{5.16}$$

We also define the dominant and sub-dominant stresslet terms as follows:

$$\mathbf{RT}_D^{ij} = (RT_{xx}^{ij}, RT_{yy}^{ij}) \,, \qquad \mathbf{RT}_S^{ij} = (RT_{xy}^{ij}, RT_{yx}^{ij}) \,. \tag{5.17}$$

Note that lift force is the sum of all $\mathbf{RT}$ terms

$$\mathbf{F}_L(\mathbf{x}_0) = \sum_{i,j=1}^{\infty} \mathbf{RT}^{ij}(\mathbf{x}_0) \,, \tag{5.18}$$

and that the lift coefficients $\mathbf{c}_4$ and $\mathbf{c}_5$ can be written as

$$\mathbf{c}_4(\mathbf{x}_0) = \sum_{i,j=1}^{2} \mathbf{RT}^{ij}(\mathbf{x}_0) \,, \qquad \mathbf{c}_5(\mathbf{x}_0) = \sum_{i=3}^{4} \sum_{j=1}^{2} \mathbf{RT}^{ij}(\mathbf{x}_0) \,. \tag{5.19}$$

We use the results $\mathbf{RT}^{ij}$ to represent a force acting on the particle and generate streamlines using advection [36]. From these streamlines we can infer the effect of each velocity term contributes to the total lift force $\mathbf{F}_L$ (Figure 5.7, Table 5.1).

If we only consider the stokeslet and the dominant stresslet $\mathbf{RT}_D^{11}$, particles move radially out from the center of the channel, and then migrate along the walls to focus in the corners of the channel (Figure 5.7E). On the other hand, considering only the stokeslet and the
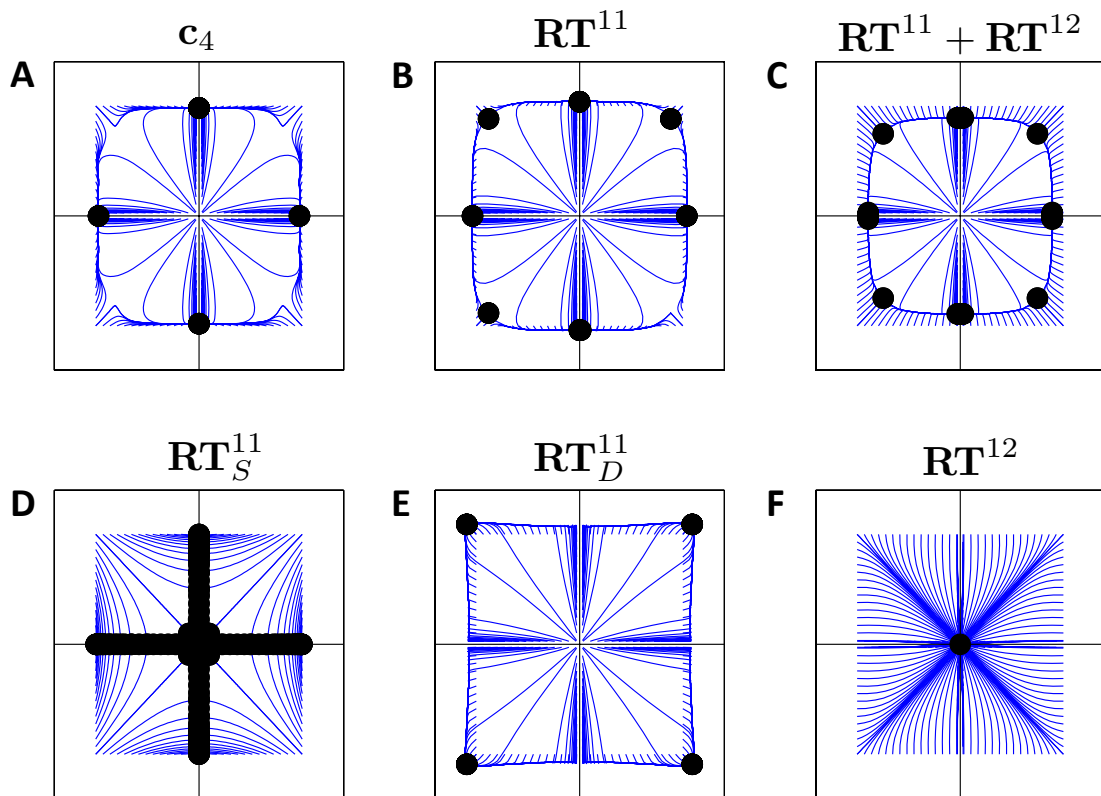
Figure 5.7: Streamlines produced by particles advected using different components of the reciprocal theorem. Solid black circles denote focusing positions. (A) full reciprocal theorem (B) stokeslet and both x- and y-shear stresslets (C) stokeslet and both stresslets and their images (D) stokeslet and x-shear stresslet (E) stokeslet and y-shear stresslet (F) stokeslets and the stresslet images.

sub-dominant stresslet $\mathbf{RT}_S^{11}$, we find that particles move away from the corners, and focus no the centerline axes of the channel (Figure 5.7D).

Combining the stokeslet and both the dominant and sub-dominant stresslet $\mathbf{RT}^{11}$, we see the same behavior as the full reciprocal theorem integral: particles move radially outward to a one dimensional manifold, and then along the manifold to focusing positions on the centerline axes of the channel (Figures 5.7B and 5.7A, respectively). However, quantitatively, the stokeslet-both-stresslets integral leads to focusing positions that are too close to the wall.

By adding in the stresslet images $\mathbf{RT}^{12}$, we adjust the focusing positions nearer the center
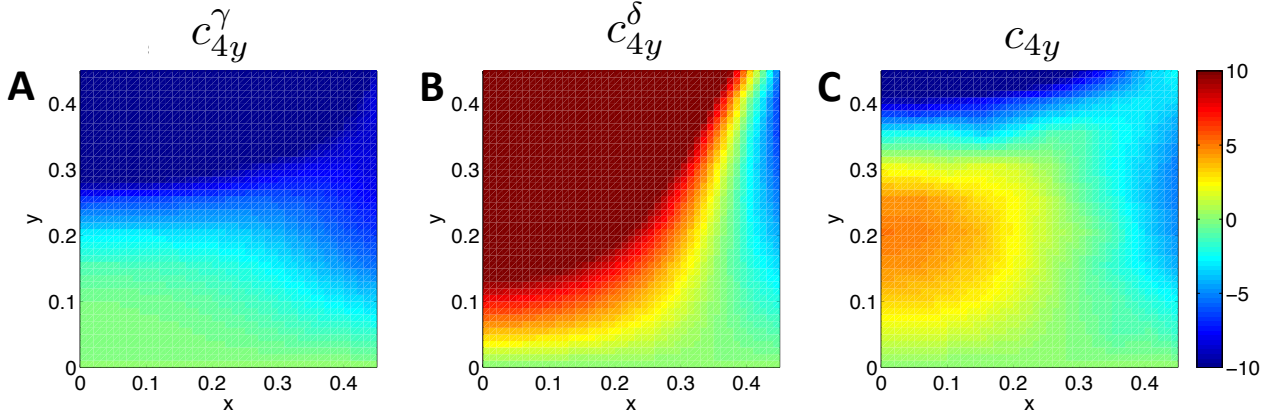
Figure 5.8: The shear and curvature contributions to c_{4y}. (A) The shear c_{4y}^{γ} pulls particles into the center of the channel, while (B) the curvature c_{4y}^{δ} pushes particles out toward the walls.

of the channel (Figure 5.7C and 5.7F). In addition, we also see that the migration along the manifold is much slower when we add in the stresslet images. We assume that further terms in the reciprocal theorem serve to set the proper location of the focusing points, doing little to alter the qualitative behavior of the dynamics.

Furthermore, we can separate out the terms of the background Poiseuille flow $\bar{\mathbf{u}}$ into its shear and curvature components:

$$\bar{\mathbf{u}}_{\gamma} = \gamma_x(x - x_0) + \gamma_y(y - y_0), \quad \text{and} \tag{5.20}$$

$$\bar{\mathbf{u}}_{\delta} = \delta_{xx}(x - x_0)^2 + \delta_{xy}(x - x_0)(y - y_0) + \delta_{yy}(y - y_0)^2. \tag{5.21}$$

We can further break down the reciprocal theorem, equation (5.15), into the shear and curvature components:

$$^{\kappa}RT_{k\ell}^{ij}(\mathbf{x}_0) = Re_p \int_V \hat{\mathbf{u}}_{ki} \cdot \left[\bar{\mathbf{u}}_{\kappa} \cdot \nabla \mathbf{u}_{\ell j}^{(0)} + \mathbf{u}_{\ell j}^{(0)} \cdot \nabla \bar{\mathbf{u}}_{\kappa} \right] dV, \qquad \text{for } \kappa = \gamma, \delta. \tag{5.22}$$

From this we can determine how the shear and curvature of the background flow $(\bar{\mathbf{u}}_{\gamma}, \bar{\mathbf{u}}_{\delta})$ contribute to the lift coefficients $\mathbf{c}_4$. Define:

$$\mathbf{c}_4^{\kappa}(\mathbf{x}_0) = \sum_{i,j=1}^{2} {}^{\kappa}\mathbf{RT}^{ij}(\mathbf{x}_0), \qquad \text{for } \kappa = \gamma, \delta. \tag{5.23}$$

The shear c^{γ}_{4y} pulls particles into the center of the channel, while the curvature c^{δ}_{4y} pushes particles out toward the wall in the $y-$direction (Figure 5.8).

5.2.3 Further work

We have shown that the outward radial part of the inertial lift force is derived from the curvature term $\mathbf{c}^{\delta}_4$. Similarly, the repullsion from the wall appears in the shear term $\mathbf{c}^{\gamma}_4$. The stresslet terms can contribute to both repulsion from and attraction to the walls, whereas the stresslet image only contributes to the repulsion from the wall. To qualitatively predict the behavior of the inertial lift force, it is sufficient to consider only the stokeslet, stresslet, and stresslet image terms in the reciprocal theorem.

We propose that the most direct way to engineer a channel with a given number of focusing positions is to balance the shear and curvature terms of the Poiseuille flow $\bar{\mathbf{u}}$. In order to proceed, we need to explicitly reveal the relationship between the shear term and the contribution to the inertial lift force. Then the channel design might be represented as an inverse problem: given the shear γ and the curvature δ terms on a small region U, what is the domain $\Omega \supseteq U$ such that the poiseuille flow $\bar{\mathbf{u}}$ on Ω matches the shear and curvature terms on U. A few interesting cases to explore initially would be rectangular channels with $AR > 1$, and the channel with a T-shaped cross-section.

APPENDIX A

Appendix: Inertial migration

A.1   Notation

Throughout the main paper, we need to change the scaling of variables in order to capture the dynamics either near the particle or near the channel walls. In this Appendix we create a reference for the notation for three scalings: dimensional scalings, dimensionless inner variables, and dimensionless outer variables. To be consistent with previous literature, we denote the dimensionless inner variables with lower case roman letters, and the dimensionless outer variables with upper case roman letters. We use primes to distinguish dimensional variables. A reference is presented in table A.1.

We must draw attention to the notation for the particle velocity and particle angular velocity. Since both the inner and outer variables are scaled by the same velocity, αU_m, the scaled particle velocity is the same in both cases. We choose to represent the dimensionless particle velocity by $\mathbf{U}_p$ to be consistent with notation in previous studies [63, 32].

However, the scaling for the particle angular velocity differs between the inner and outer coordinates. We continue to use $\boldsymbol{\Omega}_p$ in both the inner and outer variables, despite this abuse of notation. We keep $\boldsymbol{\Omega}_p$ in order to be consistent with previous studies [63, 32]. We feel justified in our decision since $\boldsymbol{\Omega}_p$ does not arise in the computation of our asymptotic model, so the reader wishing to apply our results need not worry over the discrepancy. Nevertheless, we remind the reader that the particle angular velocity for the inner variables satisfies $\omega_p = \alpha \boldsymbol{\Omega}_p$.

89

Variables	Dimensional	Inner	Outer
Distance	$\mathbf{r}' = (x', y', z')$	$\mathbf{r} = (x, y, z)$	$\mathbf{R} = (X, Y, Z)$
Velocity	$\mathbf{u}'$	$\mathbf{u}$	$\mathbf{U}$
Pressure	p'	p	P
Particle location	(x'_0, y'_0)	(x_0, y_0)	(X_0, Y_0)
Particle velocity	$\mathbf{U}'_p$	$\mathbf{U}_p$	$\mathbf{U}_p$
Particle angular velocity	$\mathbf{\Omega}'_p$	$\mathbf{\Omega}_p$	$\mathbf{\Omega}_p$
Poiseuille flow	$\bar{\mathbf{u}}'$	$\bar{\mathbf{u}}$	$\bar{\mathbf{U}}$
Asymptotic expansion of velocity	-	$\mathbf{u}^{(0)}$	$\mathbf{U}^{(0)}$
Reference velocity	-	$\hat{\mathbf{u}}$	$\hat{\mathbf{U}}$
Conversion from Dimensional variables	$\mathbf{r}'$	$\mathbf{r} = \mathbf{r}'/a$	$\mathbf{R} = \mathbf{r}'/\ell$
Conversion from Inner variables	$\mathbf{r}' = a\mathbf{r}$	$\mathbf{r}$	$\mathbf{R} = \alpha\mathbf{r}$
Conversion from Outer variables	$\mathbf{r}' = \ell\mathbf{R}$	$\mathbf{r} = \mathbf{R}/\alpha$	$\mathbf{R}$

Table A.1: Comparison of dimensional and dimensionless scalings of the variables.

A.2 Accuracy of the numerical model

A.2.1 Accuracy of the domain size

We subjected the FEM discretization of (2.4) to convergence tests based on varying the size of the numerical domain and on changing the mesh size. Maximum element size was decreased, and the length of the domain was increased until the computed drag and lift forces had converged to within 0.5%.

To test the length of the domain, we varied the variable L_z, defined so that the channel domain became $\frac{\ell}{a} \times \frac{\ell}{a} \times L_z\frac{\ell}{a}$. We solved the Navier-Stokes equations where the particle surface and channel walls have no slip boundary conditions. The particle is assumed to have no velocity or angular velocity. Comsol's standard meshing algorithms are used, and the particle size is chosen to be $\alpha = 0.11$.

We see that the drag force F quickly converges to its final value, at about $L_z = 2 - 3$
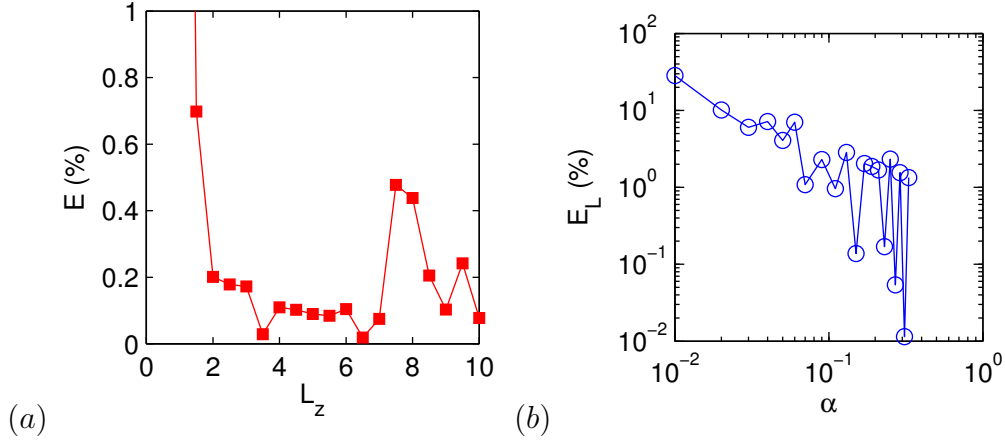
Figure A.1: (a) The relative error E of the drag force is less than 1% for $L_z > 1$, and in particular for our choice of $L_z = 5$ the relative error is less than 0.5%. (b) The relative lift force error E_L from solving the Navier-Stokes equations increases exponentially as α decreases.

(figure A.1a). Averaging the data for $L_z >= 3$ to obtain a force estimate $\bar{F}$, we also present a relative error as $E = 100(F - \bar{F})/\bar{F}$. A small fluctuating error persists as L_z is increased up to $L_z = 10$. This error probably reflects mesh noise, rather than geometry. Similar data is seen when simulations are performed on different grades of mesh.

A.2.2 Accuracy of the particle size

We also discuss the range of α that were computed in this paper. The upper range of α is limited by the position of the particle relative to the walls and to the equilibrium positions. Since the lift force f_L is not only a function of α, but also of x_0 and y_0, the location of the particle in the channel. For any given α, there are four coordinates (x_0, y_0) where the lift force is zero, we call these points equilibrium positions. In the first part of our paper, we constrain our locations to those on the positive y-axis, that is coordinates of the form $(0, y_0)$, for $y_0 > 0$. The equilibrium position $(0, y_0^*)$, which is a function of α, divides this domain into two sections: (i) domain between the equilibrium position and the center of the channel, and (ii) the domain between the equilibrium position and the wall. We must be careful in

91

these regions, when we are examining the scaling law for fixed y_0 and varied α, to choose α so that f_L remains positive and does not pass through zero. The same principal extends to the choice of α for all locations throughout the channel.

The lower range of α however, is limited by the accuracy of the root finder in the Navier-Stokes solver. As discussed in §2.2, the values of U_p and $\mathbf{\Omega}_p$ are chosen so that the particle is drag free and force free. Therefore, the drag force F_D can be used as a measure of the precision of the numerical solver. We define the relative lift force error as $E_L = 100(F_D/f_L)$. The relative lift force error as a function of α for an particle located at $(x_0 = 0, y_0 = 0.15/\alpha)$ and with $Re = 1$ increases exponentially as α decreases to zero (figure A.1b). We limit $\alpha >= 0.03$, or relative error $E_L < 10\%$.

We do not strive to test smaller particles sizes α because the theoretical results of [63] and [2] are generally accepted to be true for asymptotically small particles. Our goal in this paper is to produce theory for particles at the sizes used in experimental systems. Smaller values of α are not used in experiments, because lift forces become too weak to compete with other forces, such as Brownian motion.

A.2.3   Accuracy of the Naver-Stokes solver

To further account for artifacts associated e.g. with regularization of the convective (inertial) terms in (2.4), we also solved a model problem of computing the drag force on a sphere moving through a quiescent fluid, for which a considerable body of well-validated experimental and numerical data exists [76].

Let a be the particle radius, $U\mathbf{e_z}$ be the flow velocity, ρ the fluid density, and ν be the kinematic viscosity of the fluid surrounding a particle. The Reynolds number in this scenario is: $Re_p = Ua/\nu$. The drag F_D on the sphere is the force in the $z-$direction. We define the drag coefficient to be:

$$C_D = \frac{F_D}{\rho U^2 a^2} \ .$$

In our simulation, we consider the domain of fluid to be a cube of length $50a$, with the
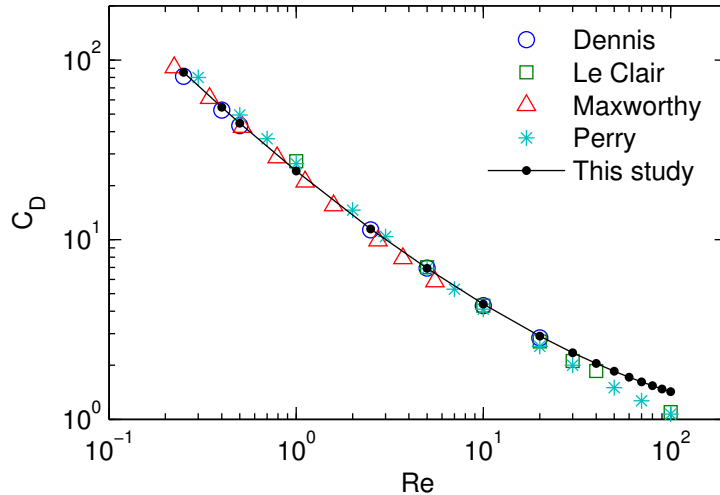
Figure A.2: Our calculation of the drag coefficient, C_D, for a sphere in a uniform flow (black dot) compares well to numerical data (Dennis - blue circles, Le Clair - green squares) and experimental data (Maxworthy - red triangles, Perry - cyan *) across a large range of Reynolds numbers, Re.

particle of radius a centered at the origin. We choose the minimum element size at the sphere surface to be comparable to those of the simulations described in §2.2.

We compute the drag force using the Lagrange multipliers used within the FEM to enforce the velocity boundary condition on the particle surface. We consider Reynolds numbers between $Re_p = 0.1$ and $Re_p = 100$, by varying the fluid velocity U. Our computation of the drag coefficient C_D compares favorably to those of various experimental and numerical studies (figure A.2b). In particular: [52] accurately measures the drag on a sphere in experiments, using a container diameter which is 700 times the sphere diameter. Maxworthy estimates his experimental error to be better than 2%. We also include experimental data catalogued in [56] for larger Reynolds numbers and numerical studies by [46] and [21].

A.3 Analytic velocities

This appendix contains the full equations for the velocities, $\mathbf{u}_1^{(0)}$ and $\hat{\mathbf{u}}_1$, described in §2.4. Since the odd terms of the expansion of $\mathbf{u}^{(0)}$ are exact on the particle, they can be computed analytically using Lamb's solution for the flow external to a sphere [44, 32]. The multipole expansion of $\mathbf{u}_1^{(0)}$ takes the form:

$$\mathbf{u}_1^{(0)} = \sum_{n=0}^{\infty} \frac{1}{r^{n+1}} \mathbf{f}_n^1 \left(\frac{x - x_0}{r}, \frac{y - y_0}{r}, \frac{z}{r} \right). \tag{A.1}$$

The components of each $\mathbf{f}_n^1$ are defined as follows:

$$\mathbf{f}_0^1 \left(\frac{x}{r}, \frac{y}{r}, \frac{z}{r} \right) = -\frac{(A_1 + I_1)}{2} \left(\mathbf{e}_z + \frac{z\mathbf{r}}{r^2} \right), \tag{A.2}$$

$$\mathbf{f}_1^1 \left(\frac{x}{r}, \frac{y}{r}, \frac{z}{r} \right) = \frac{-5\gamma_y}{2} \frac{yz\mathbf{r}}{r^3} + C_1 \left(\frac{z\mathbf{e}_y}{r} - \frac{y\mathbf{e}_z}{r} \right) + \frac{-5\gamma_x}{2} \frac{xz\mathbf{r}}{r^3} + K_1 \left(\frac{z\mathbf{e}_x}{r} - \frac{x\mathbf{e}_z}{r} \right), \tag{A.3}$$

$$\mathbf{f}_2^1 \left(\frac{x}{r}, \frac{y}{r}, \frac{z}{r} \right) = \frac{\delta_{xx}}{8} \left(\frac{5}{3}\mathbf{e}_z - 3\frac{x^2}{r^2}\mathbf{e}_z + 10\frac{xz}{r^2}\mathbf{e}_x + 5\frac{z\mathbf{r}}{r^2} - 35\frac{x^2 z\mathbf{r}}{r^4} \right) \tag{A.4}$$

$$+ \frac{\delta_{xy}}{8} \left(-3\frac{xy}{r^2}\mathbf{e}_z + 5\frac{yz}{r^2}\mathbf{e}_x + 5\frac{xz}{r^2}\mathbf{e}_y - 35\frac{xyz\mathbf{r}}{r^4} \right)$$

$$+ \frac{\delta_{yy}}{8} \left(\frac{5}{3}\mathbf{e}_z - 3\frac{y^2}{r^2}\mathbf{e}_z + 10\frac{yz}{r^2}\mathbf{e}_y - 35\frac{y^2 z\mathbf{r}}{r^4} \right),$$

$$\mathbf{f}_3^1 \left(\frac{x}{r}, \frac{y}{r}, \frac{z}{r} \right) = -\frac{\gamma_y}{2} \left(\frac{z\mathbf{e}_y}{r} + \frac{y\mathbf{e}_z}{r} - \frac{5yz\mathbf{r}}{r^3} \right) - \frac{\gamma_x}{2} \left(\frac{z\mathbf{e}_x}{r} + \frac{x\mathbf{e}_z}{r} - \frac{5xz\mathbf{r}}{r^3} \right), \tag{A.5}$$

$$\mathbf{f}_4^1 \left(\frac{x}{r}, \frac{y}{r}, \frac{z}{r} \right) = \frac{\delta_{xx}}{8} \left(\mathbf{e}_z - 5\frac{x^2}{r^2}\mathbf{e}_z - 10\frac{xz}{r^2}\mathbf{e}_x - 5\frac{z\mathbf{r}}{r^2} + 35\frac{x^2 z\mathbf{r}}{r^4} \right) \tag{A.6}$$

$$+ \frac{\delta_{xy}}{8} \left(-5\frac{yz}{r^2}\mathbf{e}_x - 5\frac{xz}{r^2}\mathbf{e}_y - 5\frac{xy}{r^2}\mathbf{e}_z + 35\frac{xyz\mathbf{r}}{r^4} \right)$$

$$+ \frac{\delta_{yy}}{8} \left(\mathbf{e}_z - 5\frac{y^2}{r^2}\mathbf{e}_z - 10\frac{yz}{r^2}\mathbf{e}_y - 5\frac{z\mathbf{r}}{r^2} + 35\frac{y^2 z\mathbf{r}}{r^4} \right),$$

and $\mathbf{f}_n^1 = \mathbf{0}$ for $n \geq 5$. Here the constants A_1, C_1, I_1, and K_1 are all of order $O(\alpha^3)$, and so do not participate in determining the force on the particle at the order computed in this study. Note that when when we are on the symmetry plane $x = 0$, then also $\gamma_x = 0$, and likewise with y and γ_y.

We can also use the Lamb's solution to calculate the odd terms in the expansion of $\hat{\mathbf{u}}$. In particular, we represent $\hat{\mathbf{u}}_1$ in the following multipole expansion:

$$\hat{\mathbf{u}}_1 = \sum_{n=0}^{\infty} \frac{1}{r^{n+1}} \mathbf{g}_n^1 \left(\frac{x - x_0}{r}, \frac{y - y_0}{r}, \frac{z}{r} \right). \tag{A.7}$$

The full analytic solutions for the $\mathbf{g}_n^1$ are below:

$$\mathbf{g}_0^1 \left(\frac{x}{r}, \frac{y}{r}, \frac{z}{r} \right) = \frac{3}{4} \left(\mathbf{e}_y + \frac{y\mathbf{r}}{r^2} \right), \tag{A.8}$$

$$\mathbf{g}_2^1 \left(\frac{x}{r}, \frac{y}{r}, \frac{z}{r} \right) = \frac{1}{4} \left(\mathbf{e}_y - \frac{3y\mathbf{r}}{r^2} \right), \tag{A.9}$$

and $\mathbf{g}_n^1 = \mathbf{0}$ for $n = 1$, and $n \geq 3$.

A.4 Determining the reciprocal theorem integrands

In this appendix, we rationalize the choice of integrands for the reciprocal theorem (2.18) in §2.4.3 and §2.4.4. For each domain, we scale by the characteristic length, and then sort terms by magnitude in α. Finally, we choose terms of the velocities that combine to give the desired power of α.

A.4.1 Inner integral

For the inner integral, we continue to scale lengths by the particle radius a, and collect terms by order of magnitude in α. For the $O(a^4)$ contribution, we need to choose combinations of $\mathbf{u}_i^{(0)}$, $\hat{\mathbf{u}}_i$, and $\bar{\mathbf{u}}$ that combine to give $O(\alpha^2)$ in the integrand of (2.18). Similarly, for $O(a^5)$, terms need to combine to give $O(\alpha^3)$ in the integrand.

The leading terms in magnitude α of the $\mathbf{u}_i^{(0)}$ are shown below.

$$\mathbf{u}_1^{(0)} \sim \alpha \left(\frac{1}{r^2} \mathbf{f}_1^1 + \frac{1}{r^4} \mathbf{f}_3^1 \right) + \alpha^2 \left(\frac{1}{r^3} \mathbf{f}_2^1 + \frac{1}{r^5} \mathbf{f}_4^1 \right) + O(\alpha^4),$$

$$\mathbf{u}_2^{(0)} \sim \alpha^3 \mathcal{SI} \left[\frac{1}{r^2} \mathbf{f}_1^1 \right] + O(\alpha^4),$$

(A.10)

and all higher order $\mathbf{u}_i^{(0)}$ are $O(\alpha^4)$ or smaller. We define $\mathbf{v} = \mathcal{SI}[\mathbf{u}]$ as the image of the function $\mathbf{u}$, that is $\mathbf{v}$ solves the Stokes equations with $-\mathbf{u}$ as the boundary condition on the walls. The leading terms in magnitude α of the $\hat{\mathbf{u}}_i$ are shown below.

$$\hat{\mathbf{u}}_1 \sim \frac{1}{r} \mathbf{g}_0^1 + \frac{1}{r^3} \mathbf{g}_2^1 \;,$$

$$\hat{\mathbf{u}}_2 \sim \alpha \mathcal{SI} \left[\frac{1}{r} \mathbf{g}_0^1 \right] + O(\alpha^3) \;,$$

(A.11)

$$\hat{\mathbf{u}}_3 \sim \alpha \left(\frac{1}{r} \mathbf{g}_0^3 + \frac{1}{r^3} \mathbf{g}_2^3 \right),$$

and higher order $\hat{\mathbf{u}}_i$ are $O(\alpha^2)$ or smaller. The leading terms in magnitude α of $\bar{\mathbf{u}}$ are:

$$\bar{\mathbf{u}} \sim [\alpha \gamma r + \alpha^2 \delta r^2 + O(\alpha)] \mathbf{e_z} \;.$$

(A.12)

Recall that the inner integral has the α expansion:

$$f_{L_1} = \rho U_m^2 a^2 (h_4 \alpha^2 + h_5 \alpha^5 + \dots) \;.$$

(A.13)

It is evident that only $\mathbf{u}_1^{(0)}$, $\hat{\mathbf{u}}_1$, and the shear term of $\bar{\mathbf{u}}$ (call it $\bar{\mathbf{u}}_\gamma$) contribute to the $O(a^4)$ term of the inner integral, that is:

$$h_4 = \int_{\mathbb{R}^3} \hat{\mathbf{u}}_1 \cdot (\bar{\mathbf{u}}_\gamma \cdot \nabla \mathbf{u}_1^{(0)} + \mathbf{u}_1^{(0)} \cdot \nabla \bar{\mathbf{u}}_\gamma) \, \mathrm{dv}.$$

(A.14)

Whereas $\mathbf{u}_1^{(0)}$, $\hat{\mathbf{u}}_1$, $\hat{\mathbf{u}}_2$, $\hat{\mathbf{u}}_3$, and both the shear and curvature terms of $\bar{\mathbf{u}}$ (call them $\bar{\mathbf{u}}_\gamma$ and $\bar{\mathbf{u}}_\delta$ respectively), contribute to the $O(a^5)$ term.

$$h_5 = \int_{\mathbb{R}^3} (\hat{\mathbf{u}}_1 + \hat{\mathbf{u}}_2 + \hat{\mathbf{u}}_3) \cdot \left[(\bar{\mathbf{u}}_\gamma + \bar{\mathbf{u}}_\delta) \cdot \nabla \mathbf{u}_1^{(0)} + \mathbf{u}_1^{(0)} \cdot \nabla (\bar{\mathbf{u}}_\gamma + \bar{\mathbf{u}}_\delta) \right] \, \mathrm{dv}.$$

(A.15)

These integrals are evaluated in §2.4.3.

A.4.2 Outer integral

The outer integral is expressed in terms of $\mathbf{R} = \alpha \mathbf{r}$. We arrange our functions in order of magnitude in α as shown below. For the $O(a^4)$ term in the outer integral, we need to collect terms of $\mathbf{U}_i^{(0)}$, $\hat{\mathbf{U}}_i$, and $\bar{\mathbf{U}}$ which combine to give $O(\alpha^4)$ in the integrand of (2.18). For the $O(a^5)$ term, we need an $O(\alpha^5)$ integrand in (2.18).

The leading terms in magnitude α of the $\mathbf{U}_i^{(0)}$ are:

$$
\begin{aligned}
\mathbf{U}_1^{(0)} &\sim \alpha^3 \left(\frac{1}{R^2} \mathbf{f}_1^1 + \frac{1}{R^4} \mathbf{f}_3^1 \right) + O(\alpha^4) \,, \\
\mathbf{U}_2^{(0)} &\sim \alpha^3 \mathcal{SI} \left[\frac{1}{R^2} \mathbf{f}_1^1 \right] + O(\alpha^4) \,,
\end{aligned}
\tag{A.16}
$$

and $\mathbf{U}_3^{(0)}$ and $\mathbf{U}_4^{(0)}$ are $O(\alpha^4)$. The leading terms in magnitude α of the $\hat{\mathbf{U}}_i$ are:

$$
\begin{aligned}
\hat{\mathbf{U}}_1 &\sim \alpha \frac{1}{R} \mathbf{g}_0^1 + \alpha^3 \frac{1}{R^3} \mathbf{g}_2^1 \,, \\
\hat{\mathbf{U}}_2 &\sim \alpha \mathcal{SI} \left[\frac{1}{R} \mathbf{g}_0^1 \right] + O(\alpha^3) \,, \\
\hat{\mathbf{U}}_3 &\sim \alpha^2 \frac{1}{R} \mathbf{g}_0^3 + \alpha^4 \frac{1}{R^3} \mathbf{g}_2^3 + O(\alpha^4) \,, \\
\hat{\mathbf{U}}_4 &\sim \alpha^2 \mathcal{SI} \left[\frac{1}{R} \mathbf{g}_0^3 \right] + O(\alpha^4) \,,
\end{aligned}
\tag{A.17}
$$

while all the terms of $\bar{\mathbf{U}}$ are $O(1)$. Recall that the outer integral has the α expansion:

$$
f_{L_2} = \rho U_m^2 \ell^2 (k_4 \alpha^4 + k_5 \alpha^5 + \dots) \,.
\tag{A.18}
$$

Only $\mathbf{U}_1^{(0)}$, $\mathbf{U}_2^{(0)}$, $\hat{\mathbf{U}}_1$, $\hat{\mathbf{U}}_2$, and $\bar{\mathbf{U}}$ contribute to the $O(a^4)$ term in the outer integral, namely:

$$
k_4 = \int_{V_C} (\hat{\mathbf{U}}_1 + \hat{\mathbf{U}}_2) \cdot \left[\bar{\mathbf{U}} \cdot \nabla (\mathbf{U}_1^{(0)} + \mathbf{U}_2^{(0)}) + (\mathbf{U}_1^{(0)} + \mathbf{U}_2^{(0)}) \cdot \nabla \bar{\mathbf{U}} \right] \mathrm{d}v.
\tag{A.19}
$$

Whereas $\mathbf{U}_1^{(0)}$, $\mathbf{U}_2^{(0)}$, $\hat{\mathbf{U}}_3$, $\hat{\mathbf{U}}_4$, and $\bar{\mathbf{U}}$ contribute to the $O(a^5)$ term:

$$
k_5 = \int_{V_C} (\hat{\mathbf{U}}_3 + \hat{\mathbf{U}}_4) \cdot \left[\bar{\mathbf{U}} \cdot \nabla (\mathbf{U}_1^{(0)} + \mathbf{U}_2^{(0)}) + (\mathbf{U}_1^{(0)} + \mathbf{U}_2^{(0)}) \cdot \nabla \bar{\mathbf{U}} \right] \mathrm{d}v.
\tag{A.20}
$$

These integrals are evaluated in §2.4.4.

APPENDIX B

Appendix: Dynamical formation

B.1 Validating the numerical solver against data

To test the accuracy of our numerical solver, we compare to experimental measurements of the drag coefficient of a sphere in a square channel. Chow *et al.* observed the drag coefficient of a sphere whose diameter d is very close to the width W of a square channel [11]. For this comparision, we use their measurements for the size ratio $d/W = 0.886 \pm 0.008$. The Reynolds number of the flow was defined by $Re = UW/\nu$, where U is the average fluid velocity in an empty channel and ν is the kinematic viscosity of water.

Our numerical solver modeled a square channel with lengths scaled by the channel width W. That is, the square channel had dimensions $1 \times 1 \times 6$, and the particle had radius $a = 0.443$. We used Comsol Multiphysics (Los Angles, CA) to solve the PDE with variable Reynolds numbers. The particle velocity U_p was chosen arbitrarily to be $U_P = .75U$. We measured the drag force F_D on the particle using Lagrange multipliers (expand). Then the drag coefficient was computed by:

$$C_D = \frac{2F_D}{\pi a^2 (U_p - U)^2}.$$ (B.1)

The results from our numerical solver compare well with the data from Chow *et al.* [11], especially for $Re \leq 300$ (Figure B.1). The range of Reynolds numbers from experiments is $30 \leq Re \leq 110$, which is well within the numerical range of accuracy.
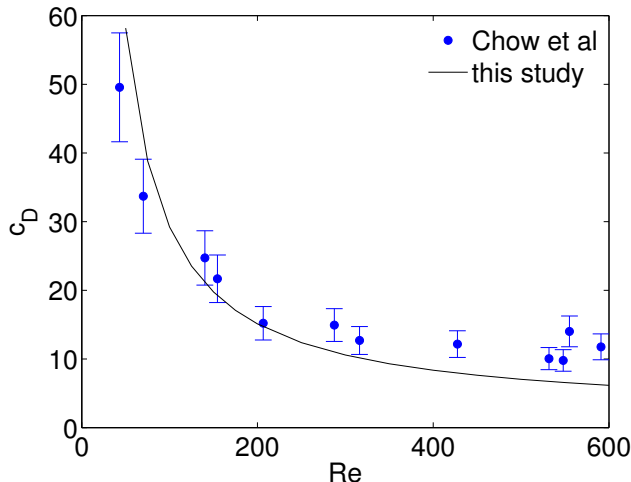
Figure B.1: Drag coefficient dependence on Reynolds number. The results from our numerical solver compare well with the data from Chow *et al.* [11]

B.2 Experimental methods for one-dimensional microfluidic crystal

We use the same raw data as collected from Kahkeshani *et al.* [40]. (below copied from that paper) The experimental observations have been made in a dual-inlet polydimethylsiloxane (PDMS) microchannel bonded to a glass slide produced according to standard soft lithography protocols [25]. The dual-inlet channel is utilized in order to self-assemble particles predominantly into one train in order to limit hydrodynamic interactions between particles to a single train. Dimensions of the channel in the axial (z or flow direction), lateral (y) and transverse (x) directions are 3 cm, 35μm and 60μm respectively. A dilute suspension of polystyrene spherical particles with diameter 12μm ($\rho_p = 1.05gcm^3$) dispersed in a suspending fluid composed of deionized water, 0.002 weight per volume (w/v) triton X-100 and 0.1 v/v glycerol is pumped into the channel with a controlled flow rate utilizing a syringe pump from one inlet, accompanied by pumping fluid without particles at an equal flow rate from the second inlet. The volume fraction of particles in the suspension is $\phi = 0.004$. The flow rate ranges from 85.5 to 342μL/min, leading to finite inertia at $Re = 30 - 120$ inside the channel. Lowering the flow rate below 85.5μL/min does not generate sufficient inertia

99

for a steady-state inter-particle spacing. Increasing the flow rate above 342μL/min leads to experimental errors such as delamination of the PDMS from the glass slide, leakage at inlets and alteration of the channel size due to high flow-induced deformation in PDMS microchannels [20]. The channel configuration allows formation of particle trains at two inertial equilibrium points close to the walls in the Y direction for particles with radius $a = 6\mu$m such that infusing the suspension from one inlet mainly generates a single train close to one wall. The axial distance between two adjacent particles has been computed from recorded snapshots captured using high-speed imaging (Phantom V710). The inter-particle spacing in multiple sections along the channel has been measured and the values corresponding to the farthest region from the entrance, spanning the last 500μm section of the channel, have been reported in order to achieve a steady-state spacing.

We developed an image analysis algorithm to measure the particle locations. As in Hood *et al.* [35], we use template matching to align a template consisting of a single 88 pixel image of a particle with the current frame. The template matching process gives a single correlation value for every pixel in the image, representing how closely the template matches the real image if centered at that pixel. We then use cubic polynomials to interpolate the correlation data and to find, with sub-pixel precision, each particle location.

References

[1] D. J. Aldous. Deterministic and stochastic models for coalescence (aggregation and coagulation): a review of the mean-field theory for probabilists. *Bernoulli*, pages 3–48, 1999.

[2] E. S. Asmolov. The inertial lift on a spherical particle in a plane poiseuille flow at large channel reynolds number. *Journal of Fluid Mechanics*, 381:63–87, 1 1999.

[3] G. K. Batchelor. *An Introduction to Fluid Dynamics*. Cambridge University Press, 1967.

[4] J. Blake. A note on the image system for a stokeslet in a no-slip boundary. In *Mathematical Proceedings of the Cambridge Philosophical Society*, volume 70, pages 303–310. Cambridge Univ Press, 1971.

[5] J. Blake and A. Chwang. Fundamental singularities of viscous flow. *Journal of Engineering Mathematics*, 8(1):23–29, 1974.

[6] J. H. Bramble. The lagrange multiplier method for dirichlets problem. *Mathematics of Computation*, 37(155):1–11, 1981.

[7] F. P. Bretherton. The motion of rigid particles in a shear flow at low reynolds number. *Journal of Fluid Mechanics*, 14:284–304, 9 1962.

[8] Y.-S. Choi and S.-J. Lee. Holographic analysis of three-dimensional inertial migration of spherical particles in micro-scale pipe flow. *Microfluidics and Nanofluidics*, 9(4-5):819–829, 2010.

[9] Y.-S. Choi, K.-W. Seo, and S.-J. Lee. Lateral and cross-lateral focusing of spherical particles in a square microchannel. *Lab on a chip*, 11(3):460–465, 2011.

[10] Y.-S. Choi, K.-W. Seo, M.-H. Sohn, and S.-J. Lee. Advances in digital holographic micro-ptv for analyzing microscale flows. *Optics and Lasers in Engineering*, 50(1):39–45, 2012.

[11] L. Chow, J. Leland, J. Beam, and E. Mahefkey. The drag coefficient of a sphere in a square channel. *Journal of fluids engineering*, 111(2):229–230, 1989.

[12] B. Chun and A. Ladd. Inertial migration of neutrally buoyant particles in a square duct: An investigation of multiple equilibrium positions. *Physics of Fluids (1994-present)*, 18(3):031704, 2006.

[13] A. J. Chung, D. R. Gossett, and D. Di Carlo. Three dimensional, sheathless, and high-throughput microparticle inertial focusing through geometry-induced secondary flows. *Small*, 9(5):685–690, 2013.

[14] A. T. Ciftlik, M. Ettori, and M. A. M. Gijs. High throughput-per-footprint inertial focusing. *Small*, 9(16):2764–2773, 2013.

[15] R. Cortez. The method of regularized stokeslets. *SIAM Journal on Scientific Computing*, 23(4):1204–1225, 2001.

[16] R. Cortez, L. Fauci, and A. Medovikov. The method of regularized stokeslets in three dimensions: analysis, validation, and application to helical swimming. *Physics of Fluids (1994-present)*, 17(3):031504, 2005.

[17] R. Cox and S. Hsu. The lateral migration of solid particles in a laminar flow near a plane. *International Journal of Multiphase Flow*, 3(3):201 – 222, 1977.

[18] R. G. Cox and H. Brenner. The lateral migration of solid particles in poiseuille flow – i theory. *Chemical Engineering Science*, 23(2), 1968.

[19] F. Da Cunha and E. Hinch. Shear-induced dispersion in a dilute suspension of rough spheres. *Journal of Fluid Mechanics*, 309:211–223, 1996.

[20] D. Dendukuri, S. S. Gu, D. C. Pregibon, T. A. Hatton, and P. S. Doyle. Stop-flow lithography in a microfluidic device. *Lab on a Chip*, 7(7):818–828, 2007.

[21] S. Dennis and J. Walker. Calculation of the steady flow past a sphere at low and moderate reynolds numbers. *Journal of Fluid Mechanics*, 48(04):771–789, 1971.

[22] D. Di Carlo. Inertial microfluidics. *Lab on a Chip*, 9(21):3038–3046, 2009.

[23] D. Di Carlo, J. F. Edd, K. J. Humphry, H. A. Stone, and M. Toner. Particle segregation and dynamics in confined flows. *Physical Review Letters*, 102(9):094503+, Mar. 2009.

[24] D. Di Carlo, D. Irimia, R. G. Tompkins, and M. Toner. Continuous inertial focusing, ordering, and separation of particles in microchannels. *Proceedings of the National Academy of Sciences*, 104(48):18892–18897, 2007.

[25] D. C. Duffy, J. C. McDonald, O. J. A. Schueller, and G. M. Whitesides. Rapid prototyping of microfluidic systems in poly(dimethylsiloxane). *Analytical Chemistry*, 70(23):4974–4984, 1998. PMID: 21644679.

[26] J. F. Edd, D. Di Carlo, K. J. Humphry, S. Köster, D. Irimia, D. A. Weitz, and M. Toner. Controlled encapsulation of single-cells into monodisperse picolitre drops. *Lab on a Chip*, 8(8):1262–1264, 2008.

[27] A. Golovin. The solution of the coagulation equation for cloud droplets in a rising air current. *Izv. Geophys. Ser*, 5:482–487, 1963.

[28] D. R. Gossett, H. T. K. Tse, J. S. Dudani, K. Goda, T. A. Woods, S. W. Graves, and D. Di Carlo. Inertial manipulation and transfer of microparticles across laminar fluid streams. *Small*, 8(17):2757–2764, 2012.

[29] H. Haddadi and J. F. Morris. Microstructure and rheology of finite inertia neutrally buoyant suspensions. *Journal of Fluid Mechanics*, 749:431–459, 2014.

[30] J. Happel and H. Brenner. *Low Reynolds number hydrodynamics: with special applications to particulate media*, volume 1 of *Mechanics of Fluids and Transport Processes*. Springer, 1982.

[31] E. J. Hinch. *Perturbation Methods*, volume 6 of *Cambridge Texts in Applied Mathematics*. Cambridge University Press, 1991.

[32] B. P. Ho and L. G. Leal. Inertial migration of rigid spheres in two-dimensional unidirectional flows. *Journal of Fluid Mechanics*, 65:365–400, 7 1974.

[33] A. J. Hogg. The inertial migration of non-neutrally buoyant spherical particles in two-dimensional shear flows. *Journal of Fluid Mechanics*, 272:285–318, 8 1994.

[34] K. Hood, S. Kahkeshani, D. Di Carlo, and M. Roper. Direct measurement of particle inertial migration in rectangular microchannels. *Lab Chip*, 2016.

[35] K. Hood, S. Kahkeshani, D. Di Carlo, and M. Roper. Direct measurement of particle inertial migration in rectangular microchannels. *Lab on a Chip*, 16:2840–2850, 2016.

[36] K. Hood, S. Lee, and M. Roper. Inertial migration of a rigid sphere in three-dimensional poiseuille flow. *Journal of Fluid Mechanics*, 765:452–479, 2 2015.

[37] K. J. Humphry, P. M. Kulkarni, D. A. Weitz, J. F. Morris, and H. A. Stone. Axial and lateral particle ordering in finite reynolds number channel flows. *Physics of Fluids*, 22:081703, 2010.

[38] S. C. Hur, H. T. K. Tse, and D. Di Carlo. Sheathless inertial cell ordering for extreme throughput flow cytometry. *Lab on a Chip*, 10:274–280, 2010.

[39] R. C. Jeffrey and J. R. A. Pearson. Particle motion in laminar vertical tube flow. *Journal of Fluid Mechanics*, 22:721–735, 8 1965.

[40] S. Kahkeshani, H. Haddadi, and D. Di Carlo. Preferred interparticle spacings in trains of particles in inertial microchannel flows. *Journal of Fluid Mechanics*, 786:R3, 2016.

[41] A. Karnis, H. L. Goldsmith, and S. G. Mason. The flow of suspensions through tubes: V. inertial effects. *The Canadian Journal of Chemical Engineering*, 44(4):181–193, 1966.

[42] J. Katz and J. Sheng. Applications of holography in fluid mechanics and particle dynamics. *Annual Review of Fluid Mechanics*, 42:531–555, 2010.

[43] S. Kim and S. Karrila. *Microhydrodynamics: Principles and Selected Applications*. Butterworth - Heinemann series in chemical engineering. Dover Publications, 2005.

[44] H. Lamb. *Hydrodynamics*. Dover Publications, 1945.

[45] L. G. Leal. Particle motions in a viscous fluid. *Annual Review of Fluid Mechanics*, 12(1):435–476, 1980.

[46] B. LeClair, A. Hamielec, H. Pruppacher, and W. Hall. A theoretical and experimental study of the internal circulation in water drops falling at terminal velocity in air. *Journal of the Atmospheric Sciences*, 29(4):728–740, 1972.

[47] W. Lee, H. Amini, H. A. Stone, and D. Di Carlo. Dynamic self-assembly and control of microfluidic particle crystals. *Proceedings of the National Academy of Sciences*, 107(52):22413–22418, 2010.

[48] D. S. Lemons and P. Langevin. *An introduction to stochastic processes in physics*. JHU Press, 2002.

[49] C. Liu, G. Hu, X. Jiang, and J. Sun. Inertial focusing of spherical particles in rectangular microchannels over a wide range of reynolds numbers. *Lab on a Chip*, 15(4):1168–1177, 2015.

[50] A. J. Mach, J. H. Kim, A. Arshi, S. C. Hur, and D. Di Carlo. Automated cellular sample preparation using a centrifuge-on-a-chip. *Lab on a Chip*, 11:2827–2834, 2011.

[51] J.-P. Matas, V. Glezer, É. Guazzelli, and J. F. Morris. Trains of particles in finite-reynolds-number pipe flow. *Physics of Fluids (1994-present)*, 16(11):4192–4195, 2004.

[52] T. Maxworthy. Accurate measurements of sphere drag at low reynolds numbers. *Journal of Fluid Mechanics*, 23:369–372, 10 1965.

[53] J. B. McLaughlin. Inertial migration of a small sphere in linear shear flows. *Journal of Fluid Mechanics*, 224:261–274, 3 1991.

[54] K. Miura, T. Itano, and M. Sugihara-Seki. Inertial migration of neutrally buoyant spheres in a pressure-driven flow through square channels. *Journal of Fluid Mechanics*, 749:320–330, 6 2014.

[55] T. C. Papanastasiou, G. C. Georgiou, and A. N. Alexandrou. *Viscous Fluid Flow*. CRC Press, 1999.

[56] R. Perry. *Chemical Engineers' Handbook, Third Edition*. McGraw Hill professional. McGraw-Hill Education, 1950.

[57] C. Prohm and H. Stark. Feedback control of inertial microfluidics using axial control forces. *Lab on a Chip*, 14(12):2115–2123, 2014.

[58] I. Proudman and J. R. A. Pearson. Expansions at small reynolds numbers for the flow past a sphere and a circular cylinder. *Journal of Fluid Mechanics*, 2:237–262, 4 1957.

[59] A. E. Reece and J. Oakey. Long-range forces affecting equilibrium inertial focusing behavior in straight high aspect ratio microfluidic channels. *Physics of Fluids (1994-present)*, 28(4):043303, 2016.

[60] M. Roper, A. Simonin, P. C. Hickey, A. Leeder, and N. L. Glass. Nuclear dynamics in a fungal chimera. *Proceedings of the National Academy of Sciences*, 110(32):12875–12880, 2013.

[61] S. I. Rubinow and J. B. Keller. The transverse force on a spinning sphere moving in a viscous fluid. *Journal of Fluid Mechanics*, 11:447–459, 10 1961.

[62] P. G. Saffman. The lift on a small sphere in a slow shear flow. *Journal of Fluid Mechanics*, 22:385–400, 5 1965.

[63] J. A. Schonberg and E. J. Hinch. Inertial migration of a sphere in poiseuille flow. *Journal of Fluid Mechanics*, 203:517–524, 5 1989.

[64] G. Segré and A. Silberberg. Radial particle displacements in poiseuille flow of suspensions. *Nature*, 189(4760):209–210, 1961.

[65] G. Segré and A. Silberberg. Behaviour of macroscopic rigid spheres in poiseuille flow part 1. determination of local concentration by statistical analysis of particle passages through crossed light beams. *Journal of Fluid Mechanics*, 14:115–135, 8 1962.

[66] G. Segré and A. Silberberg. Behaviour of macroscopic rigid spheres in poiseuille flow part 2. experimental results and interpretation. *Journal of Fluid Mechanics*, 14:136–157, 8 1962.

[67] J. Sheng, E. Malkiel, and J. Katz. Using digital holographic microscopy for simultaneous measurements of 3d near wall velocity and wall shear stress in a turbulent boundary layer. *Experiments in fluids*, 45(6):1023–1035, 2008.

[68] M. v. Smoluchowski. Drei vortrage uber diffusion, brownsche bewegung und koagulation von kolloidteilchen. *Zeitschrift fur Physik*, 17:557–585, 1916.

[69] E. Sollier, D. E. Go, J. Che, D. R. Gossett, S. O'Byrne, W. M. Weaver, N. Kummer, M. Rettig, J. Goldman, N. Nickols, S. McCloskey, R. P. Kulkarni, and D. Di Carlo. Size-selective collection of circulating tumor cells using vortex technology. *Lab on a Chip*, 14:63–77, 2014.

[70] E. Sollier, C. Murray, P. Maoddi, and D. Di Carlo. Rapid prototyping polymers for microfluidic devices and high pressure injections. *Lab on a Chip*, 11(22):3752–3765, 2011.

[71] S. E. Spagnolie and E. Lauga. Hydrodynamics of self-propulsion near a boundary: predictions and accuracy of far-field approximations. *Journal of Fluid Mechanics*, 700:105–147, 2012.

[72] J. K. Sveen. An introduction to matpiv v. 1.6. 1. *Mech. Appl. Math.*, (2), 2004.

[73] M. Tachibana. On the behaviour of a sphere in the laminar tube flows. *Rheologica Acta*, 12(1):58–69, 1973.

[74] W. S. Uijttewaal, E.-J. Nijhof, and R. M. Heethaar. Lateral migration of blood cells and microspheres in two-dimensional poiseuille flow: A laser-doppler study. *Journal of Biomechanics*, 27(1):35 – 42, 1994.

[75] P. Vasseur and R. G. Cox. The lateral migration of a spherical particle in two-dimensional shear flows. *Journal of Fluid Mechanics*, 78:385–413, 10 1976.

[76] J. Veysey and N. Goldenfeld. Simple viscous flows: From boundary layers to the renormalization group. *Reviews of Modern Physics*, 79:883–927, Jul 2007.

[77] G. M. Whitesides. The origins and the future of microfluidics. *Nature*, 442(7101):368–373, 2006.

[78] J. Zhou and I. Papautsky. Fundamentals of inertial focusing in microchannels. *Lab on a Chip*, 13:1121–1132, 2013.